Dissertation

submitted to the

Combined Faculties for the Natural Sciences and for Mathematics

of the Ruperto-Carola University of Heidelberg, Germany

for the degree of

Doctor of Natural Sciences

Put forward by

Jennifer Arps, M.Sc.

Born in Remscheid

Oral examination: 26.07.2017

Towards ε-Precision

of U-series Age Determinations of Secondary

Carbonates

Referees:

Prof. Dr. Norbert Frank

Prof. Dr. Rüdiger Klingeler

Auf dem Weg zur ε-Präzision U-Reihen Datierung von sekundären Karbonaten:

In dieser Arbeit wird beschrieben mit welchen Messprotokollen und Datenkorrekturen U-Reihen Alter auf einem MC-ICP Massenspektrometer mit der höchsten derzeit erreichbaren Präzision bestimmt werden können. U- und Th-Isotopenverhältnisse von Probenlösungen mit hohen [U] und [Th] über 6 ppt können mit einer Präzision von 6 ε reproduzierbar vermessen werden ($\varepsilon = 1 \cdot 10^{-4}$). Routinemäßig werden Proben mit moderaten [U] und [Th] mit 8 oder 18 ε-Präzision (U-/Th-Isotopenverhältnisse) bestimmt. Proben, die mit verschiedenen Massenspektrometern vermessen wurden, sind innerhalb ihrer Fehler reproduzierbar und unterstreichen die Glaubwürdigkeit der Messergebnisse.

Mit Hilfe der hochaufgelösten Datierung konnte der Anfang der vorletzten Deglaziation im Vergleich zu schon veröffentlichten Datierungen im Einzugsgebiet der Spannagel Höhle (nördliche Alpen) um 400 a präziser eingeschränkt werden. Die Erwärmung findet nun 2000 a später statt und kann auf den Zeitbereich von 133187 ± 833 a BP bestimmt werden. Dieser Zeitbereich stimmt nun weitgehend mit dem Anstieg der borealen Sommer-Sonneneinstrahlung überein und ist eher vereinnehmbar mit der Milankovic-Hypothese. Außerdem wurden Wachstumsraten mit $\Delta t = 220$ a von zwei Stalagmiten aus benachbarten Höhlen aus den Schweizer Alpen über die letzten 6500 a miteinander verglichen. Die Wachstumsraten korrelieren nicht, erlauben aber in Kombination mit einer Baumgrenzenrekonstruktion Einblicke in die lokale Vegetationsgeschichte.

Towards ε-Precision of U-series Age Determinations of Secondary Carbonates:

In this thesis the measurement protocols and data corrections for U-series dating with the highest achievable precision on a MC-ICP mass spectrometer are described. U and Th isotope ratios of sample solutions with high [U] and [Th] above 6 ppt can be measured reproducibly on a 6 ε-scale ($\varepsilon = 1 \cdot 10^{-4}$). U and Th isotope ratios of sample solutions with moderate [U] and [Th] are routinely determined with 8 to 18 ε-precision. Results from measurements on various mass spectrometers were reproducible within their uncertainties, confirming the credibility of our dating results.

Using high-resolution dating, the beginning of the penultimate deglaciation at the Spannagel Cave (Northern Alps) was dated delayed by 2,000 a at $133,183 \pm 833$ a BP achieving a higher precision of 400 a compared to formerly published results. This age interval is broadly coincident with the rise in boreal summer insolation and seems more concordant to Milankovitch hypothesis. Furthermore, the growth rates of two stalagmites from adjacent caves in the Swiss Alps were compared on a resolution of $\Delta t = 220$ a in the last 6,500 a. Both growth rates show individual growth histories, however when combined with a tree-line record, provide additional insights into the local vegetation history.

Contents

1 Motivation

The decay of U into a series of daughter isotopes provides a key chronometer in paleoclimatology that is objective of studies of climate changes on the time scale of the entire earth's history (U-Pb dating). U-Th dating, or U-series dating, is one of the few methods for dating climate archives over the last 850,000 a and can be applied to a wide variety of natural materials including speleothems (cave deposits), cold water and tropical corals, marine sediments, mollusks, volcanic rocks, fossil bone, and teeth (Ivanovich [1994]).

One important application is the reconstruction of the terrestrial climate by dating climate archives such as speleothems in combination with proxies as δ^{18}O, δ^{13}C, U isotopes, and growth rate (GR) to reconstruct past precipitation, vegetation, and temperature developments (McDermott [2004]; Suksi et al. [2006]; Baker et al. [1998]). Another major application in paleoclimatology is the reconstruction of past ocean dynamics by dating framework-forming corals and pelagic sediments in combination with geochemical proxies like Nd, δ^{18}O, Δ^{14}C, Ba/Cd, δ^{11}B, Li/Mg that provide information about the sources of deep water, water mass circulation, ventilation, alkalinity, pH-value and temperature (Böhm et al. [2015]; Chen et al. [2012]; Lea and Boyle [1990]; Grumet et al. [2002]; Montagna et al. [2014]). It is of great desire to date with high precision as, in particular high-precision speleothem and reef coral dating has been of crucial importance for calibrating the radiocarbon timescale, establishing sea level variability, testing orbital theories of climate change (Milancovic hypothesis), and resolving details of Quaternary climate change over a broad range of timescales (Reimer et al. [2013]; Thompson and Goldstein [2005]). Furthermore, with respect to today's climate change, the knowledge of the last centuries' terrestrial precipitation and vegetation extents or seawater's pH-value, salinity and temperature are tremendously useful and can only be provided with the help of high precise measurements.

U isotopic measurements are exceedingly difficult due to large differences in abundances between ^{238}U, ^{235}U and ^{234}U (e.g., ^{238}U/^{235}U ~ 140 and ^{238}U/^{234}U $\sim 10^4$). Thus, highly precise and accurate measurements challenge the instrument and detector setup and the corresponding measurement protocols. Fortunately, technical advancements in analytical capabilities have lead to continued and significant improvements in dating precision. Recent developments in multi-collector inductively coupled plasma mass spectrometry (MC-ICP-MS) have resulted in dating precisions on a per mil or even ε-unit scale (10^{-4}) leading to a decadal to annual scale of resolution (Cheng et al. [2013]; Fietzke et al. [2005]; Mason and Henderson [2010]; Potter et al. [2005]; Robinson et al. [2002]; Stirling and Andersen [2009]). Thus, the establishment of dating on ε-precision scale is the major focus of this thesis.

The second main focus of this thesis is the examination of the GR of speleothems. Speleothems have proven valuable to paleoclimatology for a number of reasons. These secondary carbonates have the potential to grow continuously for 10^3 to 10^5 a (Fairchild et al. [2012]) and can be dated with high precision and accuracy by U-series disequilibrium methods. Speleothems' most important feature, however, is their capturing of the cave's response to its external environment, as the mean annual atmospheric temperature - apart from a few exceptions - reflects the environment's temperature and the drip water discharge often responds strongly to the degree of infiltration and storage of precipitation. Various models and empirical works show that speleothem growth is dependent on temperature, soil activity, and precipitation (Baker et al. [1993], Baker et al. [1998], Baker et al. [2016]; Dreybrodt and Romanov [2008]; Dreybrodt [1999]; Genty et al. [2001]; Kaufmann and Dreybrodt [2004]; Mühlinghaus et al. [2007]; Romanov et al. [2008]).

Considering the fact that speleothem growth is dependent on climate, one may obtain evidence of the paleoclimate in the catchment of the cave when considering average GR variations or growth phases of either an individual stalagmite or a set of stalagmites (Burns et al. [1998], Burns et al. [2001]; Stoll et al. [2013]; Wong and Breecker [2015]). This would imply that growth records could have regional climate significance. There are merely few high resolution growth records to test whether such influences – either climatic or chaotic – may appear on time scales of centuries. In this thesis, it is explored whether centennial-scale GR patterns could be a robust and reproducible climate proxy.

The thesis begins with a theoretical part (Chap. 2) in which the base for the growth of stalagmites, U-series dating, the instrument, and the detector types are given. In the methods (Chap. 3) the measurement routine and a *MathWorks*® MATLAB program *UThAnalysis* for automated data analysis which was designed as part of this thesis are explained.

The main part of the thesis is divided in two parts. The first part (Chap. 4 and Chap. 5) focuses on high precision U-series dating, its feasibility, and how instrument errors affect accuracy. The reproducibility of ages measured on different instruments, with different detectors and different chemical preparations is determined. In this context, data sets of ages that were already published are repeatedly measured and improved.

The second part (Chap. 6) focuses on an application of U-series dating. A detailed study of the U-series nuclides and GR of two stalagmites from adjacent caves in central Switzerland which span the same growth interval is presented. The study shows that centennial growth patterns are individual and that alpine vegetation, as documented by a tree-line reconstruction, may exert a possible control on the millennial growth trends.

2 Theoretical background

This chapter is meant to provide a theoretical fundament for all three main chapters. Although this thesis is mainly about improving U-series dating techniques, I will start with the introduction of the geochemical background of the growth of speleothems (secondary cave deposits such as stalagmites) which make it easier to understand the following sections, especially Sec. 2.2.

2.1 Growth and growth rate of speleothems

A speleothem is a secondary mineral deposit formed in a cave. The speleothems used for paleoclimatology are almost all calcareous (calcium carbonate $CaCO_3$) and composed of the minerals calcite and/or aragonite which usually form within carbonate rocks, typically limestones ($CaCO_3$) and/or dolomite ($CaMg(CO_3)_2$). The origin of the precipitated mineral lies above the cave within the karst zone or the carbonate bedrock where carbonate is dissolved by the percolating water (Fairchild et al. [2012]).

The geochemistry of cave deposits is schematically illustrated in Fig. 2.1. When a precipitation event occurs in a region where a cave is located the water percolates the soil zone. Due to root respiration and the microbial decomposition of organic matter which is the source of CO_2 within the soil zone, the soil zone's CO_2 concentration is increased up to 100,000 ppm compared to the atmosphere above the surface (400 ppm - 4,000 ppm) (Fairchild et al. [2012]). When the water infiltrates the soil zone it is unsaturated regarding to CO_2, resulting in the dissolution of gaseous CO_2. In the presence of water the dissolved gas is transformed into carbonic acid H_2CO_3 and dissociates into HCO_3^- and CO_3^{2-}.

$$CO_2(g) \rightleftharpoons CO_2(aq) \tag{2.1}$$

$$CO_2(aq) + H_2O \rightleftharpoons H_2CO_3 \tag{2.2}$$

$$H_2CO_3 + H_2O \rightleftharpoons H_3O^+ + HCO_3^- \tag{2.3}$$

$$HCO_3^- + H_2O \rightleftharpoons H_3O^+ + CO_3^{2-} \tag{2.4}$$
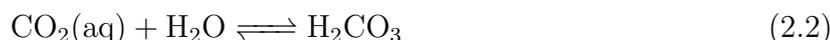
The solution percolates through the soil zone to the karst where it dissolves $CaCO_3$ and where it is fast saturated with respect to Ca^{2+}:

$$CaCO_3(s) + HCO_3^- + H_3O^+ \rightleftharpoons Ca^{2+}(aq) + CO_3^{2-}(aq) + HCO_3^- + H_3O^+ \tag{2.5}$$

$$\rightleftharpoons Ca^{2+}(HCO_3^-)_2 + H_2O. \tag{2.6}$$
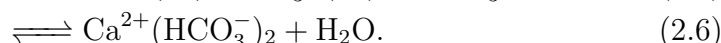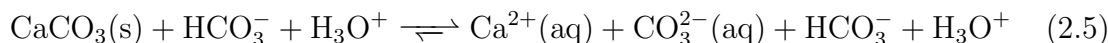
This solution enters the cave by fractures of the karst zone. A sufficiently ventilated cave has a much lower partial pressure P_{CO_2} (usually near atmospheric P_{CO_2}) as the atmospheric $[CO_2]$ of 400 - 4,000 ppm is much lower than the soil zone's concentration (100,000 ppm). Hence, the CO_2 that is dissolved within the solution begins to degas, causing a supersaturation of the solution with respect to Ca^{2+} with a shift of the solution equilibrium towards calcite precipitation ($CaCO_3$). Additionally, the increase of the surface of the droplets caused by the dripping itself also favors precipitation (Bourdon et al. [2003]). This together is described by:

$$Ca^{2+}(HCO_3^-)_2 \rightleftharpoons CaCO_3 + H_2O + CO_2. \tag{2.7}$$
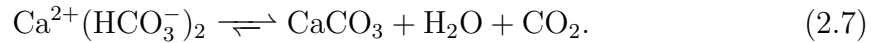
Over the time the accumulation of these precipitates form stalagmites, stalactites, and flowstones, which together compose the three major categories of speleothems.
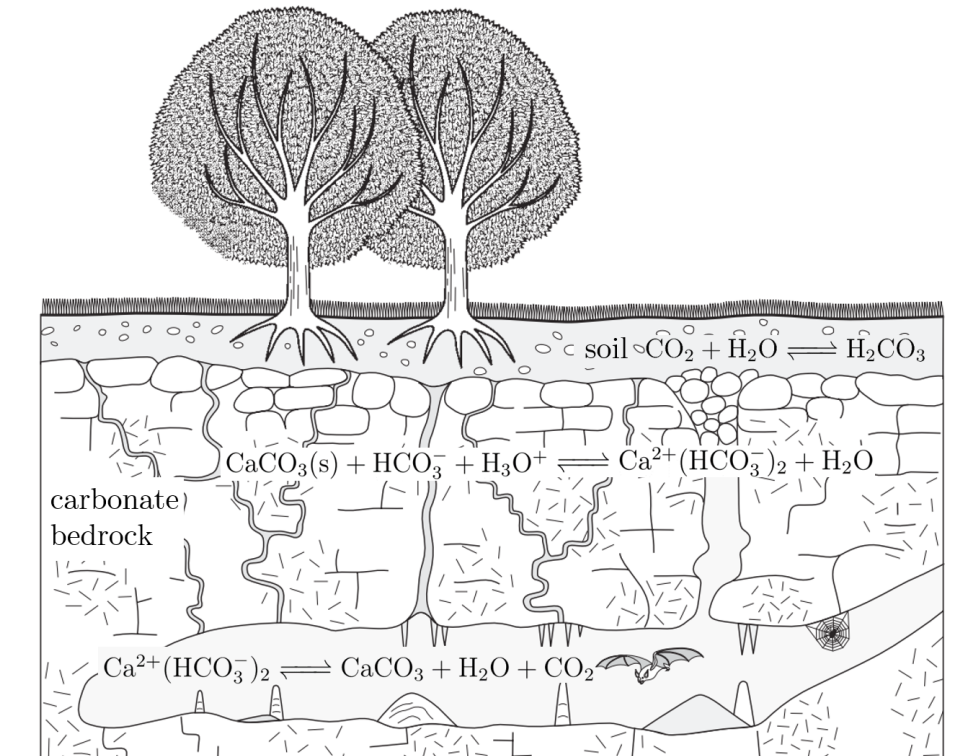
Figure 2.1: Illustration of the processes that form cave deposits (illustration from Fairchild et al. [2012]).

The speleothem's growth rate (GR) is a function of the degree of supersaturation of the drip water with respect to Ca^{2+}. The extent of Ca^{2-} supersaturation of drip water is related to soil CO_2 supply to the soil water, the subsequent host rock dissolution, the gradient between cave air and drip water P_{CO_2}, and cave air temperature. The GR also depends on the drip rate (T is the time between drips) which may be related

to the surface precipitation or soil moisture excess (e.g., Dreybrodt [1999], Dreybrodt and Romanov [2008]; Kaufmann and Dreybrodt [2004]; Baker et al. [1993], Baker et al. [1998], Baker et al. [2016]). These parameters are linked to the outside climate and thus, the precipitation of cave carbonate minerals reflects climate variations.

The precipitation of carbonate from a thin film of water with a surface open to a CO_2-containing atmosphere is complex. The precipitation rates are controlled by several different processes: (1) surface reactions as described by the rate equations of Plummer et al. [1978] from which the surface precipitation rate can be obtained when the concentrations of the reacting species are known, (2) the slow reaction of $H^+ + HCO_3^-$ into $H_2O + CO_2$, the latter being released from the water layer into the atmosphere, and (3) the mass transport of the reacting species towards or away from the carbonate surface. To obtain the precipitation rate under these various processes, transport equations which take into consideration (1) - (3) have to be solved which was done by Baumann et al. [1985]. These studies that are based on the chemical kinetics of the carbonate deposition processes, allowed a theoretical GR to be predicted, which is based on the hydro-geochemical properties of the drip water and the partial pressure P_{CO_2} of the cave air. Baker et al. [1998] used the theoretical model to calculate GR as they occur during the growth of speleothems and linearly approximated the GR to

$$GR = \alpha([\text{Ca}^{2+}] - [\text{Ca}^{2+}]_{\text{eq}})(\text{mmol cm}^{-2}\text{s}^-), \qquad (2.8)$$

where $[\text{Ca}^{2+}]$ is the calcium concentration of the water film, $[\text{Ca}^{2+}]_{eq}$ the equilibrium concentration of calcium in respect to the carbonate, and α the kinetic constant, a function of film thickness δ, cave air P_{CO_2}, temperature and flow regime. Equation 2.8 assumes a continuous water supply, such as that typically found for flowstones. For stalagmites, the time between drips might mean that the rate of supply of saturated water could limit the rate of stalagmite growth. In this case Dreybrodt [1988] demonstrated that the average molecular accumulation rate between two drops at a time interval T is

$$GR = \delta\phi c_0[1 - e^{-T/\tau}]/(T[1 - (1 - \phi)e^{-T/\tau}]). \qquad (2.9)$$

Here τ is a time constant that is defined as δ/α, and represents the relaxation time of excess saturation, where δ is the water film thickness, c_0 is the maximum saturation excess of the water, and ϕ the mixing coefficient between new drip water and the existing water film.

2.2 U-series disequilibrium dating of speleothems

In this section the determination of absolute ages with the help of the ^{238}U decay chain on secondary cave deposits is derived. The determination of absolute ages is

based on the fact that any given radionuclide decays at a known rate and forms a geological "clock". Dating is based on either the decrease of the concentration of a known radionuclide, or contrary by the increase of the stable daughter's product, and by the degree of restoration to a secular radioactive equilibrium caused by a perturbation. U-series measurements follow the latter method and are based on the measurement of the activity of U and its daughter nuclides. ^{238}U sequentially decays via intermediate short-lived isotopes to its daughters ^{234}U and ^{230}Th:

$$^{238}_{92}\text{U} \xrightarrow[4.49\cdot10^9\,\text{a}]{\alpha} {}^{234}_{90}\text{Th} \xrightarrow[24.1\,\text{d}]{\beta^-} {}^{234}_{91}\text{Pa} \xrightarrow[1.18\,\text{min}]{\beta^-} {}^{234}_{92}\text{U} \xrightarrow[2.48\cdot10^5\,\text{a}]{\alpha} {}^{230}_{90}\text{Th} \xrightarrow[7.52\cdot10^4\,\text{a}]{\alpha} {}^{226}_{88}\text{Ra} \ ... \ .$$
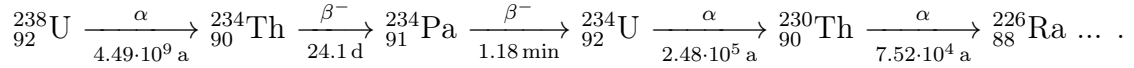
In any naturally occurring material which contain U and which has remained undisturbed on geological time scales, a state of secular equilibrium between the parent and the daughter nuclide in the radioactive series is established. However, when a deposit is formed, various geochemical processes cause isotopic and elemental fractionation which leads to a deficiency of intermediate nuclides due to one or a combination of chemical, physical or nuclear fractionation processes, initiating a state of disequilibrium between parent and daughter nuclides. If no diagenesis or other migratory processes occur after the initial formation of the deposit in this state of disequilibrium, it is possible to determine the absolute date of the deposition event by measuring the extent to which the radionuclide system has returned to the state of secular equilibrium (Ivanovich [1994]).

Two major fractionation mechanisms are utilized by U-series dating: The first is the so called *recoil effect*, i.e. ^{238}U decays to ^{234}U via one α and (two β) decays, in which the nuclide is affected by a backward momentum (recoil). During the decay of ^{238}U the ^{234}Th with an energy in the keV-range is emitted, which is sufficiently energetic to cause recoil displacement of the daughter by more than 20 nm in the lattice of crystalline materials (Kigoshi [1971]). Thus, the daughter ^{234}Th and hence ^{234}U is placed close to the surface of the rock and becomes more fragile to leaching and is preferably dissolved and transported by pore waters compared to ^{238}U. The second fractionation is based on the different chemical solubility of U and Th. U is readily mobilized in the aqueous environment, principally as the highly soluble uranyl ion (UO_2^{2+}) and its complexes. In contrast to U, the long-lived ^{230}Th typically exists in $+4$ oxidation states and is eagerly hydrolyzed and either precipitated or adsorbed on detrital particulates (inorganic and organic) or clay minerals (Bourdon et al. [2003]). Consequently, aqueous solutions such as meteoric waters carry significant amounts of U (typically some ppb), while Th can be considered absent.

2.3 Age determination

The activity A, or decay rate, of a radioactive substance is characterized by the half life $t_{1/2}$, i.e. the time taken for the activity of a given amount N of a radioactive substance to decay to half of its initial amount:

$$A = \frac{dN}{dt} = \frac{ln(2)}{t_{1/2}} = -\lambda N. \tag{2.10}$$

Here, λ is the decay constant. The solution of Eqn. 2.10 can be expressed as

$$N = N_0 e^{-\lambda t} \tag{2.11}$$

N_0 is the initial number of radioactive atoms at time $t = 0$ and N is the remaining number of atoms at time t.

For U-series dating two presumptions must be valid: (1) no gain or loss other than the decay of the parent nuclide or daughter products occur since the time of formation (closed system), and (2) intermediate and daughter decay products are absent at the time of formation, or in case of presence it can be corrected for.

Hence, in adaption from Ivanovich [1994] the $(^{230}\text{Th}/^{234}\text{U})$ activity ratio (activity ratios will be expressed in parentheses in the following) is calculated by:

$$(^{230}\text{Th}/^{234}\text{U}) = \left(\frac{1 - e^{-\lambda_{230}t}}{(^{234}\text{U}/^{238}\text{U})} \right) + \left(1 - \frac{1}{(^{234}\text{U}/^{238}\text{U})} \right) \frac{\lambda_{230}}{\lambda_{230} - \lambda_{234}} \left(1 - e^{-(\lambda_{230} - \lambda_{234})t} \right). \tag{2.12}$$

High signal intensities increase the precision of measurements, hence the more abundant isotope ^{238}U is used for ratio building instead and Eqn. 2.12 is rearranged to:

$$(^{230}\text{Th}/^{238}\text{U}) = \left(1 - e^{-\lambda_{230}t} \right) + \left((^{234}\text{U}/^{238}\text{U}) - 1 \right) \frac{\lambda_{230}}{\lambda_{230} - \lambda_{234}} \left(1 - e^{-(\lambda_{230} - \lambda_{234})t} \right). \tag{2.13}$$

In literature, the $(^{234}\text{U}/^{238}\text{U})$ is often given in so called δ notation, providing the ‰ deviation from radioactive equilibrium:

$$\delta^{234}U = \left(\frac{(^{234}\text{U}/^{238}\text{U})_{\text{meas}} - (^{234}\text{U}/^{238}\text{U})_{\text{eq}}}{(^{234}\text{U}/^{238}\text{U})_{\text{eq}}} \right) \cdot 1000 = ((^{234}\text{U}/^{238}\text{U})_{\text{meas}} - 1) \cdot 1000 \, (‰). \tag{2.14}$$

The activity ratio in secular equilibrium is set to 1, i.e. $(^{234}\text{U}/^{238}\text{U})_{eq} = 1$. Eqn. 2.12 cannot be solved analytically, but is solved graphically or numerically (see Fig. 2.2a). In practice, absolute ages are determined via the $(^{230}\text{Th}/^{238}\text{U})$ and $(^{234}\text{U}/^{238}\text{U})$ activity ratios. The dating range is dependent on U concentration [U] and the dating analytical precision of the isotopic ratios. Presently, a range of up to 650,000 a can be assessed (Cheng et al. [2013]), and in certain cases even up to 850,000 a (Fig. 2.2b; Andersen et al. [2008]).
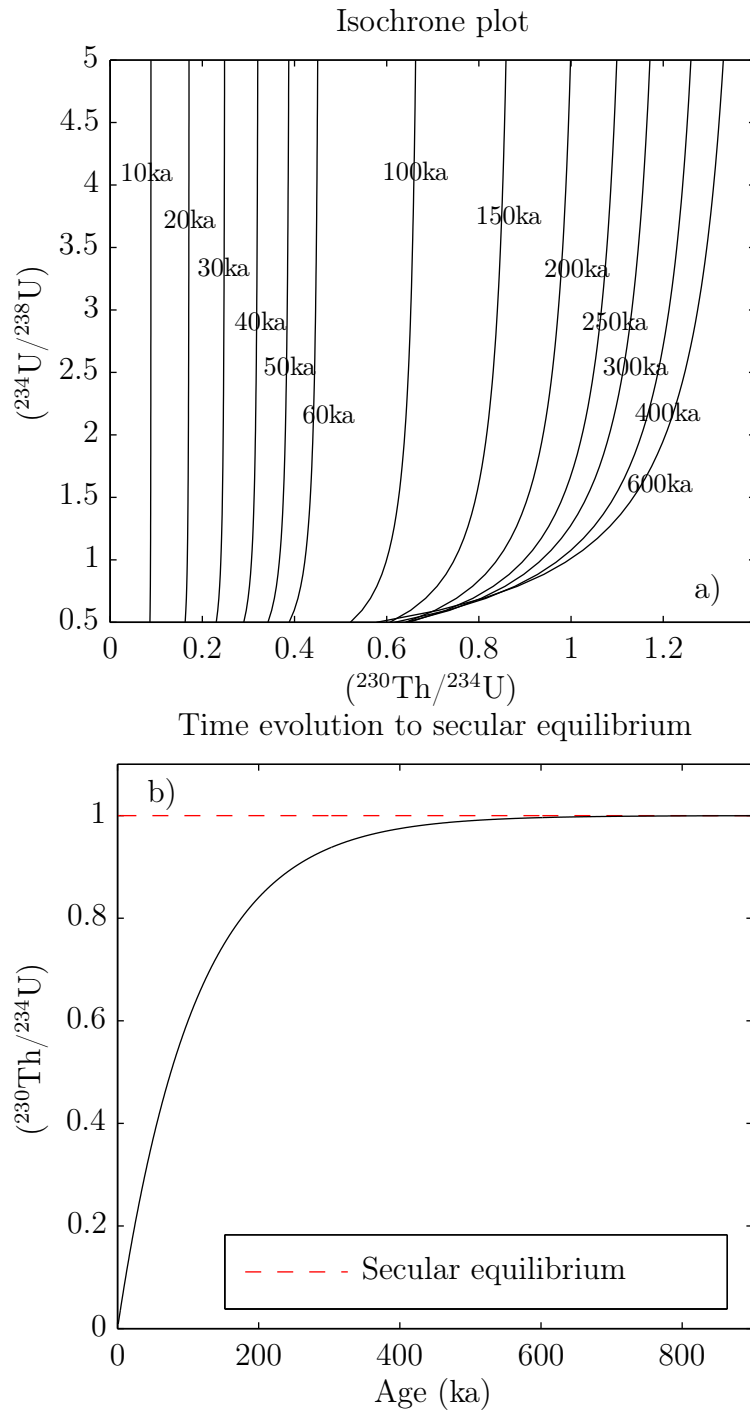
Figure 2.2: a) Graphical solution of Eqn. 2.12 with isochrones. b) $(^{230}\mathrm{Th}/^{234}\mathrm{U})$ versus age. At $\sim 850{,}000\,\mathrm{a}$, i.e. eleven times the half-live of $^{230}\mathrm{Th}$, the limits of today's state of the art U-series dating is reached (Cheng et al. [2013], Andersen et al. [2008]).

In the following, I would like to summarize the above mentioned processes regarding cave deposits; in the limestone above the cave the three isotopes of ^{238}U, ^{234}U, and ^{230}Th are assumed to be in secular equilibrium since the limestone is millions of years old. After the formation of carbonic acid with the infiltrated water and the soil's CO_2, the limestone is partly dissolved, and due to α-recoil a variable abundance of ^{234}U to ^{238}U, if compared to radioactive equilibrium, is generated in the aqueous solution (this is indicated by the variable $(^{234}U/^{238}U)$ ratios in Fig. 2.2 a)). Th does not occur in solution as it is precipitated or adsorbed on detrital particulates or clay minerals. Thus, during calcite precipitation in the cave, ideally only U without Th is incorporated in the calcite crystal lattice, leading to zero initial Th. When measuring a samples' isotopic composition, it is thus presumed that all detected Th atoms result from the decay of ^{238}U and ^{234}U since the time of the deposition of the calcite in the cave. In the end with the help of the activity ratios of ^{238}U and its decay products ^{234}U and ^{230}Th the age and its uncertainty of a sample can be iteratively estimated using numerical methods.

2.4 Mass spectrometric instrument

Here, an introduction to mass spectrometry used to generate U-series data is given. I will present the setup of a newly installed Thermo-Fisher Neptune *Plus* which is a multiple-collector inductively coupled plasma mass spectrometer (MC-ICP-MS). But first of all, I will begin with a brief historical introduction to U-series dating.

U-series dating started with U isotopic measurements conducted by α-counting spectrometry, while consuming large amounts of sample material (e.g. Thurber et al. [1965]). The required analysis times were of up to several weeks to attain analytical precisions at the percent level. Given the order of the half-lives of ^{230}Th and ^{234}U (10^5 a), one out of 10^7 of each of these atoms decays during a 1-week counting time using decay-counting methods.

In the late 1980s the development of direct U isotopic ratio measurement by thermal ionization mass spectrometry (TIMS) had an enormous impact on U-series analysis, which significantly improved precision to the per mil level for the best measurements, mainly caused by an improved signal intensity (e.g Edwards et al. [1987]). An ionization efficiency of 0.1 - 0.5 ‰ integrated over the term of the measurement for Th and U is possible (Edwards et al. [1987]) improving the number of counts for the same sample size by a factor of 10^3. With the help of this technological advance several breakthroughs were gained, e.g. the establishment of the absolute ages of Quaternary climate changes (Stein et al. [1993]; Gallup et al. [1994]; Richards et al. [1994]; Szabo et al. [1994]; Stirling et al. [1995]; Adkins et al. [1998]; Frank et al. [2000]), the calibration of the radiocarbon time scale (Bard et al. [1990a]; Bard et al. [1990b]; Bard et al. [1993]), and the studies in human evolution (Swisher et al. [1996]; Cheng et al. [1998]).

In the beginning of 2000, U-series measurement has further improved with the advent of MC-ICP-MS. Here, two important advantages are inherent of MC-ICP-MS,

which allows to measure on ε-precision scale: (1) U and Th can be ionized relatively easily in a hot plasma source compared to the inefficiency of surface ionization in TIMS. In combination with the Cetac Aridus II desolvating injection system and the Thermo-Fischer Neptune instrument our laboratory achieves up to 2-3 % ionization and transmission efficiency, hence orders of magnitudes higher of U and Th signals. This helps to overcome the limitations of detector noise, counting statistics and background interferences due to higher signals. (2) The use of different detector types (electron multiplier ion counters, Faraday cups (FC) with varying ohmic resistance amplifiers) makes it possible to measure all U isotopes and all Th isotopes simultaneously.

These analytical developments have lead to U-series dating with error precisions on an ε-scale (i.e. $1\,\varepsilon$-unit $= 10^{-4}$; Andersen et al. [2004]; Cheng et al. [2013]).

2.4.1 Setup of the MC-ICP-MS

There are three essential components of the Neptune multi-collector system: (1) the ion source (ICP module), (2) the electrostatic analyzer (ESA module), and (3) the multi-collector module which are illustrated in Fig. 2.3.
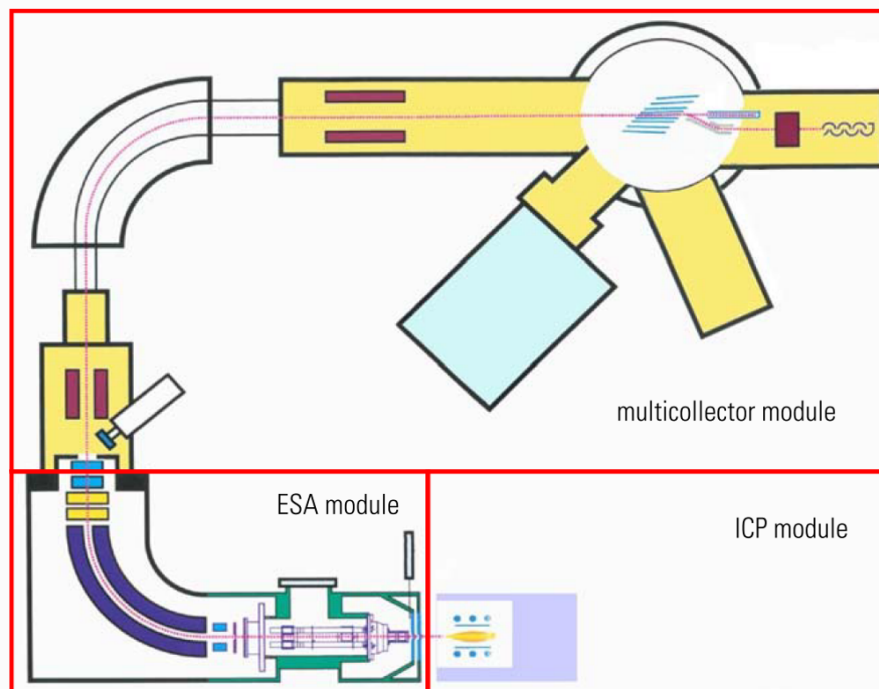

Figure 2.3: Schematic drawing of the three essential components of the Thermo Fisher Neptune *Plus* (image is extracted from ThermoFisher [2009]). In front of the ICP module the Cetac Aridus II is installed which generates an aerosol out of the liquid sample solution that is then injected into the plasma source.

ICP module. The ICP module is responsible for the ion generation using the inductively coupled plasma source. The ICP module consists of the plasma torch and load coil, the mass flow controllers, and the rf generator (ThermoFisher [2009]).

The load coil couples an rf field (27.12 MHz) in an argon gas flow (Fig. 2.4). With an initial spark for seeding electrons an argon plasma is generated and sustained with a temperature > 8,000 K. Since a potential difference is produced by capacitive coupling between the coil and the plasma, a guard electrode has been provided between the coil and the plasma torch to improve performance of the instrument and to avoid secondary discharge. An ideal ion source should produce ion beams of sufficient intensities or background ions; have no cross-contamination; and produce ions with only small mass-dependent isotope discrimination (Thomas [2013]).

The plasma torch consists of two concentric quartz tubes (Fig. 2.4). The gas stream through the outer tube is called cool gas. The cool gas shields the torch body against high temperatures of the plasma and shapes the plasma. The inner tube is used for the plasma gas which maintains the plasma. Its throughput is twenty times lower compared to the cool gas (cool gas: 15 l/min, plasma gas 0.8 l/min).

In the plasma discharge a fine aerosol generated out of the liquid sample solution can be efficiently ionized. The aerosol is generated by a concentric nebulizer and a spray chamber both parts of the Cetac Aridus II system installed in our laboratory. A pump is not required because of the special design of the nebulizer. Via the "venturi effect", i.e. a positive pressure of the nebulizer gas, the sample is sucked through the tubing and at the nozzle of the nebulizer the sample liquid is converted into a fine sample/argon aerosol. With clean sample solutions the concentric nebulizer can give excellent sensitivity and stability, however, the narrow capillary can be blocked, especially if heavier-matrix samples are being aspirated. Because the plasma discharge cannot dissociate large droplets, the aerosol from the nebulizer is refined in the spray chamber, i.e. a condensing of larger droplets at the wall of the spray chamber. The refined aerosol is then directed into the center of the plasma by the injector directly from the spray chamber. The sample introduction area has been called the Achilles' heel of ICP-MS, because only 2-5 % of the sample finds its ways into the plasma, depending on the matrix (Thomas [2013]).

ESA module. The plasma interface is the boundary between the ICP section and the ESA section, it is the interface between plasma in open atmosphere and the interior of the instrument in high vacuum. All kind of particles, such as electrons, ions, photons, neutral gas particles, and the sample ions enter the ESA section through the orifices of the sampler and skimmer cones due to pressure differences. The tongue of the plasma is placed across the tip of the sample cone and the particles enter via the sample cone the first vacuum stage. The skimmer cone is placed downstream of the sample cone and allows access to the next vacuum stage.

The ions that pass the plasma interface are then accelerated by the ion extraction lens into the transfer optics lens stack, which is used to focus the ions onto the entrance slit of the mass analyzer (ThermoFisher [2009]).

The ESA is needed for energy focusing and together with the magnetic sector they
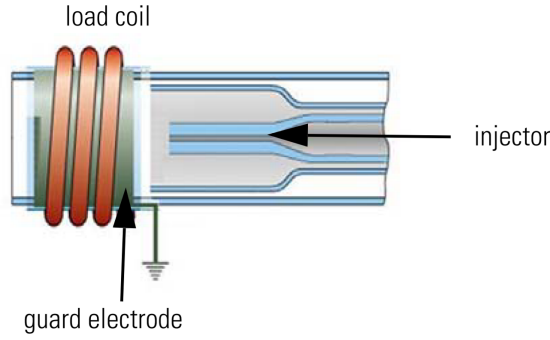
Figure 2.4: Illustration of the glass plasma torch with load coil. The sample is injected as an aerosol in the inner tube of the torch and advances into the center of the plasma that is generated via the load coil and an inital spark (image is extracted from ThermoFisher [2009]).

result in a double focusing ion optical arrangement. The ESA is mainly a spherical deflection unit and consists of two curved plates with applied and reversed DC voltages, providing an electrical field between two deflection plates. The electrical field bends and focuses the ions in respect to their energy. The inner plate with a negative polarity attracts positively charged ions and the outer plate with a positive polarity repels. The ion beam passes between these two plates and is both focused and deflected through an angle of about 90° so that only positively charged ions can pass. After leaving the ESA an acceleration lens at 10 kV accelerates the beam to its final velocity (ThermoFisher [2009]).

MC module. The magnetic sector field separates and focuses the ions according to their mass into different positions along the focal plane of the mass analyzer. Inside the magnetic sector field, ions of different mass travel on different tracks. When an ion of mass m and charge e is accelerated by a potential difference of U volts, it acquires energy, E:

$$E = eU = \frac{1}{2}mv^2 \tag{2.15}$$

where v is the velocity. Rearranging terms in Eqn. 2.15, the velocity of all ions having the same mass-charge ratio is given by:

$$v = \sqrt{\frac{2eU}{m}}. \tag{2.16}$$

For a uniform-field sector magnet mass spectrometer, the ion velocity v, the radius r of the ion path in the field, the magnetic intensity B and the mass-charge ratio m/e are related by the following equation Ivanovich [1994]:

20

$$\frac{m}{e} = \frac{Br}{v}. \tag{2.17}$$

Substituting Eqn. 2.16 and rearranging gives

$$\frac{m}{e} = \frac{B^2 r^2}{2U}. \tag{2.18}$$

The radius of the magnetic sector field is $23\,\mathrm{cm}$ and the deflection angle is $90\,^\circ$ and the magnet can be adjusted to a maximum of $1.2\,\mathrm{T}$.

The zoom optics can be used to change the spacing of the different masses along the focal plane (mass dispersion). Additionally, motors drives can move the detectors along the focal plane of the mass spectrometer to catch the different masses of all isotopes of one element simultaneously. The Neptune *Plus* system has eight movable Faraday cups (FC) and an off-axis fixed center cup. The cups are connected with amplifiers with different degrees of sensitivity (resistors with $10^{13}\,\Omega$, $10^{11}\,\Omega$, and $10^{10}\,\Omega$). The axial beam can be deflected into either the center FC or a secondary electron multiplier (SEM). The SEM is located behind a retarding potential quadrupole (RPQ), which improves abundance sensitivity by an order of magnitude (abundance sensitivities are $5\,\mathrm{ppm}$ at mass 237, in the presence of a strong ^{238}U beam and $0.5\,\mathrm{ppm}$ at mass 237 using the RPQ). The RPQ acts as a high selective filter for ions with disturbed energy or slightly changed flight directions as ions can suffer from a scattering event with residual gas particles or the rim of the apertures. As a consequence, some ions can be scattered wrong masses in the mass spectrum. Typically, this is indicated by an extended peak tail or a spread background, or both, in the mass spectrum (ThermoFisher [2009]; Thomas [2013]).

2.5 Detector types

In U-series dating the detector system is challenged when measuring isotopes with abundances ranging five orders of magnitude. Hence, in U-series dating two types of detectors are commonly used; that are (1) ion counters of the type secondary electron multipliers (SEM) and (2) Faraday cups (FC). FC can be equipped with different ohmic resistors used in the amplifiers feedback loop, that influences the sensitivity. The dynamical ranges of the used detectors for MC-ICP-MS were determined by Dornick [2016]. In Tab. 2.1 the dynamical ranges, i.e. the linear range of each detector and amplifier are shown.

However, since different detectors and amplifiers are used, any discrepancies, such as collection efficiency, dead time, and linearity among collectors may affect the precision of the results.

Table 2.1: Dynamical range of the SEM and the FC (data by Dornick [2016]).

	min intensity	max intensity
SEM	10,000 cps	300,000 cps
$10^{13}\,\Omega$	0.8 mV*	0.5 V*
$10^{12}\,\Omega$	1.6 mV*	5 V*
$10^{11}\,\Omega$	15.0 mV*	50 V*
$10^{10}\,\Omega$	50.0 mV*	500 V*

*Intensities are referred to the standard $10^{11}\,\Omega$ amplifier, whereas 62,500 cps $\approx$ 1 mV.

2.5.1 Secondary electron multiplier

For small signal ranges (see Tab. 2.1; i.e. < 0.8 mV $\approx$ 50,000 cps), a SEM can provide a higher accuracy and precision than FC (Dornick [2016]). The detector is operated in the pulse-counting mode, in which the ions are detected individually.

An image of the SEM with installed RPQ is shown in Fig. 2.5. The SEM has 19 dynodes arranged in a cascade, the impact of an ion on the first dynode generates secondary electrons, which are attracted to the next dynode by an applied potential difference. This is repeated at each dynode. The gain of an SEM has to be cross-calibrated against a FC when isotope ratios are measured using both, FC and SEM simultaneously. Hence, it is desirable to measure all isotopes on the same detector types.

To date detection of small ion beams the SEM is preferred over the use of FC. That is due to the FC's limitation by the electrical noise on the resistor used in the amplifiers feedback loop. Measurements using SEM in ion counting mode, however, suffer, from variability in the detection efficiency, both as a function of time and beam size. The dependence of the efficiency as a function of beam size, i.e. non-linearity, needs to be characterized in detail so that corrections can be applied. Furthermore, the rate is limited by the dead time which is usually 20 ns. This means a signal at 300,000 cps (~ 4.8 mV compared to a standard $10^{11}\,\Omega$) the signal's correction is already 6 ‰ of the real signal. Hence, more stable Faraday detection systems, amplifiers equipped with high $10^{12}\,\Omega$ and $10^{13}\,\Omega$ resistors in the feedback loop have been developed. Compared to the default $10^{11}\,\Omega$, $10^{12}\,\Omega$ and $10^{13}\,\Omega$ have a better signal-to-noise-ratio which is further discussed in Sec. 4.1.1.

2.5.2 Faraday cups

The FC are made from solid carbon. The cup is an element in a circuit; the current flow through the circuit can be very accurately measured and is directly proportional to the number of ions hitting the surface of the FC. The resulting potential difference across the FC's resistors is proportional to the intensity of the incident beam; the ion current is given by $I = ne$, where n is the number of ions per second. The voltage
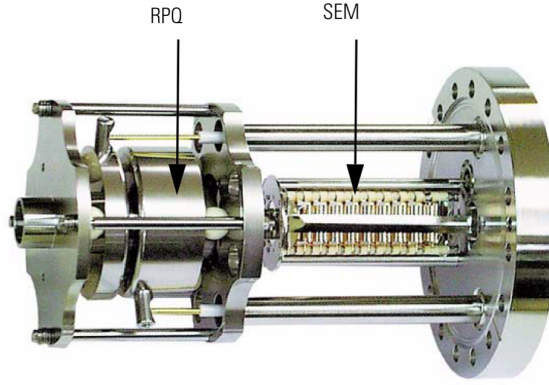
Figure 2.5: Illustration of an SEM with RPQ (image is extracted from ThermoFisher [2009]).

across the resistor is $U = IR = neR$, i.e. $n \approx 62{,}500\,\mathrm{cps}$ for generating $1\,\mathrm{mV}$ on a standard $10^{11}\,\Omega$ detector.

Each FC is connected to a current amplifier with different ohmic resistors ranging from 10^{10} to $10^{13}\,\Omega$ influencing the amplification level. To avoid any temperature effects on the stability of the current amplifier, the amplifier housing is thermo-stated with an accuracy of $0.01\,^\circ$ and evacuated to improve the noise level of the baselines.

Because the detection is based solely on the charge, no mass discrimination is exhibited, and ions of higher charge states produce a correspondingly larger signal which is an advantage in high precision measurements. Commercial FC detectors may have a weak magnetic field to prevent secondary electrons from leaving the FC and they may operate with a slight positive bias on the impacted surface to reduce secondary electron emission.

Due to the high ohmic resistances of the amplifiers, the signal needs time to establish and decay. Hence, a decay time between measurements of different isotopes, i.e. different signal intensities is needed. Dornick [2016] measured the decay times of our amplifiers (see Tab. 2.2).

Table 2.2: Decay time of the FC (data by Dornick [2016]).

	Decay time ($<1\,\%$)	Decay time ($<0.1\,\%$)
$10^{10}\,\Omega$	$0.79\,\mathrm{s}$	$0.97\,\mathrm{s}$
$10^{11}\,\Omega$	$0.78\,\mathrm{s}$	$1.04\,\mathrm{s}$
$10^{12}\,\Omega$	$1.71\,\mathrm{s}$	$3.87\,\mathrm{s}$
$10^{13}\,\Omega$	$4.12\,\mathrm{s}$	$5.54\,\mathrm{s}$

The robustness of an FC detector system is a consequence of its inherent simplicity. Hence, the gain is relatively stable and the standard $10^{11}\,\Omega$ changes only by up to

0.24 ppm/a (Dornick [2016]). The gain is determined via the instruments software by applying a known voltage of 3.33333 V to the electronics of the FC's amplifiers. It is a disadvantage that it is not possible to determine the gain of the $10^{13}\,\Omega$ resistor electronically. We hope, that this issue might be solved by Thermo Fisher soon.

The $10^{13}\,\Omega$ resistor provides better precision obtained in the intensity range usually covered by ion counting and the $10^{11}\,\Omega$ resistor (0.8 - 15 mV Dornick [2016]) which suggests that the newly developed high gain resistor can potentially substitute the SEM. In addition, the use of FC equipped with high gain resistors will be less time consuming and more practical in terms of flexibility in the collector setup.

3 Methods

3.1 Dating routine

In this chapter the measurement protocols, data treatment and data corrections are described in detail.

3.1.1 Measurement protocols

The isotopic measurements of ^{229}Th, ^{230}Th, ^{232}Th, ^{233}U, ^{234}U, ^{235}U, ^{236}U, and ^{238}U are carried out on a Thermo-Fisher Neptune *Plus* MC-ICP-MS. Depending on the concentration of ^{234}U and ^{230}Th, the measurement protocol is either to measure ^{234}U and ^{230}Th in semi-static mode on the FC (for signals above $2\,\text{mV}$, $10^{13}\,\Omega$ resistor) or on the SEM (when diluted to less than $125{,}000\,\text{cps}$). With a transition efficiency of 1-3 %, a minimum $1.5\,\text{ppt}$ concentration of the isotopes is required to measure on $10^{13}\,\Omega$ resistors. Isotope ^{238}U is typically measured on a $10^{10}\,\Omega$ resistor, while the other isotopes are measured on $10^{11}\,\Omega$ resistors. The detector arrangement and measurement protocol for simultaneous U and Th isotope measurements is illustrated in Tab. 3.1.

Final solutions are diluted such, that the isotope with the highest abundance, i.e. ^{238}U, has an intensity at $\sim 30\,\text{V}$ (equivalent to a $10^{11}\,\Omega$ resistor). The Th and U fractions are mixed to minimize the influence of abundance sensitivity, and to measure the analyzed isotopes simultaneously. Generally, the entire Th fraction is used and admixed to U in the order of 5-10 % of the solution (depending on [U]).

A standard sample bracketing technique (i.e. standard-sample-standard measurements in Tab. 3.1) is used for each sample measurement. The instrument baseline is assessed as a noise reference for the signals of each isotope. Measurement sequences start with the corrections for Hydride ions (H$^+$) and tailing/abundance sensitivity (h-as in Tab. 3.1) and chemical blank which are monitored over the course of the day. Measurements of each sample last about $20\,\text{min}$ and the samples are measured with integration times of $1.049\,\text{s}$ to $2.097\,\text{s}$, and approximately 100 or 80 scans, with three seconds idle/decay time between the magnetic field jumps. With this configuration average precisions of $1.8\,\text{\textperthousand}$ (see Sec. 4.2) for Th ratios and of $0.8\,\text{\textperthousand}$ for U ratios are achieved (two years time span). The idle or decay time is sufficient to drop the initial signal of the amplifier to $\leq 100\,\text{ppm}$, which is below our measurement precision of per mil to ε-scale. To maximize signal-to-noise ratios, the minimum beam intensities are increased if possible. Generally, it is desirable that each isotopes' drift is less than 3 % in standard deviation in $20\,\text{min}$ measurement time. Johnson Nyquist noise, instrument blank, and the most dominating counting statistics limit

the signal-to-noise ratio of the amplifiers. For a signal-to-noise ratio of $\leq 2\,‰$ for each isotope, intensities need to be above $8\,\mathrm{mV}$, $24\,\mathrm{mV}$, and $48\,\mathrm{mV}$ ($10^{13}\,\Omega$, $10^{11}\,\Omega$, $10^{10}\,\Omega$).

3.1.2 Data treatment and corrections

The first correction applied to the data results from the finite abundance sensitivity of the instrument which generates a scattering tail of the ^{238}U- and the ^{232}Th beam at lower masses. This is measured on the central SEM including an RPQ at half mass to correct for the isotopes that are measured on the SEM. For the isotopes that are measured on cups that lack an RPQ, the scattering tail is measured on the IC2, which is an additional SEM (without RPQ) positioned at the deflection unit L5. The 237/238 isotopic ratio is typically in the range of $0.3 - 0.7\,\mathrm{ppm}$ (with RPQ).

A second correction applied to the data results from hydrated ions. For correction of U Hydride (U-H$^+$), the isotope on 239 amu is monitored over the course of the day. For correction of Th Hydride (Th-H$^+$) the isotope on 233 amu is measured with an in-house ^{232}Th solution (^{230}Th$/^{232}$Th $= 1.04{\cdot}10^{-6}$). Usually, both values are in the range $10 \pm 9\,\mathrm{ppm}$ (see Sec. 4.1.3).

After correcting tailing and Hydrides the mass bias is determined, for which the natural ratio of ^{235}U$/^{238}$U isotopes is used due to the lack of natural Th-isotopes. The residual differences of U isotopes in standards demonstrate the necessity to normalize using a bracketing method.

Each sample measurement is bracketed by two measurements of the standard Harwell Uraninite (HU-1), which are typically diluted to the same signal intensities as the one of the sample. The HU-1 standard is in secular equilibrium and the activity ratios of (^{234}U$/^{238}$U) and (^{230}Th$/^{238}$U) are supposed to be one. The reproducibility of the HU-1 standard is (^{234}U$/^{238}$U) $= 1.00002 \pm 0.00082$; (^{230}Th$/^{238}$U) $= 1.0004 \pm 0.00180$ ($1\,\sigma$ standard deviation spanning two years). Hence, any offset of the activity ratios due to machine errors is detected in the standard measurements and used for the correction of the activity ratios of the samples that are needed to calculate a U-series age.

Isotope ratios were used to calculate U-series ages according to the decay equations of Ludwig and Titterington [1994] and the error propagation accounts for the statistical uncertainties, but also for detrital ^{232}Th-correction if significant (for details see Neff [2001]).

3.1.3 Chemical preparation

Chemical preparation followed sample dissolution, spiking with ^{229}Th, ^{233}U, and ^{236}U and subsequent purification of U and Th using wet-column extraction chromatography with Eichrom UTEVA. The purification of U and Th is mainly due to the necessity for removal of unwanted interferences in the mass spectrum and to provide optimal ionization efficiency (see Sec. 4.2.1). The chemical separation protocol followed the

procedure of Wefing [2016], Matos et al. [2015], Fontugne et al. [2013], and Douville et al. [2010].

3.2 Automated data analysis protocol

In order to generate U-series ages the following corrected isotopic ratios are needed:

- $^{235}U/^{238}U$ for mass bias correction

- $^{234}U/^{238}U$ for the calculation of $(^{234}U/^{238}U)$

- $^{235}U/^{236}U$ for the calculation of $[^{238}U]$

- $^{234}U/^{233}U$ for the calculation of $[^{234}U]$

- $^{233}U/^{236}U$ (artificial known isotopic ratio of the spike) for double-checking the mass bias correction

- $^{230}Th/^{229}Th$ for the calculation of $[^{230}Th]$

- $^{229}Th/^{232}Th$ and $^{230}Th/^{232}Th$ for the correction for possible initial Th impurities in the samples which is called detrital ^{232}Th-correction (see Bourdon et al. [2003] and Neff [2001]).

The raw data as it is provided by the Thermo Fisher Neptune *Plus* software is corrected for the process blank, mass bias, tailing, Hydride formation ($-H^+$) and spike impurities (see Sec. 3.1.2). In the framework of this thesis a data analysis *MathWorks*® MATLAB program *UThAnalysis* was designed to automatically correct the isotopic ratios. The program further provides an overview on the used correction factors and the process blank. The graphical user interface is illustrated in Fig. 3.1 and the corresponding source code is implemented in the Appendix C.

Table 3.1: Dating routine and collector configuration for U-series measurements.

Faraday cups amplifier	L1 $10^{11}\,\Omega$	Center $10^{13}\,\Omega/(\text{SEM})$	H1 $10^{11}\,\Omega$	H2 $10^{11}\,\Omega$	H3 $10^{10}\,\Omega$
h-as U SEM		(228.50)			
		(230.50)			
		(231.50)			
		(233.50)			
		(236.50)			
		(236.70)			
		(237.05)			
		(237.50)			
		(239.00)			
		-			^{238}U
h-as U IC2	...	...	...	...	...
h-as Th SEM		(227.50)			
		(228.50)			
		(229.50)			
		(230.50)			
		(231.50)			
	^{232}Th	(^{233}U)			
h-as Th IC2	...	...	...	...	...
Chemistry blank	^{233}U	(^{234}U)	^{235}U	^{236}U	^{238}U
	^{229}Th	(^{230}Th)		^{232}Th	
		(^{229}Th)	^{230}Th		
Standard	^{233}U	^{234}U	^{235}U	^{236}U	^{238}U
	^{229}Th	(^{230}Th)		^{232}Th	
		(^{229}Th)	^{230}Th		
Sample	^{233}U	^{234}U	^{235}U	^{236}U	^{238}U
	...	...	...	...	...
	...	...	...	...	...
Standard	...	...	...	...	...

h-as refers to measuremens to correct for Hydride and abundance sensitivity (tailing). This is done for the two tails of ^{238}U and ^{232}Th to correct on SEM with RPQ and the other to correct for cup measurements (IC2 without RPQ). 239 amu and ^{233}U are measured for Hydride corrections. Isotopes and other amu in () are measured on SEM.
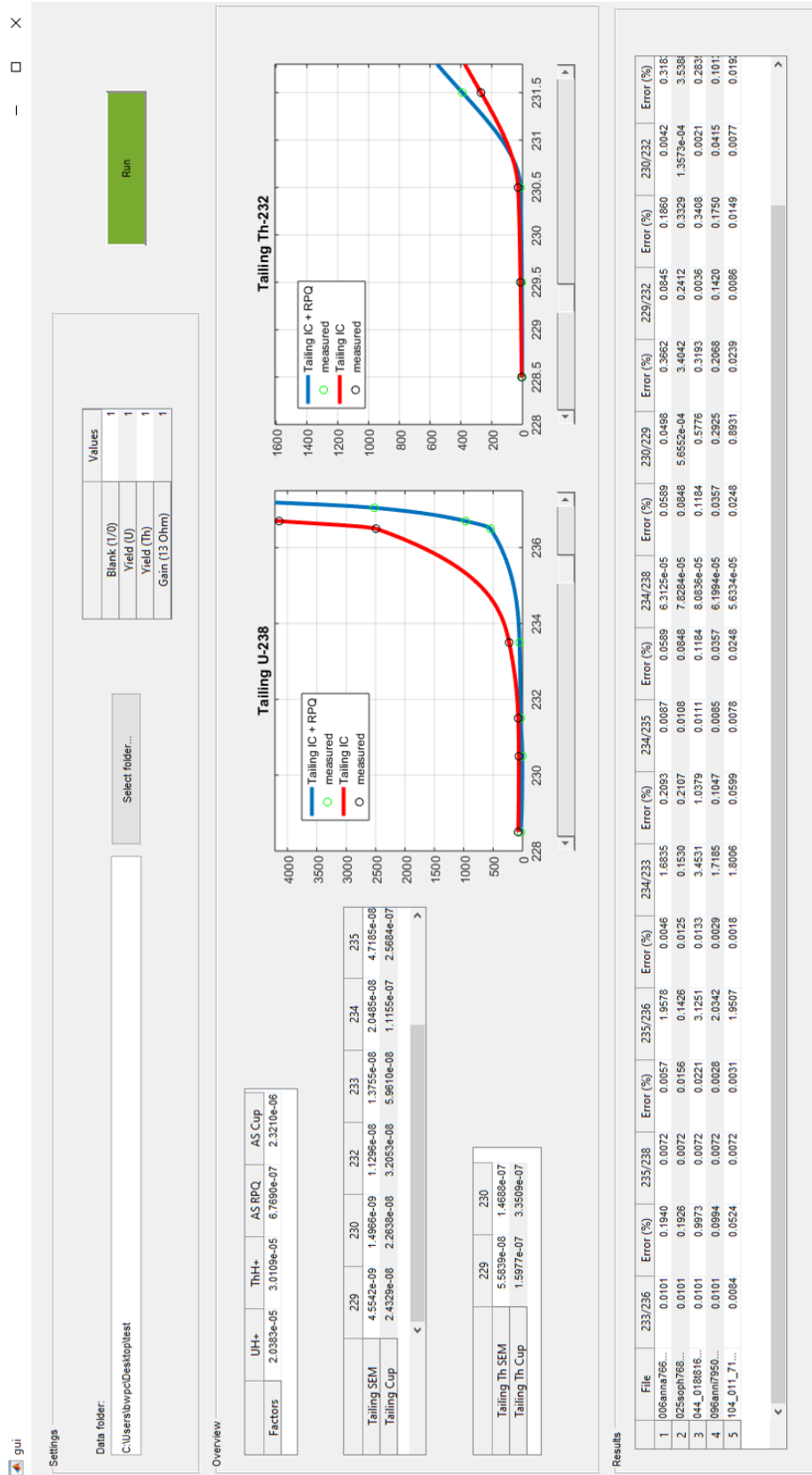
Figure 3.1: Illustration of the graphical user interface of the automated data analysis program *UThAnalysis* for determining corrected isotopic ratios. Settings panel: selection of the folder containing the data, the h-as U and the h-as Th files, and the process blank files. Blank = 1: process blank is subtracted within *UThAnalysis*, Blank = 0: process blank was already subtracted by the Thermo Fisher Neptune *Plus* software. Varying the factors in Yield (U), Yield (Th), and Gain (13 Ohm) cancels/tunes for yield and gain drift for the isotopes ^{234}U, ^{230}Th, ^{229}Th. Overview panel: Hydride formation U-H$^+$ and Th-H$^+$, and the abundance sensitivity (AS) of the SEM/RPQ and cups are shown. The tailing measurements and their interpolation to full masses are plotted and the corresponding correction factors are shown in the two tables. Results panel: corrected ratios with 2 σ errors in %.

4 Towards ε-precision

U isotopic measurement is exceedingly difficult due to large differences in abundance between ^{238}U, ^{235}U and ^{234}U (e.g., ^{238}U/^{235}U ~ 140 and ^{238}U/^{234}U $\sim 10^4$). Thus, highly precise and accurate measurements challenge the instrument and detector setup and the corresponding measurement protocols. But recent studies showed that U-series dating with error precisions on an ε-scale is feasible using the newest MC-ICP mass spectrometry technology (i.e. $1\,\varepsilon$-unit $= 10^{-4}$) (Andersen et al. [2004], Cheng et al. [2013]). In this chapter it is discussed how ε-precision dating can be achieved, what kind of appropriate corrections need to be applied, and how critical the correction's impact is on accuracy.

In Sec. 2.4 two inherent advantages of MC-ICP-MS were introduced which allow for measurement at ε-precision scale and are repeated at this point: (1) U and Th can be ionized relatively easily in a hot plasma source compared to the inefficiency of surface ionization in TIMS (in combination with the Cetac Aridus II and the Thermo Fisher Neptune Instrument our laboratory achieves a 2-3 % ionization and transmission efficiency). (2) The use of different detector types (SEM ion counters, FC with varying ohmic resistance amplifiers) makes it possible to measure all U isotopes and all Th isotopes simultaneously.

Analytical developments in U-series dating by MC mass spectrometry (both TIMS and MC-ICP-MS) have emphasized high precision measurements using small sample sizes. It is now possible to routinely measure both ^{234}U/^{238}U and ^{230}Th/^{238}U with 1–2 ‰ uncertainties ($2\,\sigma$) using only a few tens of ng of U (Robinson et al. [2002], Goldstein [2003], Andersen et al. [2004], Fietzke et al. [2005], Mason and Henderson [2010], Cheng et al. [2013]). Because U sample size is no longer a limiting factor for many U-series studies, recent studies focused on significantly improving dating precision by increasing sample size while maintaining a manageable measurement protocol.

"High precision" dating refers to determining the activity ratios $(^{234}$U/^{238}U$)$ and $(^{230}$Th/^{238}U$)$ at ε-precision. This does not necessarily lead to age precision on ε-scale as Eqn. 2.12 and Fig. 2.2a show that a shift in the activity ratios has more impact on older ages located at the steep slopes of Fig. 2.2a. Under ideal circumstances the state of the art is a modeled analytical age precision of $1{,}000 \pm 2$, $10{,}000 \pm 5$, $30{,}000 \pm 20$, and $300{,}000 \pm 1{,}000$ a that was thus far only proven experimentally for very old ages (and hence for samples high in [Th]) in Cheng et al. [2013].

The improvement in the gained intensities during measurements leads to high precise isotopic ratio measurements which does not necessarily imply accuracy with regards to natural activity ratios. Hence, in this thesis, the term of accuracy is

included when considering high precision measurements. The accuracy of an age is limited by possible fractionation processes of isotopes of U and isotopes of Th that happened during the chemical preparation of the samples, and by isotopic fractionation induced by the instrument itself. But since Cheng et al. [2013] and Wefing [2016] see no evidence for differential isotopic fractionation during chemical preparation, here, the focus is on the applied instrumental corrections, and on the quality of the corrections for ages with ε-precision errors.

In the following sections, sources of errors that affect accuracy will be introduced. These error parameters were measured and their extent of fluctuation that occur during day-to-day routine instrument use were quantified. To examine the errors fluctuation's impact on accuracy, these error fluctuations will be applied to the activity and age analysis of samples that were measured in our laboratory. Consequently, four different kinds of samples were selected that reflect, in their [U] and [Th], their measured intensities, and whose age range is typical of secondary carbonates used for U-series dating. The four samples' intensities and ages span from very low signals and ages close by the detection limit (fg/ml solution) up to old samples which are heavy in concentration to demonstrate the average but also the maximum extent of instrumental fractionation correction on accuracy.

The first sample (C09-2) originates from a stalagmite from the Cloşani Cave located in south-western Romania, which is only 390 ± 25 a old and provides very low concentration of $[^{238}U] \sim 45$ ppb and $[^{230}Th] \sim 0.004$ ppt. Due to low concentrations this sample was not selected to prove high-precision measurements but rather for examining the detection limits. The second sample, Emmertal3, is a cryogenic cave calcite from southern Frankenalb, Germany, that has an age of $32,700 \pm 120$ a and a concentration of $[^{238}U] \sim 1.4$ ppm and $[^{230}Th] \sim 9$ ppt. The third sample (GeoB) is from a coral from the Angolan Margin from core GeoB20933-1 of cruise M122 with an age similar to Emmertal3, i.e. $33,600 \pm 80$ a, and with a typical coral concentration of $[^{238}U] \sim 4$ ppm and $[^{230}Th] \sim 21$ ppt. Emmertal3 and GeoB are, despite of their similar age, different in [U] and [Th]. Their accuracy analysis will give insight about the impact of instrumental errors as a function of intensity and detector types as isotope ^{234}U was measured either on SEM (Emmertal3) or on a $10^{13}\Omega$ FC (GeoB). The last sample (SPA-52) is from a flowstone from the Spannagel Cave in Austria which is $132,580 \pm 120$ a in age. The latter is noteworthy for its very high concentration of $[^{238}U] \sim 85$ ppm and $[^{230}Th] \sim 940$ ppt, so that all isotopes were able to be measured on Faraday cups and even exceeded the formerly mentioned ideal precision.

As previously stated, high signal intensities are fundamental for ε-precision, as the relative impact of the errors of counting statistics and the constant offset of the baseline decreases with signal intensity. Hence, I will start with a discussion about the signals needed to achieve ε-precision to overcome counting statistics limitations and baseline noise of Faraday cups (measured by Dornick [2016]).

4.1 Influences of machine parameters on precision

4.1.1 Precision limit: counting statistics and baseline

Counting statistics together with baseline noise mainly induced by thermal noise determine the base limit of noise in ICP-MS. The counting statistics in ICP-MS is mainly based on the variance of the number of atoms during the sample injection via a nebulizer system (Aridus), ionization fluctuation in the plasma itself, variance during differential pumping between plasma, sample and skimmer cone, incomplete transmission inside the ion channel and uncertainties in the detector itself, all following a Poisson distribution. A detailed study of Ulianov et al. [2014] showed however, that the distribution of count numbers in ICP-MS is a doubly stochastic Poisson process having an additional, "excess" variance in the uncertainty of ICP-MS signals (also known as flicker noise), caused by changes in transmission probabilities and changes in the amount of ions generated and being transmitted. In this section, for reason of simplicity any excess variance is neglected and the only focus is placed on the regular Poisson distribution assuming that counting statistics are directly proportional to the square root of the signal I.

The thermal noise problem is resolved by ion counting on SEM. However, the use of this technique is limited by other restrictions which were discussed in Sec. 2.5: uncertainties in channel cross calibration, possible non-linearity, instability, and the limited dynamic range of the ion counters. In contrast to SEM, Faraday cups have a higher baseline induced by thermal noise. The degree of noise is a function of the chosen ohmic amplifier, as low resistors usually have a higher signal-to-noise ratio (see 2.5 and Tab. 4.1). There remains a gap in the dynamic intensity range, where ion counters are not good enough anymore because of their specific limitations, and Faraday cup detector (default standard $10^{11}\,\Omega$) are limited due to noise. Hence, Thermo Fisher Scientific generated those new set of amplifiers with Tera-Ohm feedback resistors that are $10^{12}\,\Omega$, $10^{13}\,\Omega$ and for high signals $10^{10}\,\Omega$. Dornick [2016] measured the signal-to-noise ratio U_R of the detectors in his bachelor thesis shown in Tab. 4.1.

As counting statistics' error is $\sqrt{I}$ (shot noise) and the baseline is roughly a constant offset, it follows that as the signal intensity gets larger, the noise has less of an impact on the precision of the signal. This means that at high ion counts, the most dominant source of imprecision in ICP-MS is derived from instrumental drift and the shot (and flicker) noise generated in the sample introduction area. The $\%\,\mathrm{RSD}$ (ratio standard deviation) is ultimately limited by counting statistics and the signal-to-noise ratio of the detectors and is calculated with the following equation:

$$\%\,\mathrm{RSD} = \frac{\sqrt{\sqrt{I}^2 + U_R^2}}{I} \cdot 100. \tag{4.1}$$

Figure 4.1 shows that with increasing ohmic resistors the less intensity is needed to reach a higher precision. E.g., measurements with 1 s integration times performed with the $10^{13}\,\Omega$ amplifier do need an intensity of $1.3\cdot10^6$ cps (i.e. 21 mV on a standard $10^{11}\,\Omega$ amplifier) to gain ε-precision. In contrast, the standard $10^{11}\,\Omega$ amplifier needs a signal of $3.0\cdot10^6$ cps (i.e. 48 mV) generating the same precision. As the baseline noise of the ohmic amplifiers is statistical (Dornick [2016]) precision is improved by increased integration times t ($\sim \mathrm{SD}/\sqrt{t}$) or by repeated measurements n ($\sim \mathrm{SD}/\sqrt{n}$), respectively. If a stable signal can be maintained long enough and prolonged and repeated measurements are possible, ε-precision is achieved with less intensity, making the use of the $10^{13}\,\Omega$ amplifier an attractive detector for low mV signals.

Table 4.1: Signal-to-noise ratio of ohmic amplifiers of the Faraday cups with 1 s integration time (data by Dornick [2016]).

Ohmic resistors (Ω)	10^{10}	10^{11}	10^{12}	10^{13}
Signal-to-noise ratio (μV)	101	40	22	11

4.1.2 Tailing correction

After introducing the base limit of U-series dating a discussion about data corrections follows. In this section the extent of the tailing correction on precision is examined. Two significant tails from ^{238}U (and ^{235}U) and ^{232}Th exist below the ^{234}U and ^{230}Th ion beam that arises from the scattering of low energy ^{238}U and ^{232}Th ions caused by particle collisions in the mass spectrometer analyzer (Fig. 4.2). The magnitude of the tail is thus strictly related to the mass spectrometer and expressed as an abundance sensitivity (defined by convention as the contribution from ^{238}U at mass 237)

The tailing problem is largely eliminated by monitoring background zeros at half-masses and applying a tailing correction to all isotopes that are affected by the tail. For the ^{238}U tail we correct for ^{234}U, ^{233}U, ^{232}Th, ^{230}Th, and ^{229}Th, and for the ^{232}Th tail we correct for ^{230}Th, and ^{229}Th. The magnitude of the ^{238}U and ^{232}Th tail can be further minimized in a mass spectrometer equipped with an RPQ to reject the majority of scattered ions. This typically improves abundance sensitivity by an order of magnitude (Thermo Fisher claims for the Neptune instrument a $237/238 \leq 0.5$ ppm (with RPQ)).

The low abundance isotopes ^{234}U, ^{230}Th, and ^{229}Th are usually measured on the center SEM equipped with an RPQ. The other isotopes are measured on Faraday cups that generally lack an RPQ. Thus, the two tails are measured twice; first, the tail on half-masses is measured on the center SEM and second, the tail is measured on an off-center SEM (IC2) lacking an RPQ.
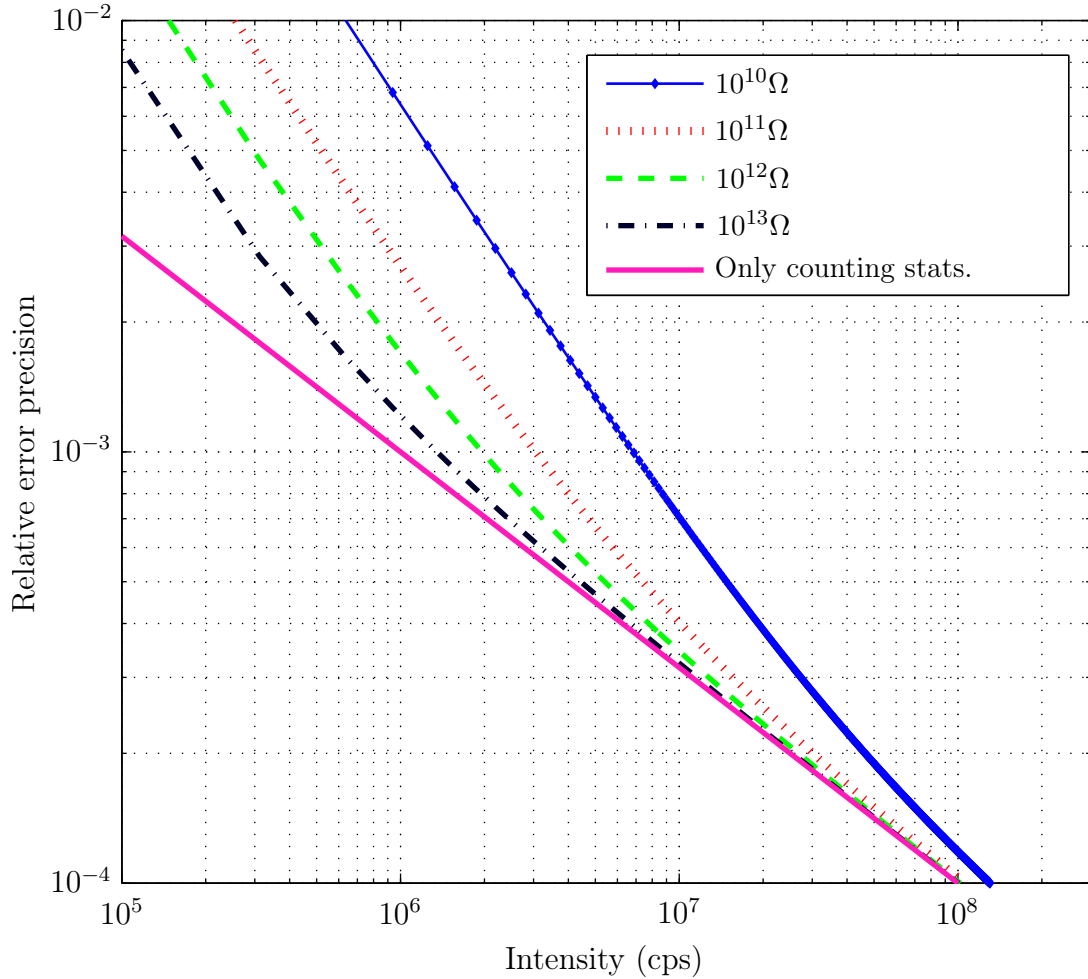
Figure 4.1: Relative error precision as a function of counting statistics and signal-to-noise ratio versus intensity in cps (62,500 cps $\widehat{=}$ 1 mV). With increasing intensity the relative error decreases. The different ohmic amplifiers at the Faraday cups show that the highest resistor with $10^{13}\,\Omega$ converged with lower intensities to the counting statistics limit in comparison to the lower ohmic resistors as its signal-to-noise ratio is the lowest (see. Tab. 4.1).

A signal of 50 V for ^{238}U and of 1 V for ^{232}Th provide a detectable count rate on each half-mass. As the relative tailing changes with measurement time, background zeros are monitored over the course of the measurement day.

Fig. 4.2 shows the relative tailing from the isotopes ^{238}U and ^{232}Th either on the SEM (with RPQ) or on the SEM IC2 (without RPQ). The abundance sensitivity of the ^{238}U tail improves by an order of magnitude (e.g., amu 234: RPQ/IC2 ≈ 0.14), but does not for the ^{232}Th tail (RPQ/IC2 ≈ 0.25). The daily variation of the relative tailing lies between 3 to 30 % (date 09/05/2016; black curves; standard deviation versus mean) and increases up to 50 % during a two month monitoring. The high variation on long-term scale is the result of low measured tailing intensities (~ 30 to 15,000 cps), the instrument's tuning induced changes of focusing characteristics, and the error on interpolation on full masses done by a piecewise cubic Hermite interpolating polynomial (pchip). While a small 3 % daily shift is legitimate, as other laboratories claim a < 5 % shift (Cheng et al. [2013]), the 30 % is particularly high and needs to be thoroughly monitored in the future.

In Fig. 4.3 a dependency on beam intensity of the ^{238}U tail cannot be observed, as daily variation is up to 30 % and because all ratios shown are in between $3\,\sigma$ errors. This legitimates the use of only one standard solution with only one intensity (e.g. ~ 50 V for ^{238}U and ~ 1 V for ^{232}Th) for tailing determination in every day routine work.

How the observed tailing variations affect accuracy is discussed as follows. The sensitivity of the ages and the activity ratios of the four samples are simulated as a function of the variation of the tailing. Here, the sample measurements are corrected by tailing factors that vary in their extent, i.e. the average correction factors on each isotope are uniformly multiplied by $\alpha = 0, 0.1, 0.2, 0.3,...,$ and 3.0. Whereas the multiplication of 1.3 (0.7) and 1.5 (0.5) simulates the maximum daily and monthly variation of 30 %, and 50 %, respectively.

In Fig. 4.4 the influence on the tailing variation on the activity ratios is plotted. Here, the $(^{234}\text{U}/^{238}\text{U})$ and the $(^{230}\text{Th}/^{238}\text{U})$ varies on ε-scale on a daily and on long-term shift (30 %: 0.7 - 7.0 ε; 50 %: up to 10.0 ε). In this trial the variation of $(^{230}\text{Th}/^{238}\text{U})$ of the C09-2 sample is excluded, as this sample, due to its particular low intensities (20 cps for ^{230} Th) varies between 1.4 to 8.5 ‰. The extent of the variation on the activity ratios is dependent on signal intensity, as the impact on activity ratios increases for lower intensities of the low abundant isotopes of ^{234}U and ^{230}Th and similarly for high intensity ^{238}U beams. The error bars in Fig. 4.4 are measurement errors. As the maximum daily shift of 30 % is within those measured $2\,\sigma$ errors, the error estimation regarding tailing correction seems legitimate for those samples.

While we already saw that the activity ratios are affected on ε-scale supporting ε-precision on errors stemming from daily and long-term tailing variance, it is still interesting to see how much these variation affect ages. Fig. 4.5 and 4.6 show a simulation of the influence of the tailing correction on age. Plotted is the influence of α on the activity ratios as a function of age. Here, each square corresponds to an
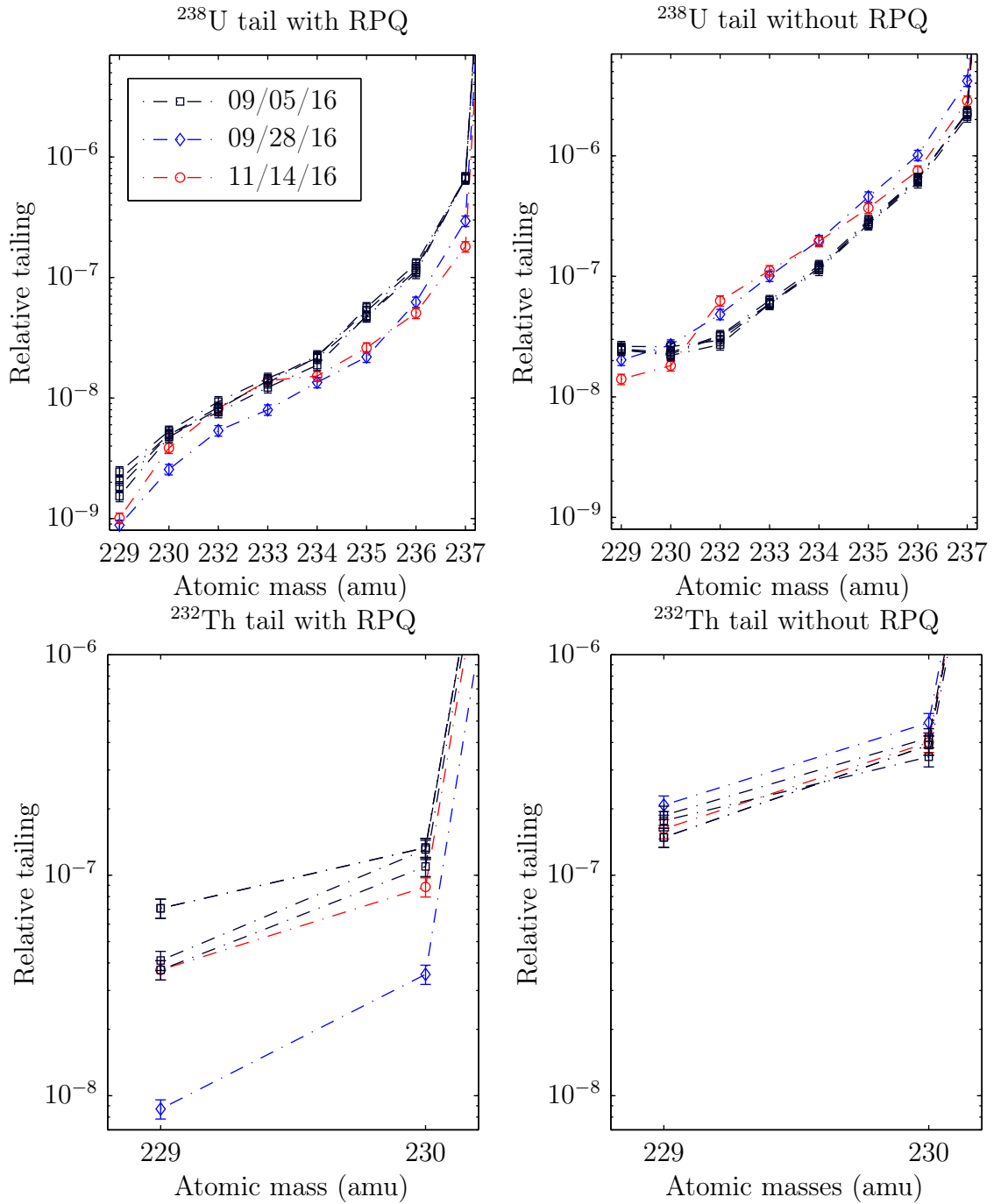
Figure 4.2: Relative tailing of ^{238}U and ^{232}Th. Measurements on three different days are shown spanning a two month interval (long-term). The ^{238}U tail shows daily variance, i.e. standard deviation versus mean, between 3 to 20 % (black) and between 14 to 43 % on a long-term scale. The ^{232}Th tail varies between 8 to 30 % on a daily-scale (black) and between 12 to 51 % on a long-term scale. The abundance sensitivity is improved by a factor of 0.12 to 0.25 using an RPQ.

Figure 4.3: Tailing on half-masses as a function of ^{238}U beam intensities. The ratios of two tailing values from CRM 112-A standard solutions with different dilutions were used. No dependencies of these ratios on beam intensities are observed as all ratios are within $3\,\sigma$ and daily variations of $30\,\%$ are possible. These results support the use of only one standard concentration for tailing determination.
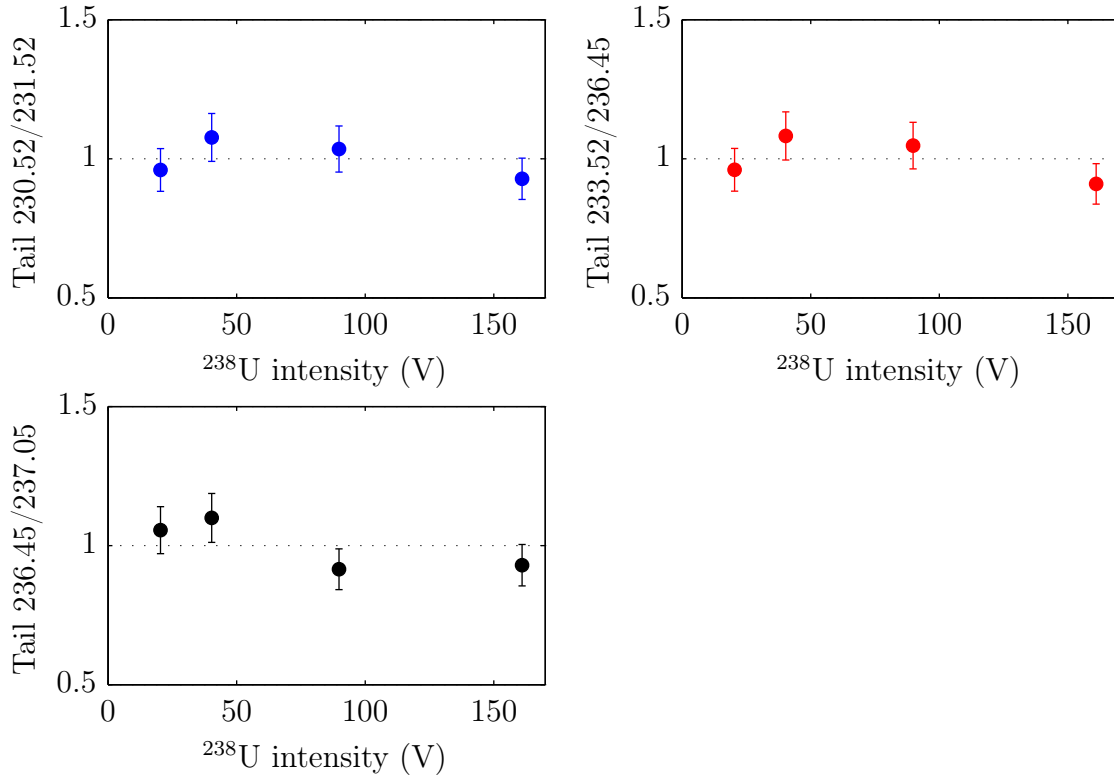
$\alpha = 0.1$ variation of the tailing correction factors beginning with $\alpha = 0$ and in the bottom left corner of the plots. The x and y axes values of the two figures decrease with increasing α values according to Fig. 4.4. The boxes represent the shift in age when varying the tailing correction factors by 30 and $50\,\%$ (small and big box), while the arrows and their corresponding numbers represent the maximum possible shift in age when varying the tailing correction factors by 30 and $50\,\%$ (small and big arrow). Emmertal3 and GeoB show, that the maximum daily shift in age (which is along the small arrow) is on ε-scale up to $8\,\varepsilon$-units (Fig. 4.6). As SPA-52 is the oldest sample and has the highest ^{238}U intensity the shift in age is largest, which is $14\,\varepsilon$-units in age for a maximum daily variation (Fig. 4.5 bottom). Sample C09-2 is excluded in this consideration. A maximum daily shift in age of $1.3\,\%$, i.e. $5\,\mathrm{a}$ can occur (Fig. 4.5 top). The sample solution of C09-2 contained $\sim 4\,\mathrm{fg/ml}$ ^{230}Th stressing the limits of U-series dating. Isotope ^{234}U is measured on a FC for sample GeoB which implies a higher tailing correction on that isotope (see Fig. 4.2 top) in contrast to sample Emmertal3. This explains the higher shift in age for sample GeoB.
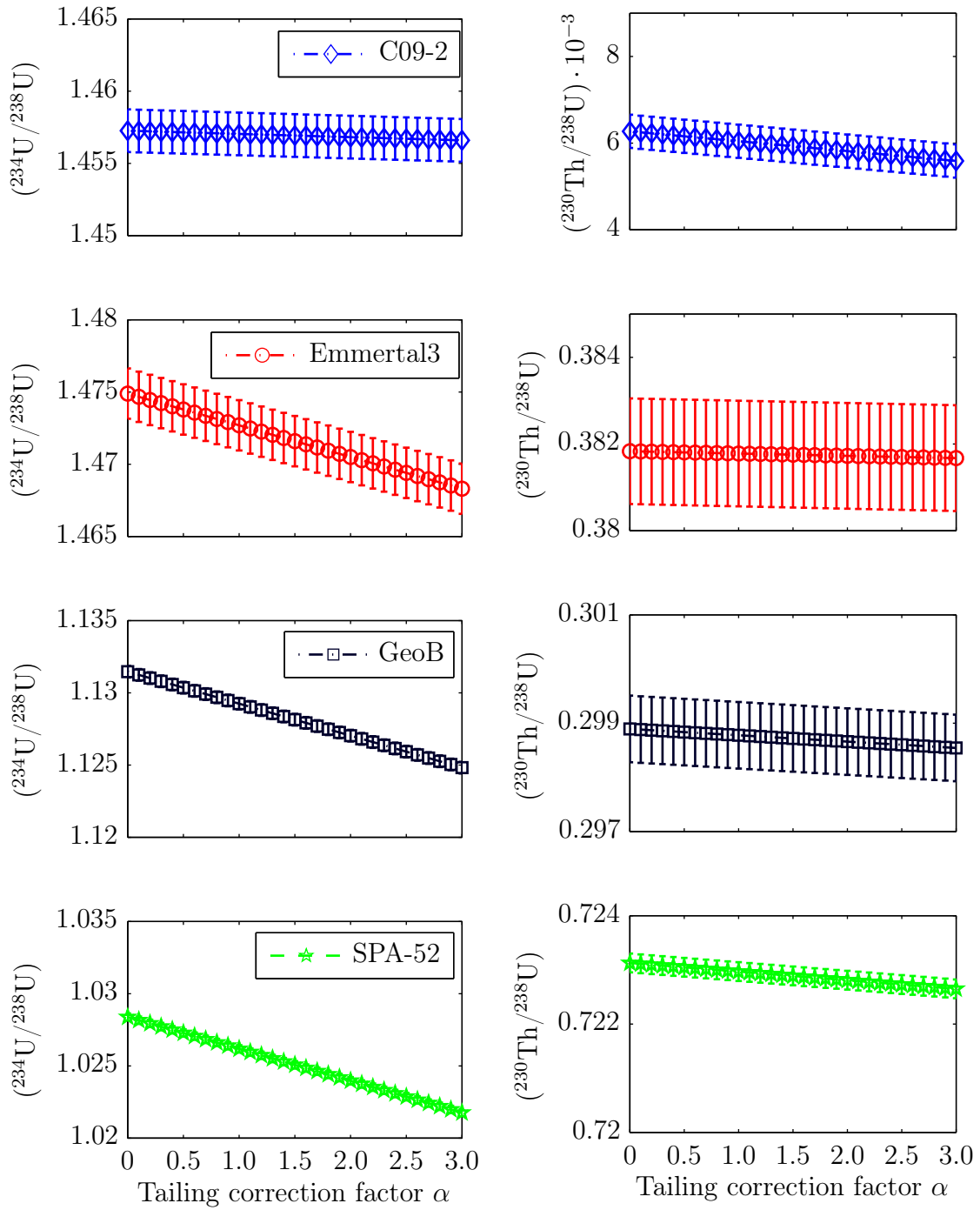
Figure 4.4: Activity ratio sensitivity as a function of tailing correction extent. $(^{234}\text{U}/^{238}\text{U})$ and $(^{230}\text{Th}/^{238}\text{U})$ varies most for C09-2 as this one has very low intensity. 30 % daily tailing variation extent changes $(^{234}\text{U}/^{238}\text{U})$ only up to $7\,\varepsilon$ for all samples. The measurement errors are $2\,\sigma$.
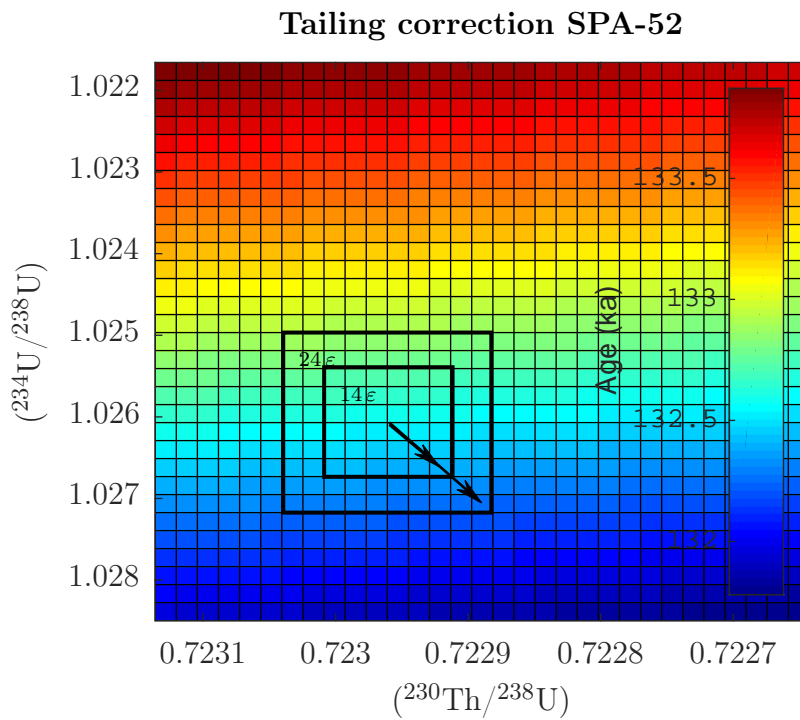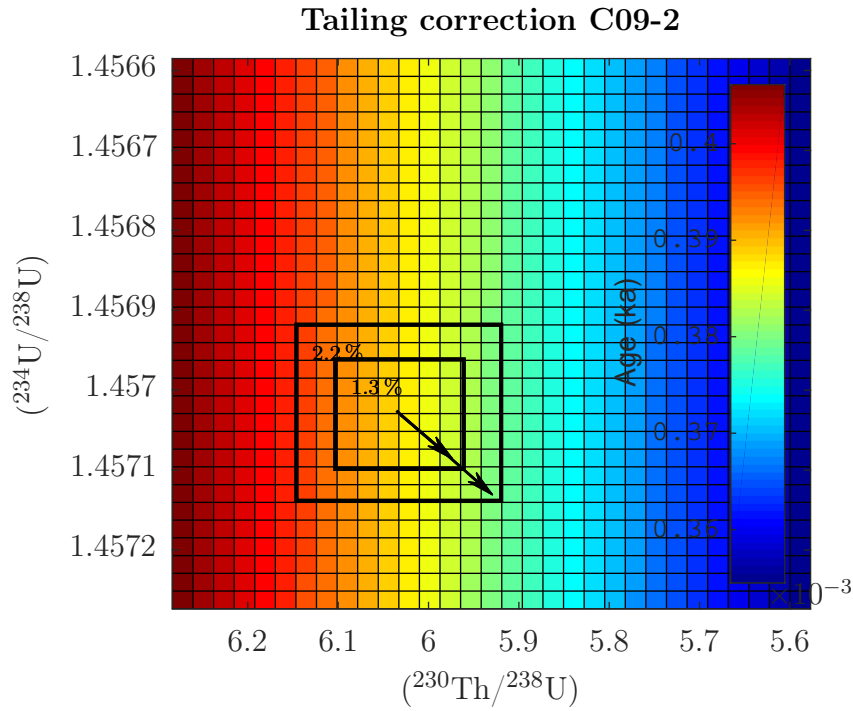
Figure 4.5: Influence of tailing induced activity ratio variation on age for sample C09-2 and SPA-52. Each square corresponds to an $\alpha = 0$, 0.1, 0.2,..., 3.0 tailing correction shift beginning from bottom left. Note that x and y axes values decrease according to Fig. 4.4. The arrows symbolize with their size a 30 and 50 % shift of the tailing correction and its maximum effect on age accuracy. Old ages are more sensitive to changes in their activity ratios, so that on a maximum daily 30 % tailing correction shift SPA-52 already varies $> 10\,\varepsilon$. The C09-2 varies daily by maximum 1.3 %, i.e. 5 a limiting the accuracy of tailing correction for samples at detection limit.
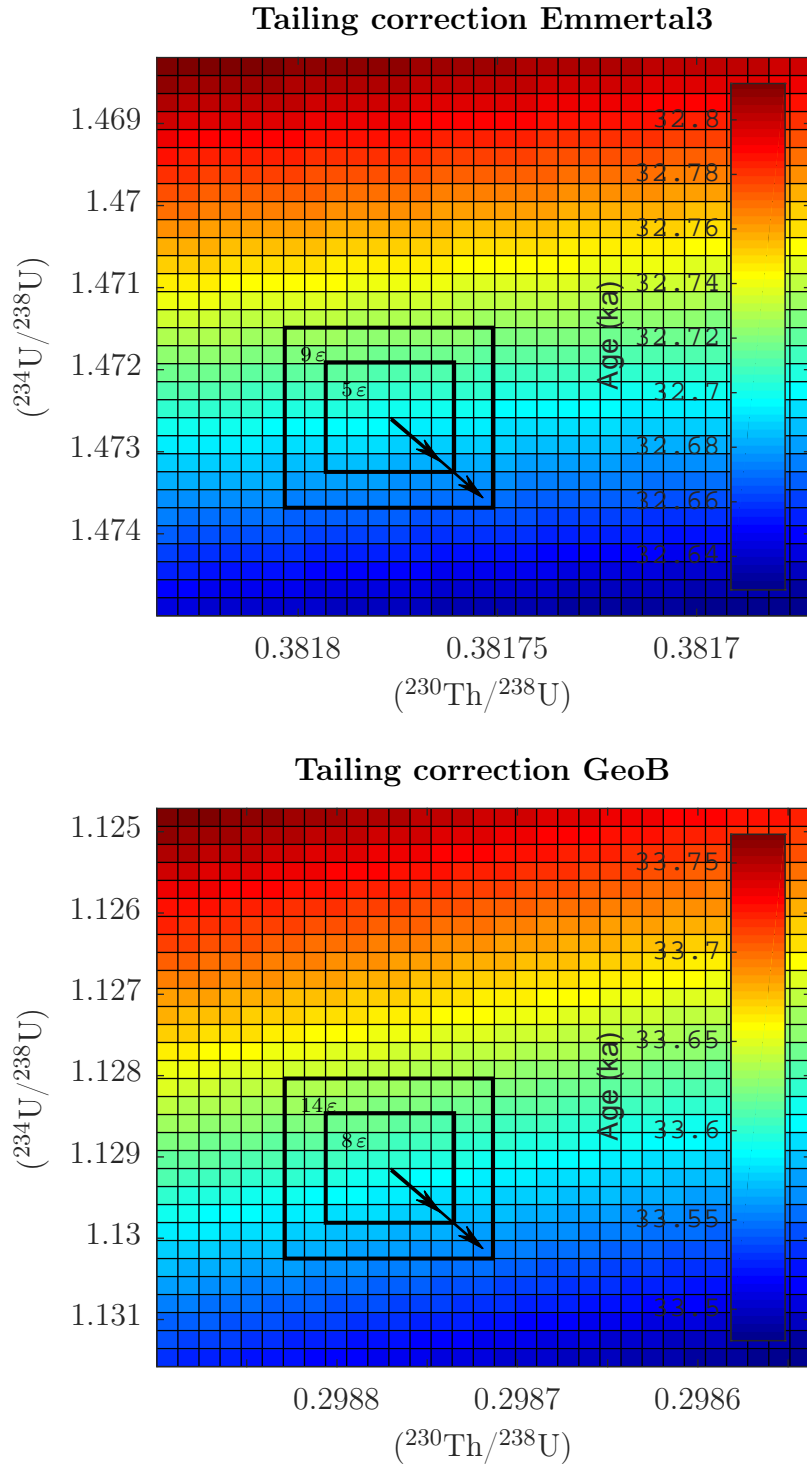
Figure 4.6: Influence of tailing induced activity ratio variation on age determination for sample Emmertal3 and GeoB. Description is the same as in Fig. 4.5. The maximum daily shift affects the age by up to $8\,\varepsilon$-units (small arrow).

4.1.3 U-H$^+$ and Th-H$^+$ corrections

Spectral interferences of neighboring masses on our isotopes of interest limits precision. These interferences are H$^+$, ^{16}O$^+$, or ^{16}OH$^+$ (either from water or air), which occur at 1, 16, and 17 mass units, respectively, higher than the element's mass. As our isotopic system includes mainly the masses 229 to 238, i.e. nine mass units, the system is only corrected for neighboring mass Hydride formations (H$^+$). Loss of intensity on each isotope due to ^{16}O$^+$ or ^{16}OH$^+$ formation do not need to be corrected as we compare and correct our isotopic ratios with standards that are ideally affected by the same spectral loss. Hence, it is important for comparing standards with samples to dilute and spike the standards to the samples' similar intensities and isotopic ratios.

In Fig. 4.7 the mean value of the U Hydride correction factor varies by $1.0 \pm 0.9 \cdot 10^{-5}$ in eight months, while the U Hydride correction factor changes between 0.6 to 100.0 % during one measurement day. Although maximum variance is high, most of the daily measured Hydride correction factors vary only on small scale. Fig. 4.8 shows only U Hydride correction factors, but measurements show that Th Hydride correction factors vary on comparable scales (up to 30 % to each other).

Effects on activity ratios and age when varying the correction factor by $\alpha = 0$, 0.1, 0.2, 0.3,..., 3.0 are shown in Fig. 4.8, Fig. 4.9, and 4.10. The activity ratios (^{234}U/^{238}U) and (^{230}Th/^{238}U) vary only up to 1.4 ε-units considering a daily 100 % variation of the Hydride coefficient. Here, the C09-2's (^{230}Th/^{238}U) varies on percent scale (i.e. 4.7 %) which is, on the one hand still within its $2\,\sigma$ measurement error range but on the other hand a rather high shift. This shows that very young samples with low [Th] are strongly effected by Hydride correction stressing the importance to reduce the intensity of the neighboring isotope ^{229}Th. But if high signals are guaranteed (e.g. Emmertal3 $\sim$ 4,000 cps) the Hydride correction has a minor influence on activity ratios and thus high precision measurements are not limited by Hydride formation.

Fig. 4.9 and 4.10 show that the ages of Emmertal3, GeoB, and SPA-52 vary only by up to 1.5 ε for an $\Delta\alpha = 1$ keeping in mind that this is a maximum possible daily shift as variation are usually less than $\Delta\alpha = 0.1$. C09-2 varies by 6.2 % in age, which corresponds to an age error of 24 a. Here, it is obvious that a correctly determined Hydride factor is necessary, as its effect on measured age is high.
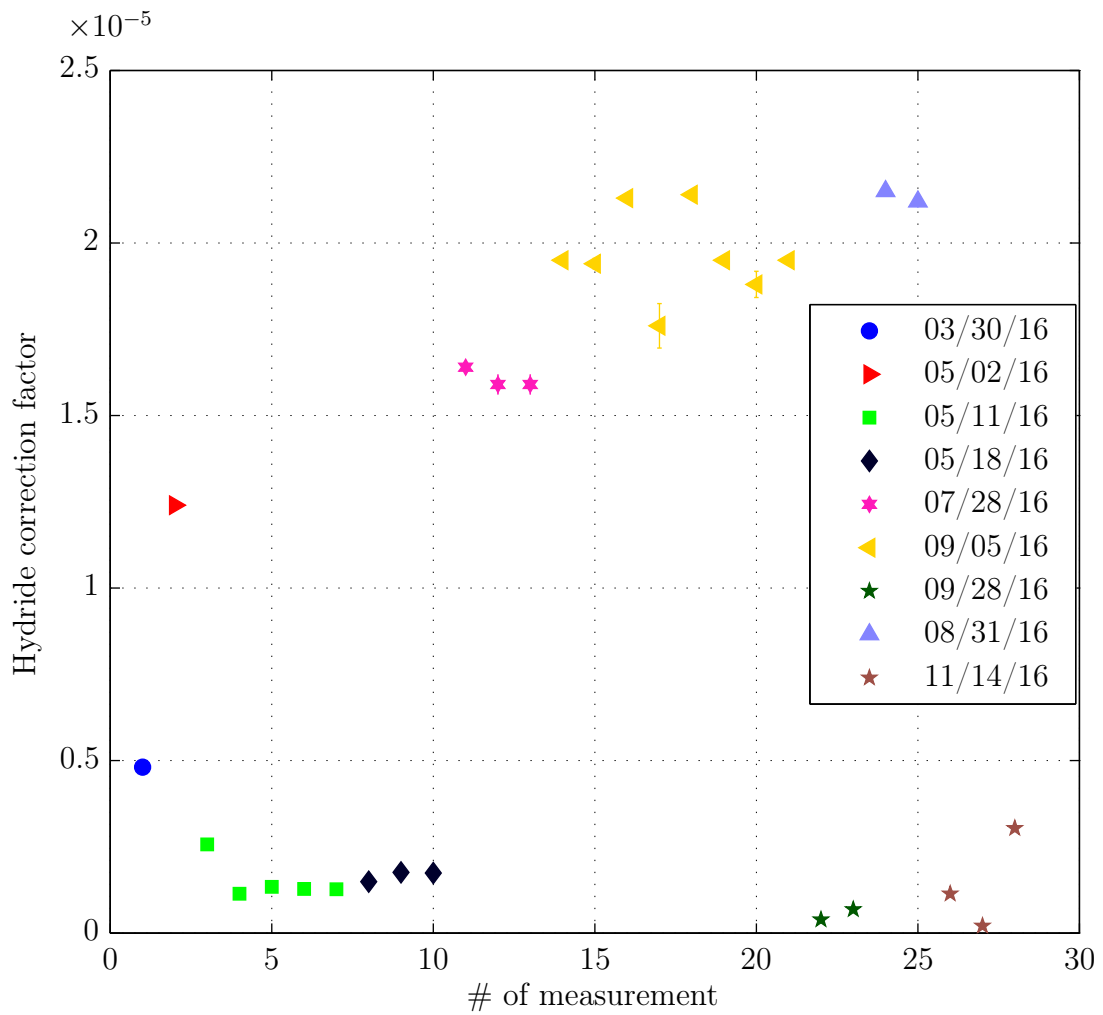
Figure 4.7: Long-term monitoring of the UH$^+$ formation. The Hydride coefficients span a time range of eight months. The coefficients vary long-term by 90 % and between 0.6 to 100 % on a daily basis.
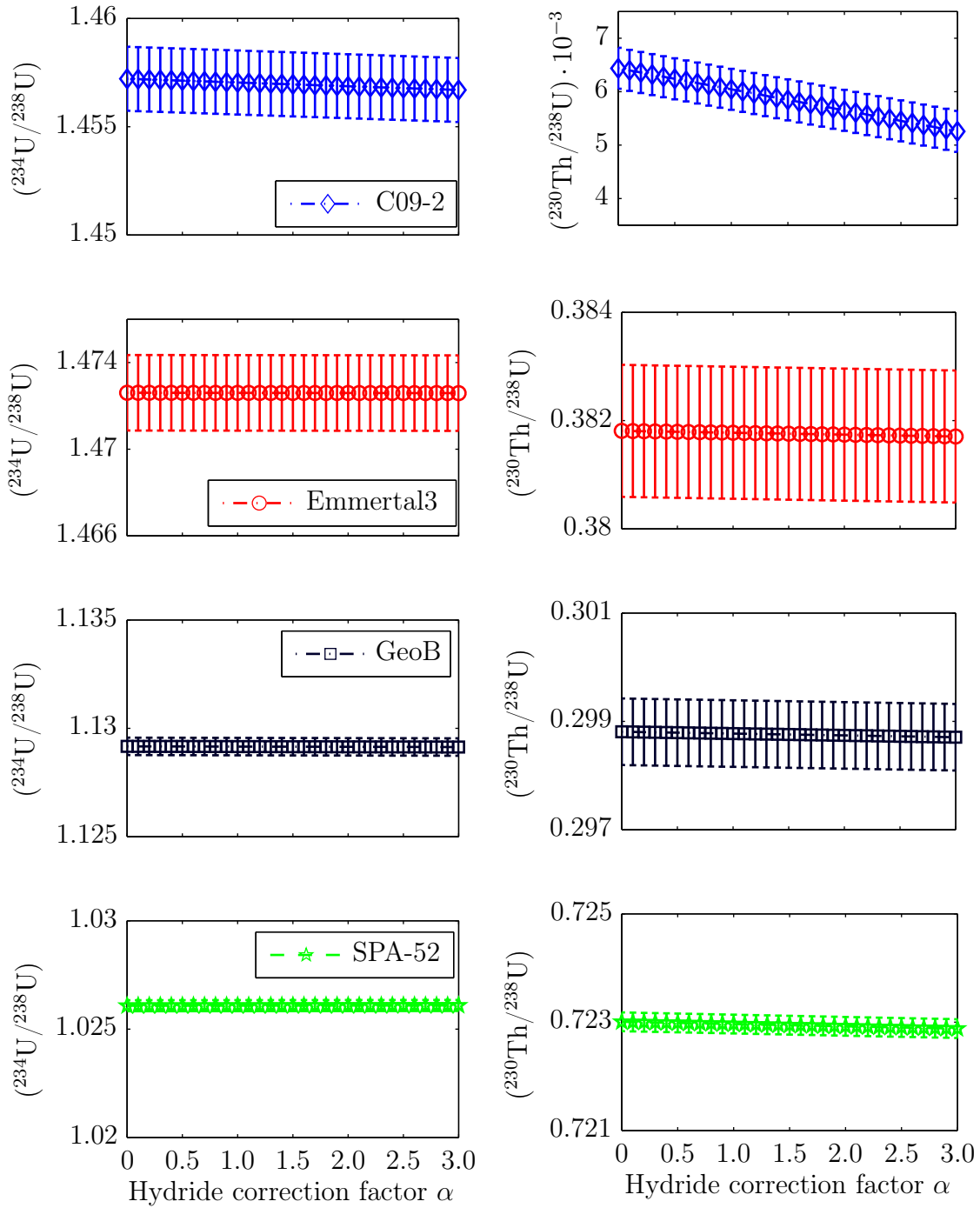
Figure 4.8: Activity ratio sensitivity as a function of Hydride correction extent. $(^{234}\text{U}/^{238}\text{U})$ and $(^{230}\text{Th}/^{238}\text{U})$ varies most for C09-2, the latter activity ratio even on percent scale, stressing the impact of Hydride correction on samples with tremendously low Th intensity. 100 % daily variation in Hydride correction extent changes activity ratios only up to $1.1\,\varepsilon$ for the other three samples. The measurement errors are $2\,\sigma$.

Hydride correction C09-2

Hydride correction SPA-52
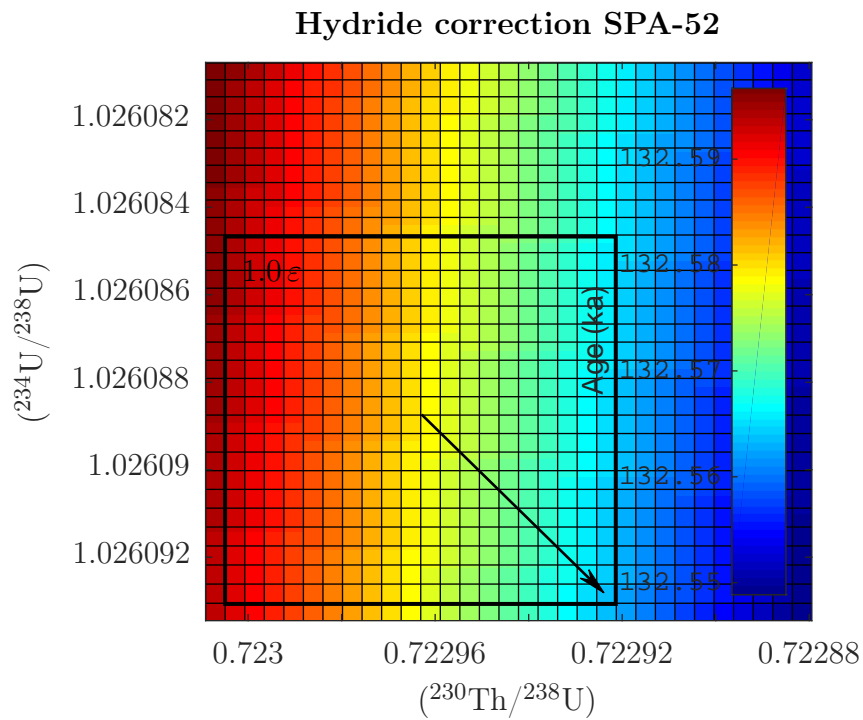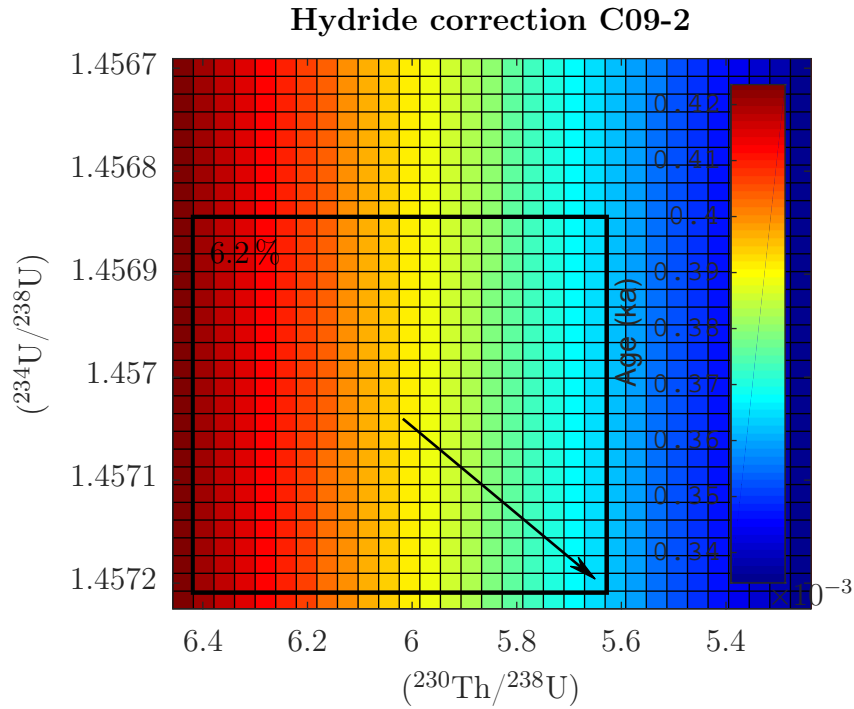
Figure 4.9: Influence of Hydride correction induced activity ratio variation on age for sample C09-2 and SPA-52. Each square corresponds to an $\alpha = 0$, 0.1, 0.2, 0.3,..., 3.0 beginning from bottom left. Note that x and y axes values decrease according to Fig. 4.8. The arrow symbolizes with its size a maximum 100 % shift of the Hydride correction and its maximum effect on age accuracy. The young C09-2 varies by 6.2 % which corresponds to 24 a by changes of 100 % of the tailing correction.
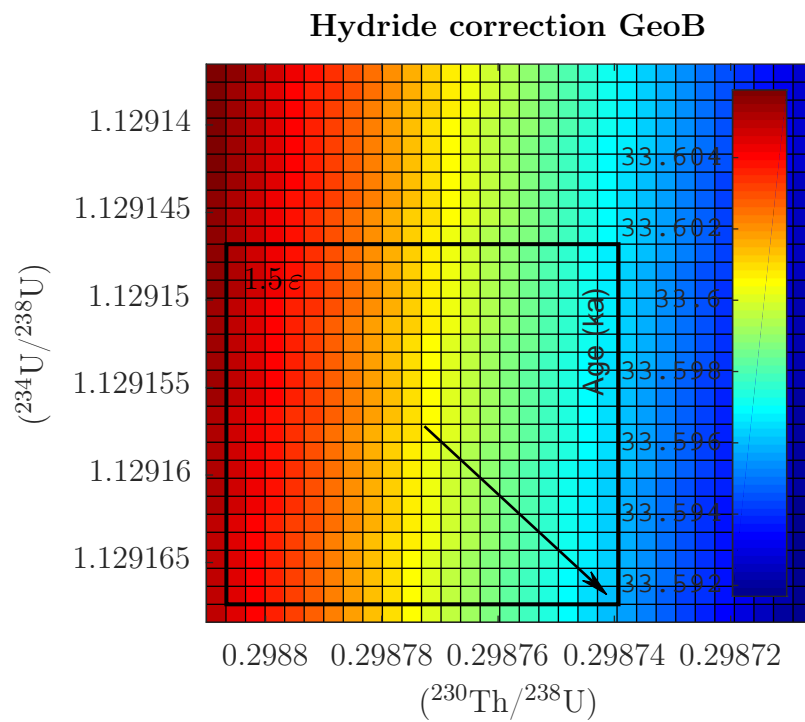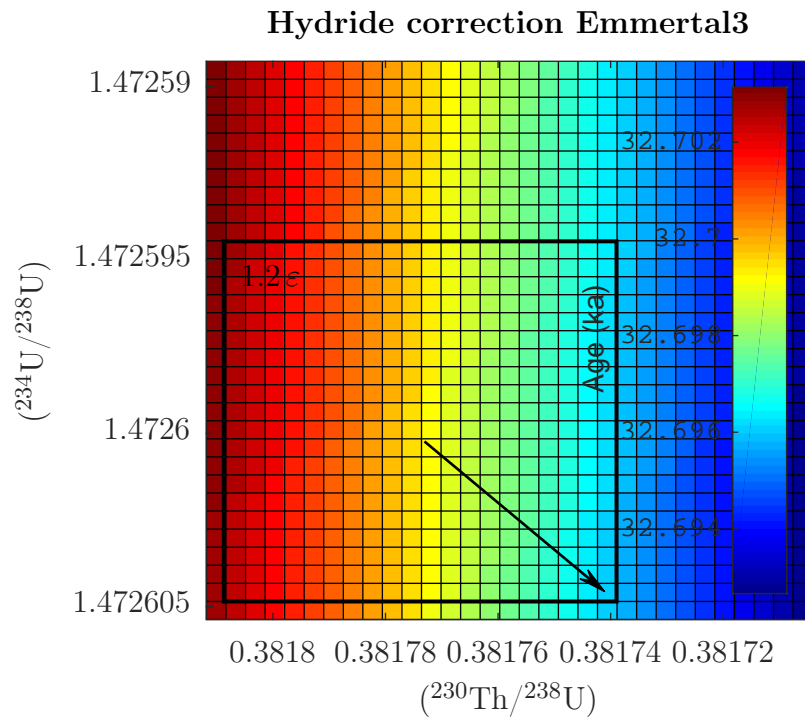
Figure 4.10: Influence of Hydride correction induced activity ratio variation on age for sample Emmertal3 and GeoB. Description is the same as in Fig. 4.9. Hydride correction does not have a high impact on age variation, as a shift of $\Delta\alpha = 1$ varies the age on low $< 1.5\ \varepsilon$-scale.

4.1.4 Process blank correction

To prevent memory effects, background signals are normally quickly reduced through acid washouts between measurements. The rinsing time is a function of the applied intensities, mostly determined by the less-mobile element Th, which usually requires several minutes. The process blank is subtracted from each isotope's measured intensity and thus, an insufficient rinse limits precision. To avoid this needless systematic error it is necessary to decrease the extent of the process blank to the level of an ε-unit with regard to the sample's intensity.

If measuring a series of samples lasting several hours, an increase in the process blank may occur, therefore, the impact of the process blank amount on activity ratios is examined in this section. In the following discussion a regular low process blank is applied to the samples (Tab. 4.2). For sample C09-2, Emmertal3, and GeoB the blank is increased by $\alpha = 0$, 0.5, 1.0, 1.5,..., 5.0 simulating the realistic increase of process blank during their measurement series. This contrasts with the process blank for SPA-52 which, due to its high intensities, is examined with an increase of $\alpha = 1$, 5, 10, 15, 20, 25, 30,..., 40.

The impact of the activity ratios is shown in Fig. 4.11. Obviously, $(^{230}\text{Th}/^{238}\text{U})$ is more affected by process blank correction as isotope ^{230}Th has the lowest intensity. $(^{234}\text{U}/^{238}\text{U})$ is affected by less than $1\,\varepsilon$-unit for Emmertal3, GeoB and SPA-52, and by up to $4\,\varepsilon$ for C09-2 (for maximum $\alpha = 5$ or 40, respectively). If count rates are above 10,000 cps the $(^{230}\text{Th}/^{238}\text{U})$ again varies by less than $1\,\varepsilon$-unit for the highest α values, namely $\alpha = 5$ (GeoB) and $\alpha = 40$ (SPA-52). C09-2 with its 40 cps in isotope ^{230}Th varies by up to 11 %. But Emmertal3 with 4,000 cps in isotope ^{230}Th varies from $4\,\varepsilon$ up to $20\,\varepsilon$-units ($\alpha = 2$, 3, 5). This stresses the importance of sufficient rinsing times for samples with low intensities.

The variation on age with process blank is demonstrated in Fig. 4.12 and 4.13. C09-2 varies by 5 %, i.e. 20 a, only by increasing the blank by $\alpha = 2.0$. Also sample Emmertal3, which has a few thousands cps on isotope ^{230}Th is affected by $4.6\,\varepsilon$-units in age when varying α by 2.0. GeoB, in contrast, varies by $0.5\,\varepsilon$ when increasing the process blank by $\alpha = 2.0$ and sample SPA-52 is affected by a shift of $1.5\,\varepsilon$ in age when increasing α from 1 to 20.

Process blank has only a minor influence for isotopes measured with intensities above 10,000 cps. But if isotopes are measured with less than 10,000 cps, an appropriate rinsing time is necessary and helps prevent inaccuracy in age. Emmertal3 shows a process blank is best for $^{230}\text{Th} < 0.8\,\varepsilon$-units of the intensity.

Table 4.2: Process blank indicating a clean state of the instrument without memory effect. ^{230}Th is generally below 1 cps when starting a measurement series.

| ^{229}Th	^{230}Th	^{233}U	^{234}U	^{235}U	^{236}U	^{238}U
5 cps	0.7 cps	$1 \cdot 10^{-7}\,\text{V}$	2 cps	$3 \cdot 10^{-7}\,\text{V}$	$3 \cdot 10^{-7}\,\text{V}$	$4 \cdot 10^{-4}\,\text{V}$
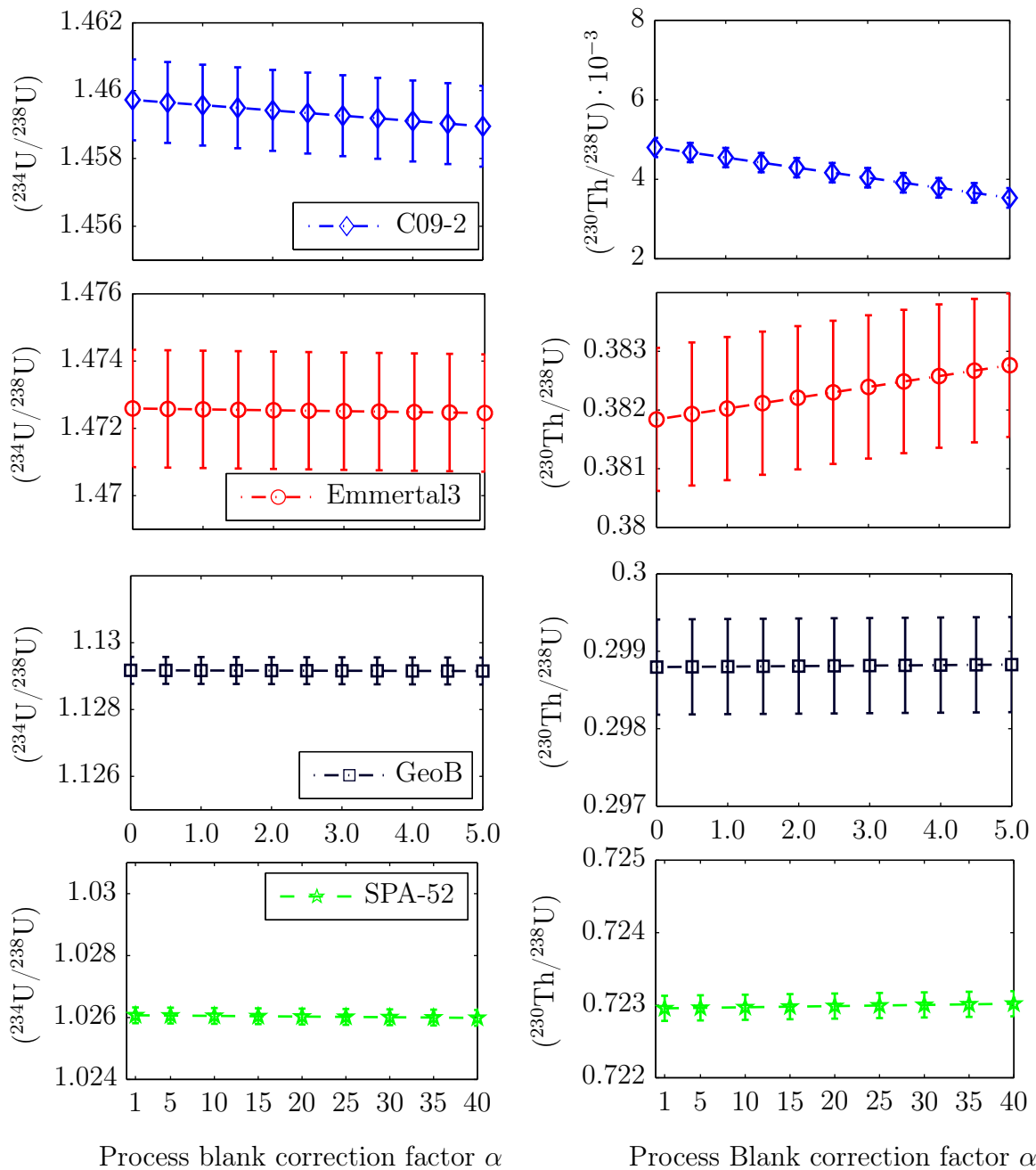
Figure 4.11: Activity ratio sensitivity as a function of process blank correction extent. $(^{234}\text{U}/^{238}\text{U})$ and $(^{230}\text{Th}/^{238}\text{U})$ varies most for samples with low intensities such as sample C09-2 and Emmertal3, with the former's activity ratio varying on the percent scale, stressing the impact of process blank correction for samples with tremendously low Th intensity. The measurement errors are $2\,\sigma$.
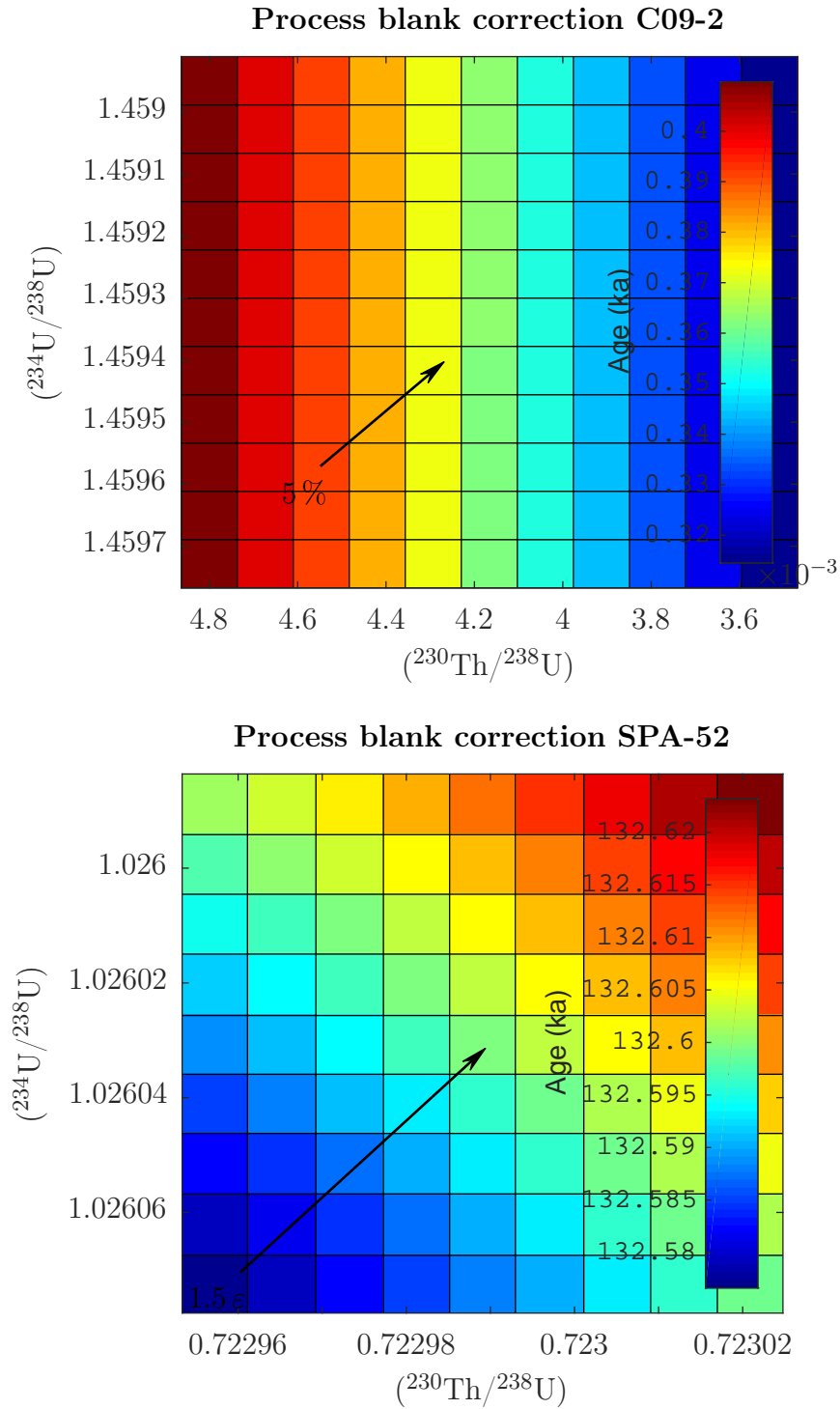
Figure 4.12: Influence of process blank induced activity ratio variation on age for sample C09-2 and SPA-52. Each square of C09-2 correspond to an $\alpha = 0$, 0.5, 1.0,..., 5.0 and for SPA-52 to an $\alpha = 1, 5, 10,..., 40$, respectively, beginning from bottom left. Note that x and y axes values in- or decrease according to Fig. 4.11. The arrows of C09-2 correspond to $\alpha = 1$ to 2.0. The arrows for SPA-52 correspond to $\alpha = 1$ to 20.

Process blank correction Emmertal3

Process blank correction GeoB
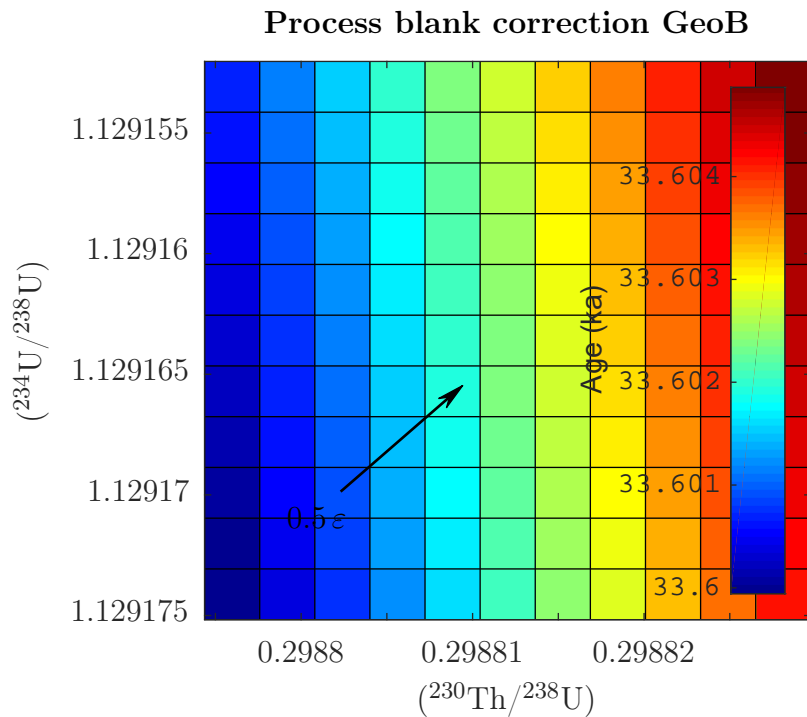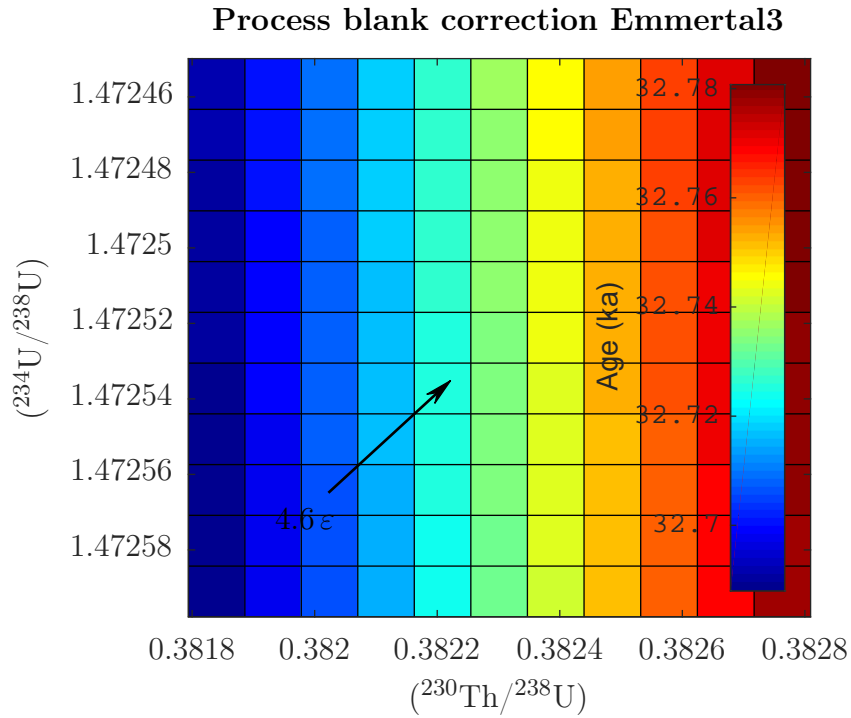
Figure 4.13: Influence of process blank induced activity ratio variation on age for sample Emmertal3 and GeoB. Each square correspond to $\alpha = 0$, 0.5, 1.0,..., 5.0 beginning from bottom left. Note that x and y axes values in- or decrease according to Fig. 4.11. The arrows correspond to an $\alpha = 1$ to 2.0. The impact on process blank correction is high for samples with low intensities in ^{230}Th and ^{234}U.

4.1.5 Spike accuracy

Ultimately, all U-series dating is limited by the imprecision of the spikes. In Heidelberg we usually use three different types of spikes: (1) the UDop consisting of ^{233}U and ^{236}U, (2) the Th229-01 consisting of ^{229}Th, and (3) the Trispike, a diluted and mixed version of the two. UDop and Th229-01 were calibrated relative to the CRM 112-A and the HU-1 standard. The Trispike was gravimetrically prepared.

The imprecision regarding concentrations of the first two spikes consists of instrumental error (ie), imprecision in weighing (we) and imprecision on the concentration of the CRM 112-A uranium standard (ce). As $ie \gg ce > we$ the assumed total error on the spike concentration is considered to be ie. The imprecision on the concentrations of the Trispike are calculated via error propagation of (ce) of the CRM 112-A and the (we). The assumed errors on our spikes are shown in Tab. 4.3.

In Tab. 4.4 the maximum and average impact of the spike's imprecision on $\left(^{230}\mathrm{Th}/^{238}\mathrm{U}\right)$ and ages are shown. MaxR and SD are the maximum range and the standard deviation of the activity ratios and the ages. $\left(^{234}\mathrm{U}/^{238}\mathrm{U}\right)$ is not affected by spike imprecision as this ratio is directly measured via the $^{234}\mathrm{U}/^{238}\mathrm{U}$ atomic ratio. The spike's imprecision lead to an ε-scale of standard deviation on the $\left(^{230}\mathrm{Th}/^{238}\mathrm{U}\right)$ for young ages, but for older ages it has a non-negligible impact on the activity ratio. As the ages show a high maximum range and hence a high variability, I would recommend recalibrating our spikes on ε-precision to limit the inaccuracy on our ages.

Table 4.3: Spikes with imprecisions used for U-series dating.

Spike name	^{229}Th	^{233}U	^{236}U
UDop		$398.83 \pm 0.27\,\mathrm{pg{\cdot}g^{-1}}$	$47.79 \pm 0.03\,\mathrm{ng{\cdot}g^{-1}}$
Th229-01	$175.87 \pm 0.20\,\mathrm{pg{\cdot}g^{-1}}$		
Trispike	$18.12 \pm 0.01\,\mathrm{pg{\cdot}g^{-1}}$	$38.56 \pm 0.03\,\mathrm{pg{\cdot}g^{-1}}$	$386.78 \pm 0.06\,\mathrm{pg{\cdot}g^{-1}}$

4.2 Machine drift and reproducibility

In this section I will examine whether the reproducibility of our standard measurements allows for ε-precision measurements. The reproducibility is limited by (1) the inherent instrumental statistics mentioned in Sec. 4.1.1, by (2) the above mentioned corrections and by (3) the remaining sources of systematical errors apparent in the persistent machine drift.

The main sources of drift are changes of temperature in electronics, changes in vacuum, abrasion or matrix induced coating of the detector surfaces, change of size

Table 4.4: Spike imprecision's impact on accuracy.

	ATh$_-$	$\overline{\text{ATh}}$	ATh$_+$	MaxR	SD
C09-2	0.007535	0.007541	0.007546	14 ε	7 ε
Emmertal3	0.381529	0.381775	0.382022	13 ε	5 ε
GeoB	0.298582	0.298775	0.298968	13 ε	6 ε
SPA-52	0.721660	0.722965	0.724272	36 ε	18 ε
	Age$_-$ (a)	$\overline{\text{Age}}$ (a)	Age$_+$ (a)	MaxR	SD
C09-2	394 $\pm$ 8	394 $\pm$ 8	394 $\pm$ 8	-	-
Emmertal3	32,678 $\pm$ 74	32,702 $\pm$ 74	32,725 $\pm$ 74	14 ε	7 ε
GeoB	33,580 $\pm$ 46	33,605 $\pm$ 46	33,630 $\pm$ 46	15 ε	7 ε
SPA-52	131,752 $\pm$ 38	132,211 $\pm$ 39	132,673 $\pm$ 39	70 ε	35 ε

ATh$_-$, $\overline{\text{ATh}}$, ATh$_+$ are minimum, average, and maximum (^{230}Th/^{238}U) calculated with minimum, average, and maximum spike imprecision. Age$_-$, $\overline{\text{Age}}$, and Age$_+$ are the corresponding ages calculated with minimum, average and maximum impact of spike imprecisions. MaxR and SD are the maximum range and standard deviation. The measurement errors on age are $2\,\sigma$.

of orifices or matrix induced coating of skimmer and sampler cones, changes in gas mixture/gas flow from the injector system (Aridus), and a changing yield or gain of the detectors. As it is typically not possible to measure ^{234}U and ^{238}U simultaneously within the limits of a standard multiple-Faraday collector array equipped with $10^{11}\,\Omega$ resistors as it is discussed in Sec. 2.5, and therefore normal to measure the minor ^{234}U isotope on SEM or if the signal is $> 50{,}000\,\text{cps}$ (i.e. $0.8\,\text{mV}$ at $10^{11}\,\Omega$) on a $10^{13}\,\Omega$ amplifier. A major problem for measurements using a mixed array is the calibration of the relative yield (SEM) or the gain of the $10^{13}\,\Omega$ amplifier. The yield is generally unstable and must be monitored frequently, in contrast to the relatively stable gain of Faraday detectors.

Regarding the machine drift, simultaneous measurement of isotope ratios, especially isotopes of the same element, is tremendously advantageous since the majority of drift cancels out. The remaining systematical bias is induced by mass discrimination, called mass bias fractionation. Although we correct mass bias via the natural ratio of ^{238}U/^{235}U $= 137.881$ usually not all fractionation correction is covered.

The remaining observed drift is a very complex interplay between the systematic errors. Measuring the single impact of each requires complex measurement setups (e.g., Ulianov et al. [2014]), and so it is nontrivial to correct for yield and gain in particular. For reasons of simplicity the drift, as well as the remaining conglomerate of systematic error, is corrected via standard bracketing; i.e. each sample is bracketed by two standards and the average offset of the two standard's activity ratios is used to correct the sample's activity ratios. This corrects for drift, while any statistical

variation has no impact on the statistics of the sample. Apparently, the reproducibility of the drift corrected standards limit the error on age of the samples. As I focus on ε-precision, I will have a closer look on the numbers, now.

Fig. 4.14 shows the activity ratio $(^{234}\text{U}/^{238}\text{U})$ of standards used for bracketing spanning almost two years (May-15 to Feb-17; $\# = 517$). Furthermore, Fig. 4.14 shows the drift of the standards before and after floating window drift bracketing. The drift corrected histfit shows a normal distribution which supports this approach for drift correction. Before drift correction $(^{234}\text{U}/^{238}\text{U})$ varies by 1.0005 ± 0.0015. After standard bracketing, the external reproducibility of $(^{234}\text{U}/^{238}\text{U})$ is 1.00002 ± 0.00082. The external error is on the same scale as the mean standard error for a single standard measurement, showcasing the correct error prediction during measurements. The internal error is 1.00002 ± 0.00004 still covering the literature value of 1.

Fig. 4.15 top shows the drift corrected $(^{230}\text{Th}/^{238}\text{U})$ for the same time span. Here, the external reproducibility is 1.00004 ± 0.00180 as Th isotopes are not measured simultaneously and with less intensity. The internal reproducibility is 1.00004 ± 0.00008. Fig. 4.15 bottom show that measurements with very high signals can even provide ppm-precision reproducibility ($1\,\text{ppm} = 10^{-6}$). Isotope ^{143}Nd and isotope ^{144}Nd were both measured on standard $10^{11}\,\Omega$ amplifiers with signals close to $1\,\text{V}$. Shown are three measurements days spanning six months (Aug 16 to Feb 17; $\#$ 190). The external reproducibility is $0.51211501 \pm 0.00000340$, which is a precision of $7\,\text{ppm}$ $(^{143}\text{Nd}/^{144}\text{Nd} = 0.512115)$ (the internal precision is $0.51211501 \pm 0.00000002$). These results show that the reproducibility is a function of intensity. Hence, several standards with high intensities above $20\,\text{mV}$ (on a standard $10^{11}\,\Omega$) or above $11\,\text{mV}$ (on a $10^{13}\,\Omega$) were measured, the results are shown in Fig. 4.16. The measurements vary by $6\,\varepsilon$-units which would allow for ε-precision measurements, but requires measurement either with high signals (better) or prolonged measurement times. However, finding samples that provide high [U] and [Th] is very difficult.

The measurements of the samples should always be conducted with maximum available precision. The corresponding standard measurements should be adjusted so that the standards variation matches the sample's precision. In the end the mean standard's error can be used as error for the age, therefore limiting the precision range.
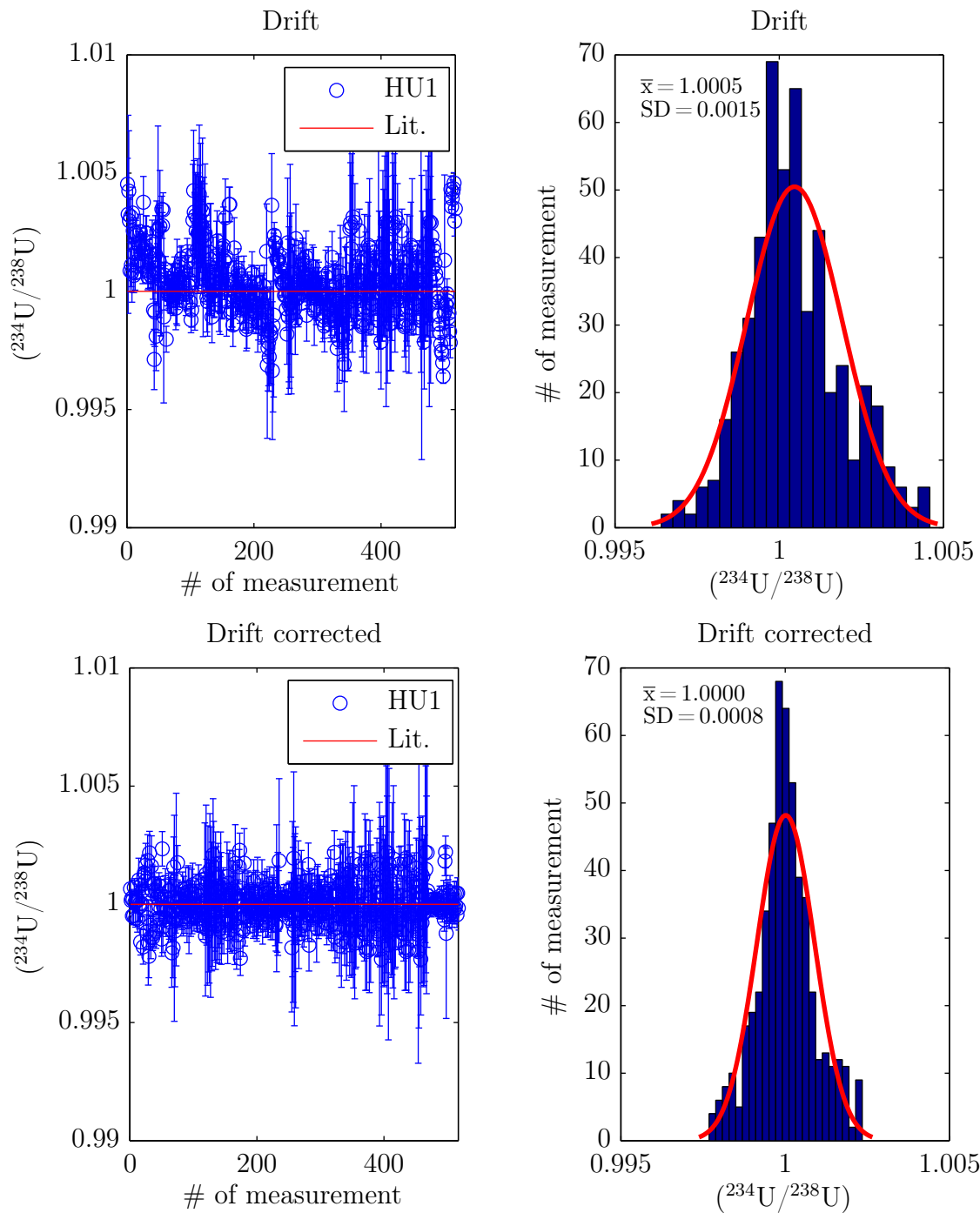
Figure 4.14: Reproducibility of $(^{234}\text{U}/^{238}\text{U})$ from May-15 to Feb-17. Top: Standard measurements without drift correction. Here, the standards scatter on per mil-scale, the histfit shows a drift to higher activity ratios. Bottom: The activity ratios are corrected by floating window standard bracketing; the drift cancels out. The reproducibility is on ε-scale.
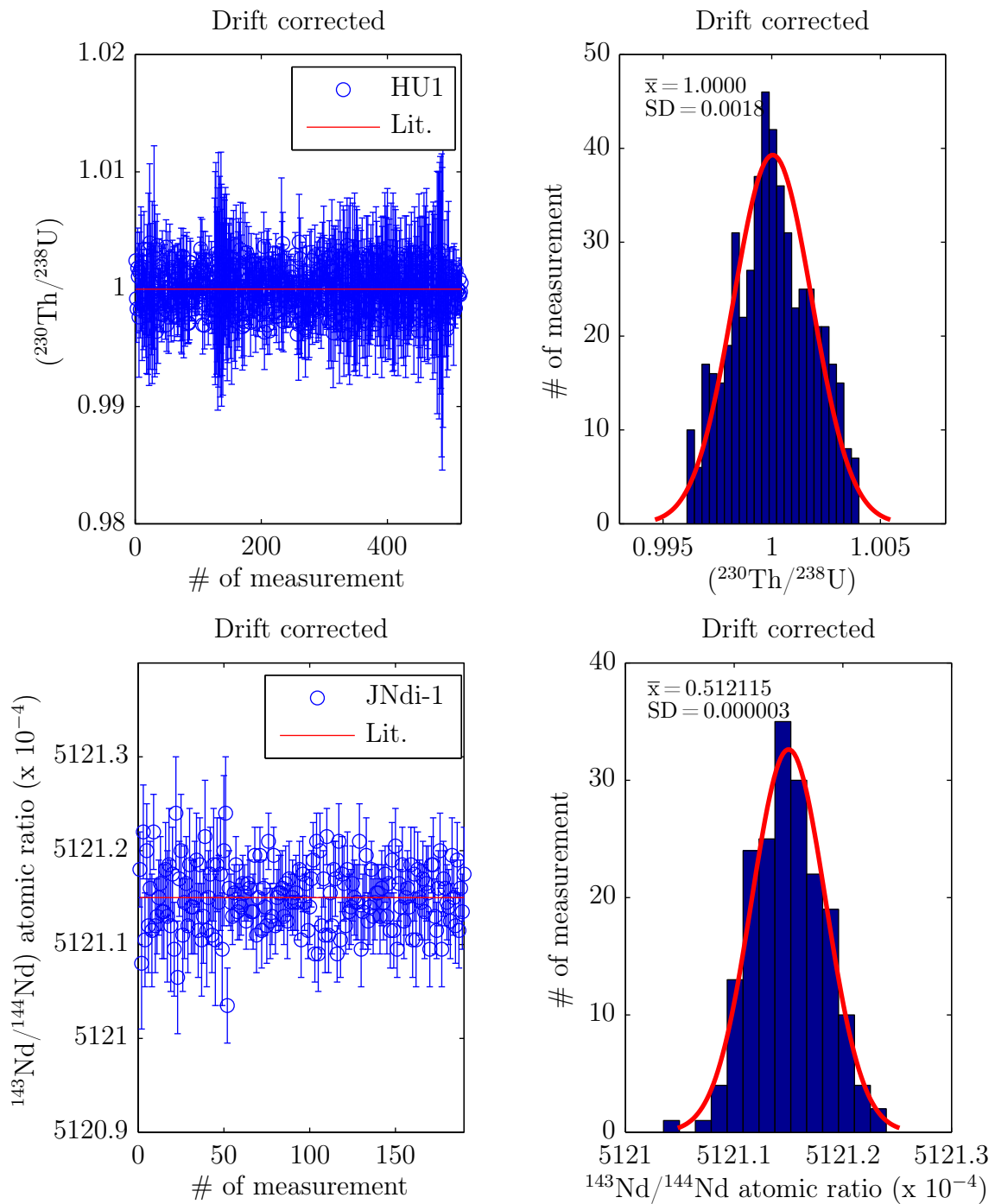
Figure 4.15: Reproducibility of $(^{230}\text{Th}/^{238}\text{U})$ from May-15 to Feb-17 (top) and reproducibility of $^{143}\text{Nd}/^{144}\text{Nd}$ atomic ratio (Aug-16 to Feb-17). Top: Standard measurement with drift correction. Here, the standards scatter on per mil-scale, the histfit shows a normal distribution. Bottom: High intensities lead to ppm reproducibility.
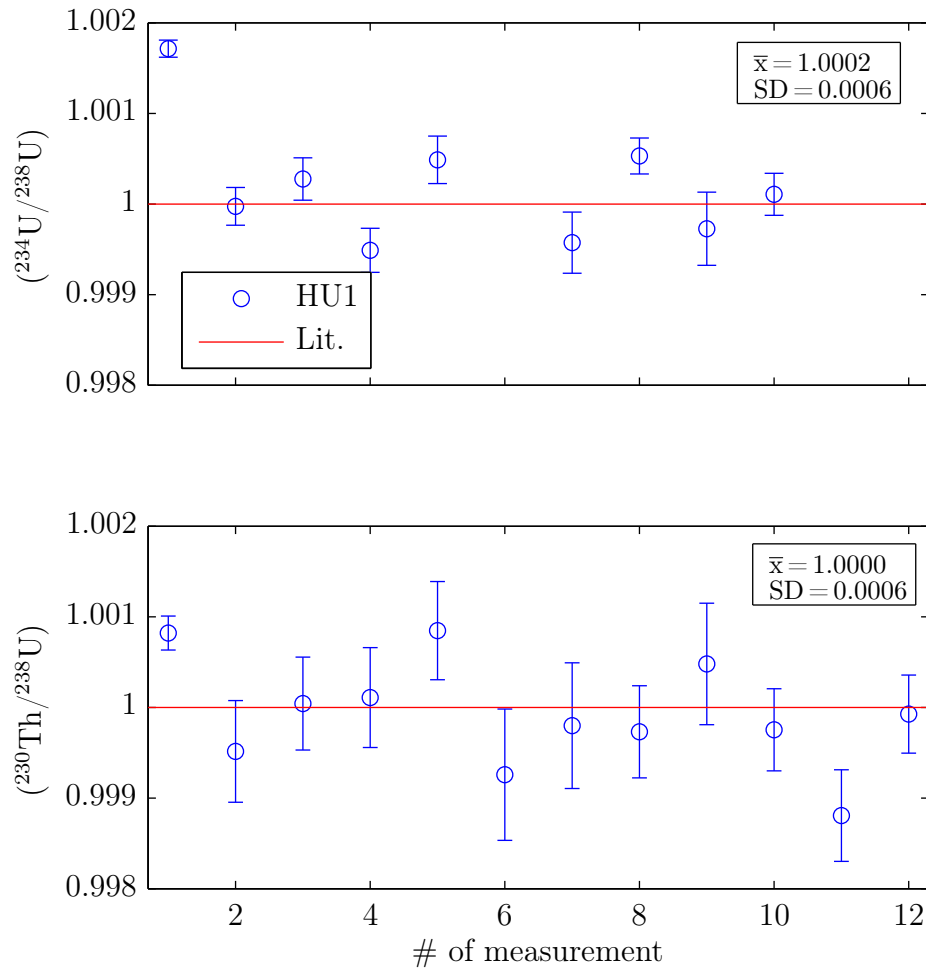
Figure 4.16: Reproducibility of cup measurements. The less abundant isotopes are measured with $> 11\,\mathrm{mV}$. Intensity limits reproducibility; i.e. activity ratios were measured with $6\,\varepsilon$-precision.

4.2.1 Comparison between standard and samples

After introducing machine drift in Sec. 4.2, the question arises whether this drift correction can be applied to samples. As standards are used to imitate samples but with a known concentration of U and Th isotopes, it is crucial that samples and standards are affected similarly by instrumental bias. The difference between samples and standards is the remaining matrix elements in the sample's solution, although the aim of the chemical preparation is to remove matrix from solution. The presence of residual matrix elements can degrade analytical performance. There are essentially two types of matrix-induced interferences: (1) the sample transport effect and (2) the ionization condition effect. The first one is the physical suppression of the analyte signal, brought on by the level of dissolved solids or acid concentration in the sample, caused by the sample's impact on droplet formation in the nebulizer of droplet size selection in the spray chamber or by slowly blocking of the sampler and skimmer orifices leading to long-term signal drift. Organic matrices usually cause variations in the pumping rate due to different viscosities. The second type causes a suppressed signal by varying amounts, depending on the concentration of the matrix components. The ionization conditions in the plasma are so fragile that higher concentrations of acid result in severe suppression of the analyte signal (Thomas [2013]).

Secondary carbonates consist of $\sim 40\,\%$ Ca, Sr, Mg, and trace elements such as transition metals (Mn) or rare earth elements, building up the main matrix elements that need to be removed. Fig. 4.17 shows test on standard solution with added Ca concentrations (1, 5, 10, 100, and 500 ppm), which reveal that below 10 ppm, added Ca did not cause a mass bias effect on the isotopic composition, but U and Th intensity dropped by $10\,\%$. In addition, throughout the analyses of carbonate samples and standard solutions having residual amounts of Ca (less than 10 ppm), no mass bias effect was found. The used chemical preparation procedure (Wefing [2016]) show that on average a Ca concentration of 1.0 ± 0.8 ppm is achieved.

Fig. 4.18 and Fig. 4.19 show standards (HU1) in comparison to samples (batch of GeoB samples). Both, sample (red) and standards (blue), vary by the same $\sim 1.7\,\%$ (standard deviation divided by mean) per measurement (1 measurement: 30 runs), proving that the samples behave in the same manner as standards during measurements. The standards oscillate over time reflecting the instrumental drift. The atomic ratios itself are very stable and vary only by $0.02\,\%$ for the U ratios (as those are high in intensity and are measured simultaneously) or by $0.68\,\%$ for the Th ratios. These numbers support treating standards as samples and the use of standard bracketing itself.
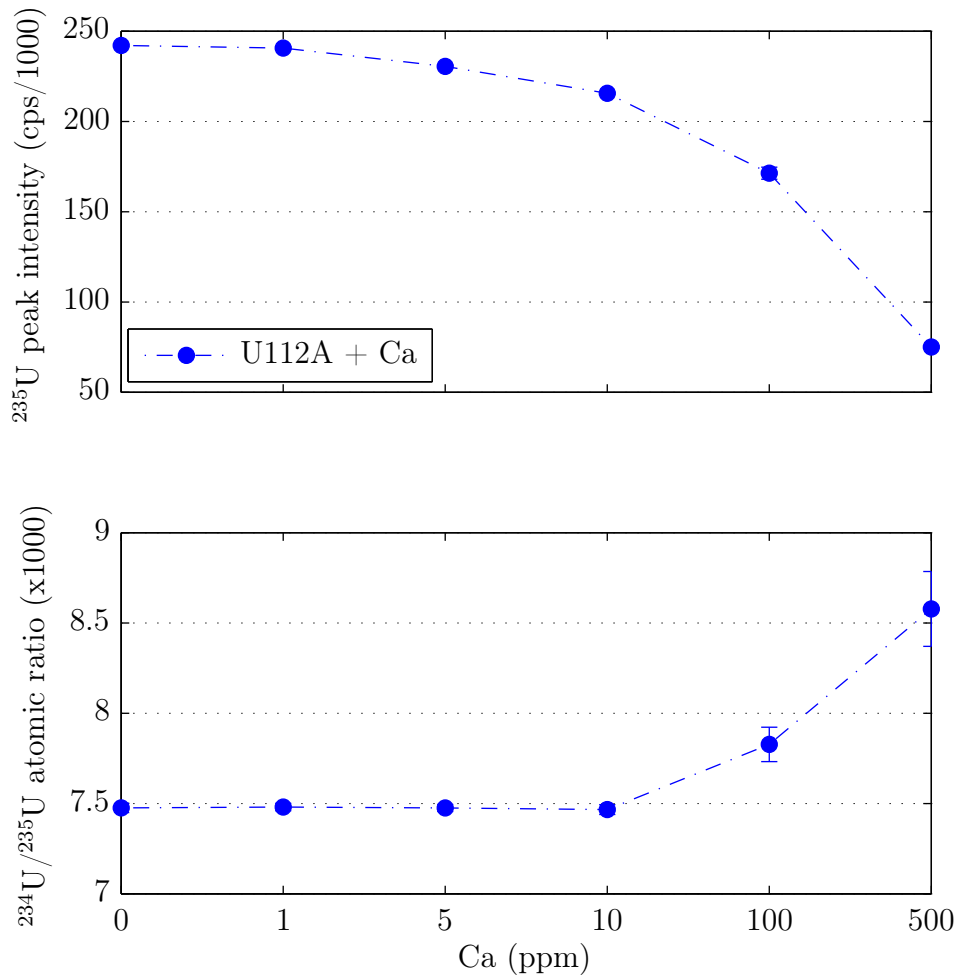
Figure 4.17: Measured ^{234}U/^{235}U atomic ratio of the different CRM 112-A standard solutions doped by various amounts of [Ca]. Below [Ca] = 10 ppm, the ratios are not affected by matrix elements. The peak intensity decreased by 10 %. Our samples are usually measured with [Ca] ≪ 10 ppm.
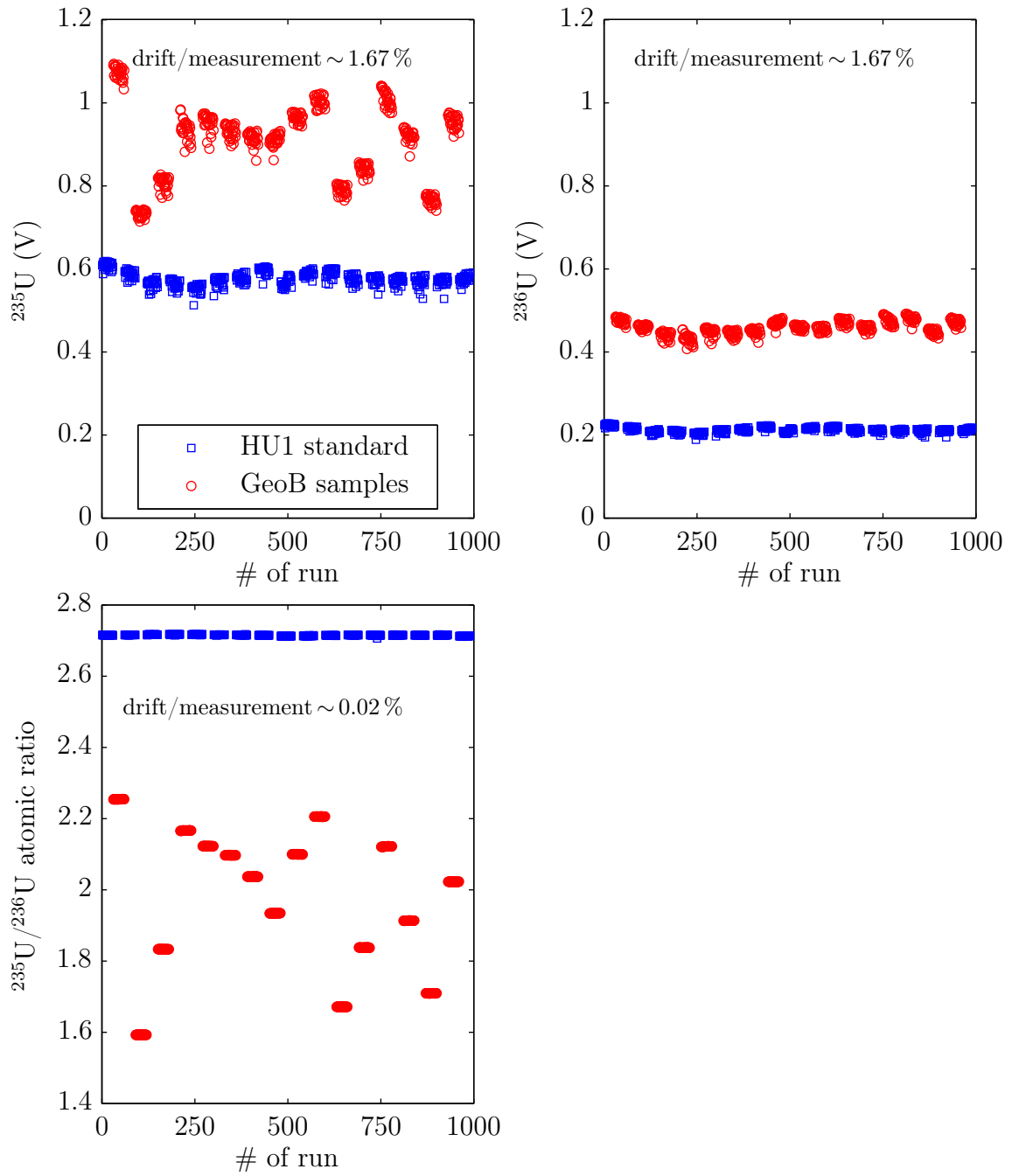
Figure 4.18: Isotope ^{235}U and ^{236}U intensity and ^{235}U/^{236}U atomic ratios of samples (red) and standards (blue). The average drift of each measurement is on the same scale for both standards and samples, supporting standard bracketing as a technique, as well as showing that the samples contained low amounts of matrix elements. The ratios are very stable with a standard deviation of $0.02\,\varepsilon$.
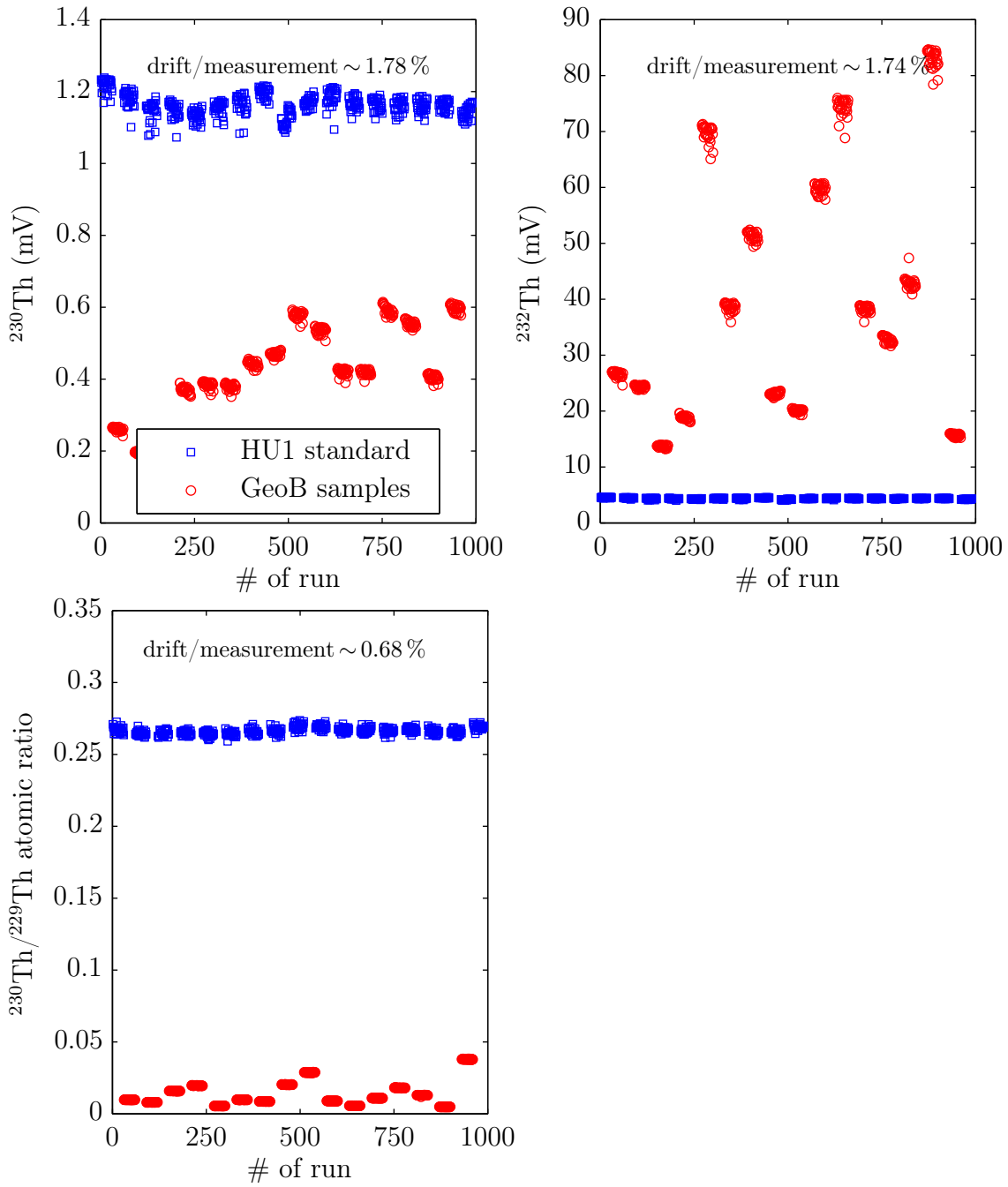
Figure 4.19: Isotope ^{230}Th and ^{232}Th intensity and ^{230}Th/^{229}Th atomic ratios of samples (red) and standards (blue). The average drift of each measurement is on the same scale for both standards and samples, supporting standard bracketing as a technique, as well as showing that the samples contained low amounts of matrix elements. The ratios are very stable with a standard deviation of $0.68\,\varepsilon$.

4.3 Summary ε-precision dating

The results presented in this chapter show that the applied corrections scale on the order of ε-units for regular samples (Emmertal3 and GeoB) but as well for samples with old ages as SPA-52, which is demonstrated by the square sum of the daily maximum variances $e(^{234}\mathrm{U}/^{238}\mathrm{U})$ and $e(^{230}\mathrm{Th}/^{238}\mathrm{U})$ of the common coral sample GeoB:

$$e(^{234}\mathrm{U}/^{238}\mathrm{U}) = \sqrt{e_{tail}^2 + e_{H^+}^2 + e_{PB}^2} = \sqrt{0.9^2 + 0.1^2 + 0.2^2} \cdot \varepsilon \approx 0.9\,\varepsilon, \qquad (4.2)$$

$$e(^{230}\mathrm{Th}/^{238}\mathrm{U}) = \sqrt{e_{tail}^2 + e_{H^+}^2 + e_{PB}^2} = \sqrt{1.1^2 + 1.1^2 + 0.9^2} \cdot \varepsilon \approx 1.8\,\varepsilon. \qquad (4.3)$$

Here, e_{tail}^2, $e_{H^+}^2$, and e_{PB} are the daily maximum variance of the activity ratios induced by tailing, H^+, and the process blank. Also, the daily variance effects on the corresponding ages range on ε-scale besides for the tailing correction for sample SPA-52. I would like to remember at this point that only maximum variances are considered and the daily tailing variance ranges between 3 up to 30 %.

In the above mentioned assumptions, spike imprecision and considerations about the reproducibility of the activity ratios are excluded as both scale on a low per mil level. However, corrective actions like recalibration of the spikes for ε-precision would guarantee U-series dating on such a highly precise scale. Furthermore, as Fig. 4.15 bottom and 4.16 prove, a standard reproducibility on ε-precision (even ppm) is possible if the signals on the detectors are $> 11\,\mathrm{mV}$.

Table 4.5: Idea for a future measurement protocol.

Faraday cups	L1	Center	H1	H2	H3
amplifier	$10^{13}\,\Omega$	$10^{13}\,\Omega$	$10^{11}\,\Omega$	$10^{11}\,\Omega$	$10^{10}\,\Omega$
U fraction	$^{233}\mathrm{U}$	$^{234}\mathrm{U}$	$^{235}\mathrm{U}$	$^{236}\mathrm{U}$	$^{238}\mathrm{U}$
Rinse					
Th fraction				each $\sim$ 30th cycle	$^{238}\mathrm{U}$*
	$^{229}\mathrm{Th}$	$^{230}\mathrm{Th}$		$^{232}\mathrm{Th}$	

Simplified measurement setup. This setup allows to measure with 0 s decay time and with consistent detector types. An intensity $> 0.8\,\mathrm{mV}$ must be guaranteed. *Used for tailing correction.

Since it is difficult to find samples that naturally contain high [U] and, in particular, high [Th] as SPA-52 does (corals mainly contain only $2\,\text{-}\,4\,\text{ppm}$ ^{238}U), I suggest achieving ε-precision via a detour. On the one hand, this could be achieved through technical improvements that increase the transmission efficiency by an order of magnitude (currently 1 - 2 %) and by decreasing baseline noise by, e.g., cooling the electronics ($U_R \sim \sqrt{T}$) or, on the other hand, by improving the measurement setup. The setup shown in Tab. 4.5 would establish simultaneous measurements for all isotopes in each of their fractions and allow for the decay time to be set to $0\,\text{s}$ as each cup's signal remains from the same isotope. The separated measurement of the U and the Th fraction decreases the tailing impact of isotope ^{238}U on isotope ^{230}Th. Also, a dilution of the sample to only $0.5\,\text{ml}$ (at the moment it is $2\,\text{ml}$) would decrease the measurement time to $5\,\text{min}$ which is $300\,\text{runs}$ of $1\,\text{s}$ and would increase the concentration by a factor 4.

Our instrumental setup is limited to concentrations in the fg/ml-regime (e.g. C09-2). For sample C09-2 the corrections scale with a squared sum of 8 % of age, which is $31\,\text{a} > 25\,\text{a}$ (instrumental error). Thus, our instrumental setup allows to resolve the last $390\,\text{a}$ to $31\,\text{a}$ for samples that contain unusual low [U] and [Th].

5 Reproducibility of U-series ages

Within the scope of this thesis, several samples and standards were measured at different laboratories and on various mass spectrometers (MS) with variable detector setups. Measurements were conducted at the Heidelberg University (UHEI), at the Laboratoire des Sciences du Climat et de l'Environnement (LSCE) in Gif-sur-Yvette, France, and at the University of Minnesota in Minneapolis (UoM), USA. In addition, published data from the Isotope Geology Laboratory at the University of Bern (UoB) by Shakun et al. [2007] are compared with data that were obtained at UHEI and UoM (Sec. 5.2).

The mass spectrometer types range from a Finnigan MAT 262 thermal ionization mass spectrometer (TIMS), via a Thermo Fisher inductively coupled quadrupole mass spectrometer (ICP-QMS or iCapQ) to the formerly introduced Neptune instrument.

The iCapQ has an ICP for ion generation, and a quadrupole magnet that filters for m/z. On the one hand, the iCapQ has the disadvantage of possessing only one SEM detector which prohibits simultaneous measurements. But on the other hand, the iCapQ is less cost intensive, easy to handle and thus less maintenance-intensive. It is fast in scanning large mass ranges and small in size and hence more mobile.

The TIMS is the predecessor of the Neptune. The general setup is similar to the Neptune, only the ion introduction is different. At the TIMS instrument, the sample is thermally evaporated from a filament into the mass spectrometer system. It is noticeable that the TIMS is best in mass bias correction and abundance sensitivity as the TIMS is generally known to be very stable compared to the other two instruments (Tab. 5.1). On the contrary, the TIMS has long measurement times between 2 - 4 h for one U-series age and a lower reproducibility induced by low transmission efficiencies.

The Neptune excels in its high transmission efficiencies (up to 3 %) leading to a high reproducibility (Tab. 5.1).

5.1 Reproducibility of measurements conducted on three different MS

In this section, a sample set of the previously introduced flowstone SPA-52 (see Chap. 4) was dated on a TIMS (UHEI), iCapQ (UHEI), and a Neptune instrument (UHEI and LSCE) in order to evaluate the reproducibility of the UHEI Neptune instrument and measurement protocols (Fig. 5.1). All chemical preparation and data corrections were conducted at UHEI.

It is noteworthy that all ages determined on Neptune instruments are consistent within their 2σ errors (Fig. 5.1). As these measurements were performed at the

Table 5.1: Comparison of the instrument performances of iCapQ, TIMS and Neptune.

	iCapQ	TIMS	Neptune
Mass bias correction (%/amu)	-	$< 0.20^a$	~ 0.34
Transmission efficiency (%)*	0.06 - 0.12	0.05^b	1.50 - 3.00
Abundance sensitivity (ppm)	0.90 - 1.20	0.02 (RPQ)^c	0.30 - 0.80 (RPQ)
U Hydride formation (ppm)	100 - 500	-	10 ± 9
$2\,\sigma$ reproducibility $(^{234}U/^{238}U)/(^{230}Th/^{238}U)$ (‰)	$4.0/10.0^d$	$1.8/2.9^{a,c}$	0.6 - 0.8/0.6 - 1.8

*The transmission efficiency is regarding to isotope ^{238}U. ^{a}Frank et al. [2000], ^{b}ionization efficiency integrated over the term of a measurement (Edwards et al. [1987]), ^{c}Cheng et al. [2000b], ^{d}Douville et al. [2010].

LSCE and UHEI and with different cup configurations (low abundant isotopes of ^{234}U and ^{230}Th on SEM, $10^{11}\,\Omega$ or $10^{13}\,\Omega$ FC) this result is amazingly consistent, also in respect to the gained precisions on age (best $8.4\,\varepsilon$).

This result underlines the credibility of the UHEI corrections and the reproducibility of the instruments and the measurement protocols. It also shows that maximum daily tailing variations of 30 % which affects SPA-52 ages by $14\,\varepsilon$-precision $> 8.4\,\varepsilon$ (Chap. 4) is most likely overestimated.

Another noticeable result is that 80 % of the iCapQ ages overlap with the Neptune ages and 90 % of the TIMS ages overlap with the Neptune and iCapQ ages within their uncertainties (Fig. 5.1).

5.1.1 Reproducibility of measurements performed with $10^{11}\,\Omega$ and $10^{13}\,\Omega$ amplifiers

In this section, a closer look on the reproducibility of the different FC amplifiers, i.e. $10^{11}\,\Omega$ versus $10^{13}\,\Omega$ is obtained. The ages of UHEI-Neptune-FC and UHEI-Neptune-FC13 show ages that were determined with all isotopes measured on FC (Fig. 5.2). The low abundant isotopes of ^{234}U and ^{230}Th were measured either on $10^{11}\,\Omega$ or $10^{13}\,\Omega$ FC, respectively.

All shown ages are reproducible within $2\,\sigma$ uncertainty. The $10^{13}\,\Omega$-ages were measured with mean 11 mV (^{234}U) and 13 mV (^{230}Th; signals normed to a standard $10^{11}\,\Omega$ amplifier) signals while the $10^{11}\,\Omega$-ages were measured with mean 22 mV (^{234}U) and 31 mV (^{230}Th) signals. All errors vary on 8.4 - 11.5 ε-scale, besides two $10^{11}\,\Omega$-ages
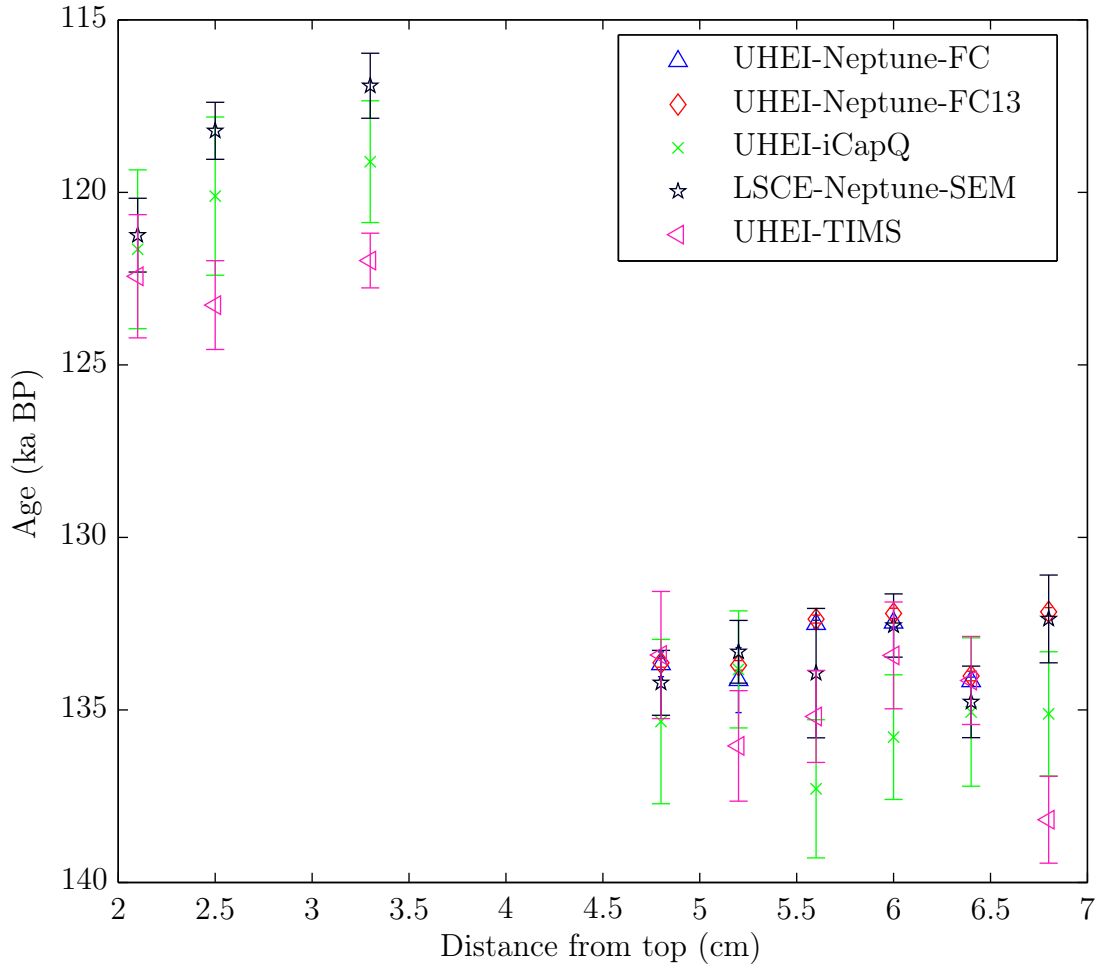
Figure 5.1: Ages determined at UHEI and LSCE with different instruments and with different detector setups versus distance from the top of the flowstone SPA-52. The ages were determined between 2014 and 2016. All ages determined at Neptune instruments are within $2\,\sigma$ errors. Some of the ages determined at UHEI were measured on ε-scale. UHEI-Neptune-FC: all isotopes are measured on $10^{11}\,\Omega$ FC. UHEI-Neptune-FC13: low abundant isotopes of ^{234}U and ^{230}Th are measured on $10^{13}\,\Omega$ FC. LSCE-Neptune-SEM: low abundant isotopes of ^{234}U and ^{230}Th are measured on SEM.

that were measured on 2.7 - 7.0 ‰-scale. These results show that high precision U-series dating with $10^{13}\,\Omega$ amplifiers is feasible, reproducible and that less intense signals are sufficient. Furthermore, regarding only the ages that were measured with the highest precision (Fig. 5.2) the duration of the growth interruption (Hiatus) of the flowstone SPA-52 can be determined to $133.187 \pm 0.833\,\text{ka BP}$. The meaning of this newly obtained date is further discussed in the following section.
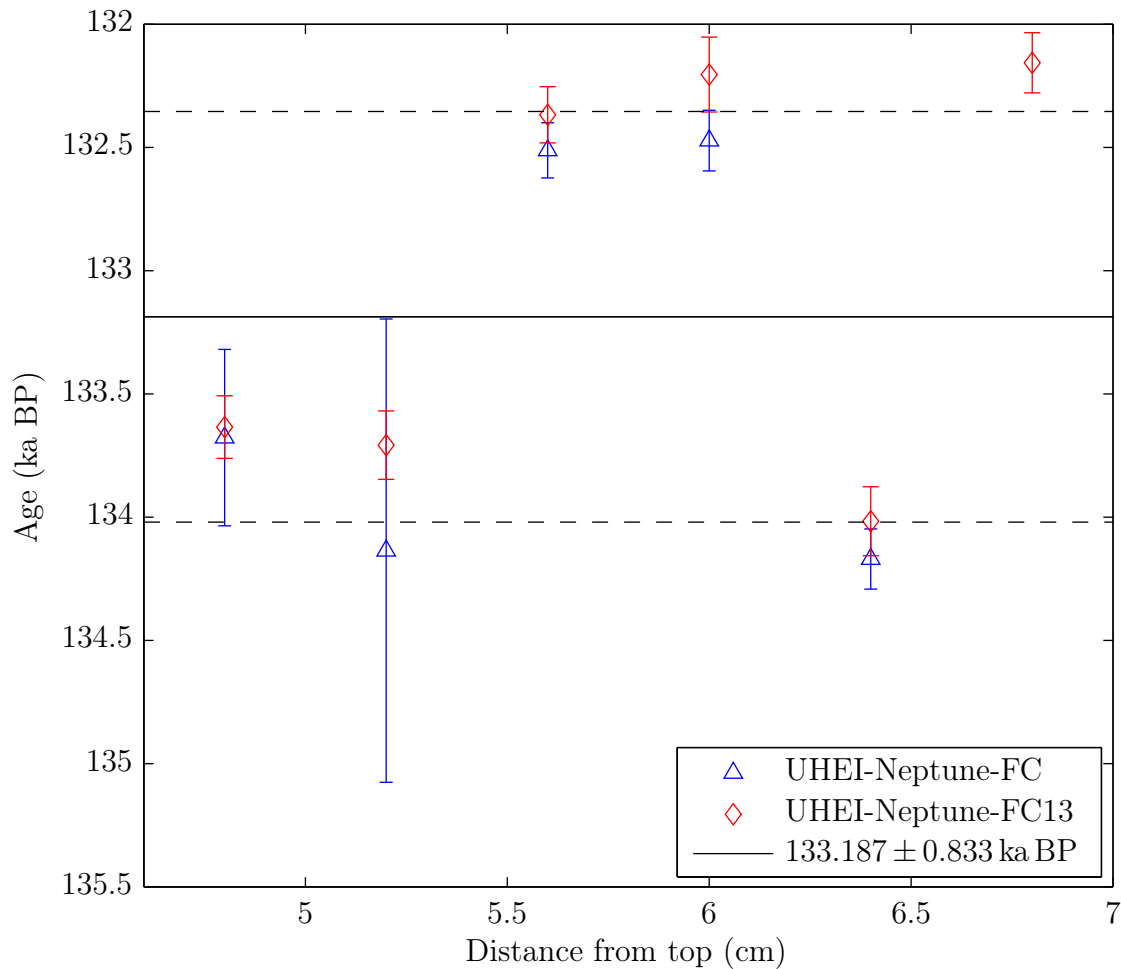

Figure 5.2: Ages determined at UHEI with different detector setups versus distance from the top of flowstone SPA-52. The black lines correspond to the average age of $133.187 \pm 0.833\,\text{ka BP}$, i.e. the duration of the Hiatus of the flowstone SPA-52.

5.1.2 Short climate story: mystery 135 ka-event

Changes to Earth's orbital parameter configuration relative to the Sun, known as Milankovitch hypothesis or orbital forcing, have been considered as the leading theory for the mechanism driving glacial-interglacial cycles and associated climate change (Emiliani [1955]; Hays et al. [1976]; Imbrie [1985]). This hypothesis is supported by a number of paleoclimate records across the globe proving that climate shifts took place on orbital time scales simultaneous with changes in the orbital parameters of the Earth's orbit around the Sun (Hays et al. [1976]; Cheng et al. [2009]; Lisiecki and Raymo [2005]).

Of note is the controversy about the timing of events at the end of the penultimate glacial period/Marine Isotope Stage 6 called Termination II (TII). At issue is whether TII preceded the rise in boreal insolation in which case TII could not result directly from orbital forcing. In this connection, the data of SPA-52 of UHEI-TIMS in Fig. 5.1 were published by Spötl et al. [2002]. They claim that the deposition of the flowstone, and hence the beginning of the warming in the Northern Alps started at 135.0 ± 1.2 ka BP which is before the rise in boreal summer insolation (black dashed box in Fig. 5.3b).

In this thesis and with the help of precise and reproducible measurements the start of the warming in the Northern Alps at Spannagel Cave can be determined to 133.187 ± 0.833 ka BP (considering only high resolution UHEI-Neptune-FC and UHEI-Neptune-FC13 ages in Fig. 5.2 and in Sec. 5.1.1).

Although this newly determined date of the beginning of the warming was only shifted by ~ 2 ka, the beginning of flowstone deposition now corresponds with the turning point towards maximum solar irradiance of the June $60\,^\circ$N latitude insolation curve as well as with other climate proxies, such the δD Antarctica curve (black solid box in Fig. 5.3a and b). Hence, it seems that warming took place possibly concordant to the rise in boreal summer insolation which is in contrast to the former dating results of Spötl et al. [2002] (black dashed box in Fig. 5.3b).

The newly obtained age also matches with the start of the carbonate deposition of two other stalagmites which are in close proximity to SPA-52 (SCH-5 from Schneckenloch Cave which started depositing at 134.1 ± 1.7 (Fig 5.3d) and HÖL-10 Hölloch Cave which started depositing at 131.8 ± 1.2 ka; Moseley et al. [2015]; both from Austrian Northern Alps) and with the midpoint to the shift to interglacial values at 132.2 ± 1.4 ka of the famous sub-aqueous calcite record DH_2-D from Devils Hole, Nevada, USA (Moseley et al. [2016]; Fig. 5.3c).
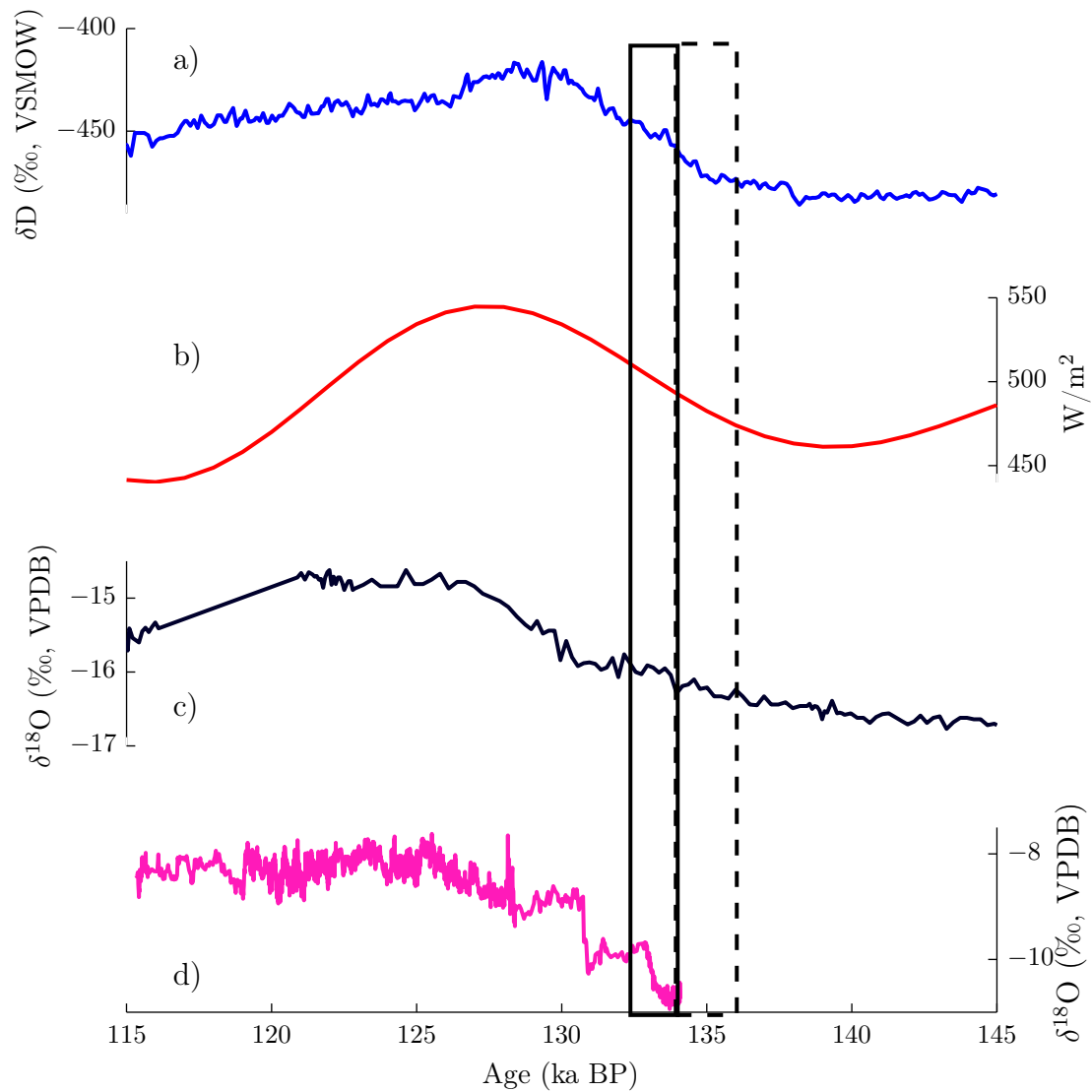
Figure 5.3: Flowstone growth in comparison to Pleistocene climate records. From top to bottom: a) δD of ice at Vostok, proxy of air temperature at Antarctica (ice flow modeling; Petit et al. [1999]). b) June insolation of 60° N latitude. c) δ^{18}O calcite record DH$_2$-D from Devils Hole, Nevada, USA (Moseley et al. [2016]). d) δ^{18}O from stalagmite SCH-5 from Schneckenloch Cave, Austria (Moseley et al. [2015]). Black dashed box: Previously obtained temporal resolution of 135.0 ± 1.2 ka BP from Spötl et al. [2002]; black solid box: improved temporal resolution of 133.2 ± 0.8 ka BP.

5.2 Instrument performances between different laboratories

The Neptune instrument installed in UHEI and the chemical protocol are compared with the Neptune instruments installed at LSCE and UoM and their chemical protocols (Tab. 5.2). The results are convincing that mass bias correction, chemistry blank, transmission efficiency, and abundance sensitivity perform on comparable levels for all three laboratories.

Here, I would like to stress that stalagmite MI5 from Socotra island, Yemen, which was originally dated in the Isotope Geology Laboratory at UoB in 2007 by Shakun et al. [2007] fits with the age model of dates that were determined in the UoM laboratory in 2016 and another 25 dates that were obtained from the UHEI laboratory in the same year. The ages determined at UoM used a different chemical preparation procedure which is further discussed in Chap. 6. The growth is continuous and no age inversions within 3σ uncertainties are given which highlights again the reproducibility of the UHEI chemical preparation procedure, instrument performance, data corrections and measurement routines. The UHEI ages were determined in two different ways, i.e. the U and Th fractions were measured separately or combined, which will be further discussed in Sec. 5.3.

Table 5.2: Comparison of the Neptune instrument and chemical protocol performances at three different laboratories (UHEI, UoM, LSCE).

	UHEI	UoM	LSCE
Mass bias correction (%/amu)	$^{235}U/^{238}U$* ~ 0.34	$^{233}U/^{236}U$* ~ 0.34	$^{235}U/^{238}U$* ~ 0.34
Transmission efficiency (%)**	1.5 - 3	0.5 - 1.9	1.5
Abundance sensitivity RPQ (ppm)	0.3 - 0.8	0.4 - 0.7	0.5
Chemistry blank			
^{230}Th	40 ag	< 100 ag	-
^{232}Th	4 pg	< 1 pg	-
^{234}U	400 ag	< 100 ag	-
^{238}U	5 pg	< 1 pg	-

The mass bias correction, the transmission efficiency, and the abundance sensitivity were determined by data I obtained while working in the three laboratories. The UHEI chemistry blank is an average value of 22 months working operation since installation, whereas the UoM values are recommended best case chemistry blank values and do not represent a mean value. *Determined with this isotopic ratio. **The transmission efficiency is with respect to isotope ^{238}U.
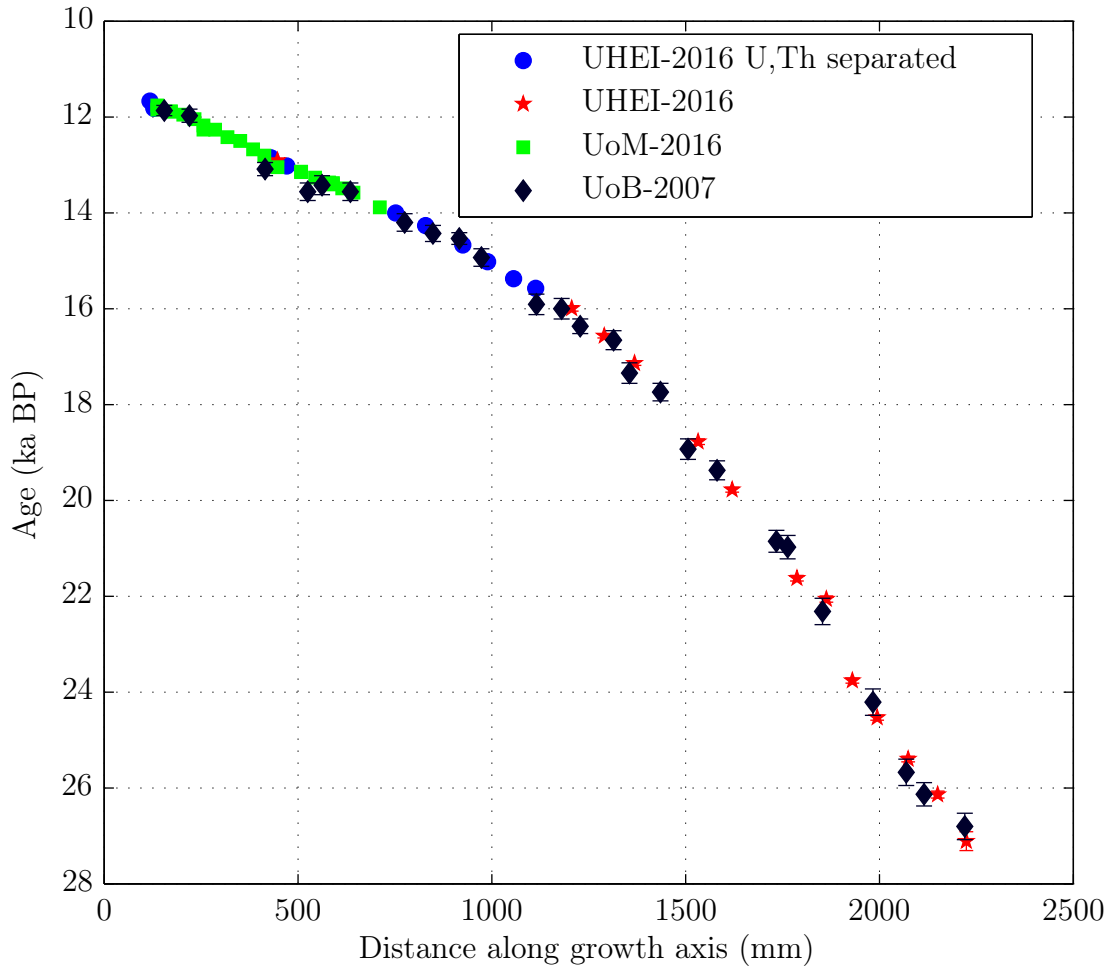
Figure 5.4: Ages determined in UHEI, UoM, and UoB versus distance along growth axis. The growth is continuous and no age inversions within $3\,\sigma$ uncertainties are given demonstrating that all three laboratories' chemical preparation, instrument performances, and data corrections do not affect ages significantly in a time frame of $27\,\text{ka}$.

5.3 Measurements of separated U and Th fractions

In this section, the advantages and disadvantages by measuring the U and the Th fraction separately are investigated. The measurement protocol for separated U and Th fractions is shown in Tab. 5.3. Here, the isotope ^{238}U is measured every ~ 30th cycle of the Th fraction in order to correct for tailing.

The advantages for separate measurements are the following: (1) there is less impact of U tailing correction on the low abundant isotope ^{230}Th which is especially important for samples with low [Th], because only a few per mil of the U fraction remains in the Th fraction (Wefing [2016]) and (2) an improved statistic is gained due to an increase of measurement cycles for each fraction as it is not necessary to jump between U and Th (see Tab. 5.3).

69

Table 5.3: Dating routine and collector configuration for U-series measurements.

Faraday cups amplifier	L1 $10^{11}\,\Omega$	Center $10^{13}\,\Omega$/(SEM)	H1 $10^{11}\,\Omega$	H2 $10^{11}\,\Omega$	H3 $10^{10}\,\Omega$
Standard	^{233}U ^{229}Th	^{234}U $(^{230}$Th) $(^{229}$Th)	^{235}U ^{230}Th	^{236}U ^{232}Th	^{238}U
U fraction Th fraction	^{233}U ^{229}Th	^{234}U $(^{230}$Th) $(^{229}$Th)	^{235}U ^{230}Th	^{236}U each $\sim$ 30th cycle ^{232}Th	^{238}U ^{238}U
Standard	...	...	...	...	...

Measurement protocol for a separated U and Th fraction. No switch in the magnet of the Neptune is needed in the U fraction.

On the contrary, there are the following disadvantages: (1) only a mean of the U fractions' ^{235}U/^{238}U ratio is used for Th isotopes mass bias correction, in contrast to the conventional protocol illustrated in Sec. 3.1.1 in which each cycle is simultaneously corrected to the respective ratio. (2) U and Th fraction measurements between two standards (standard bracketing corrects the activity ratios (^{234}U/^{238}U) and (^{230}Th/^{238}U)) take a greater deal of time of about 15 - 20 min and hence increases the impact of the machine drift on activity ratios. (3) The consumption of acids for the rinse is higher and the total measurement time is prolonged in the end.

In order to estimate the influence/offset of the particular age when measuring U and Th separately compared to the conventional measurement protocol, two sample batches A (Tab. 3.1, combined fractions) and B (Tab. 5.3, separated fractions) from the same sample material/powder of corals from core GeoB20933-1 were generated (Wefing2016). The ages obtained with both measurement ways are plotted versus each other (see Fig. 5.5). The ages follow a linear fit with slope $a = 0.99904$, offset $b = $ -0.01164 and with a fit norm of residuals of 0.078. The errors in age range on an average 3 ‰-scale which is the same 3 ‰-scale of the ages' offset to each other. The offset of the activity ratios (^{234}U/^{238}U) and (^{230}Th/^{238}U) to each other range on 1.6 ‰-scale.

These variations are within dating precision but do not vary on ε-scale. However, the samples were measured on two different days within a two months time frame and the sample's chemical preparation is different: batch A was prepared manually, and batch B was prepared automatically via a prepfast module (see Wefing [2016]). Hence, no significant effect of altered corrections on ages is observed within the time frame of 35 ka. The reproducibility of the obtained data is on 1.6 ‰-scale for the
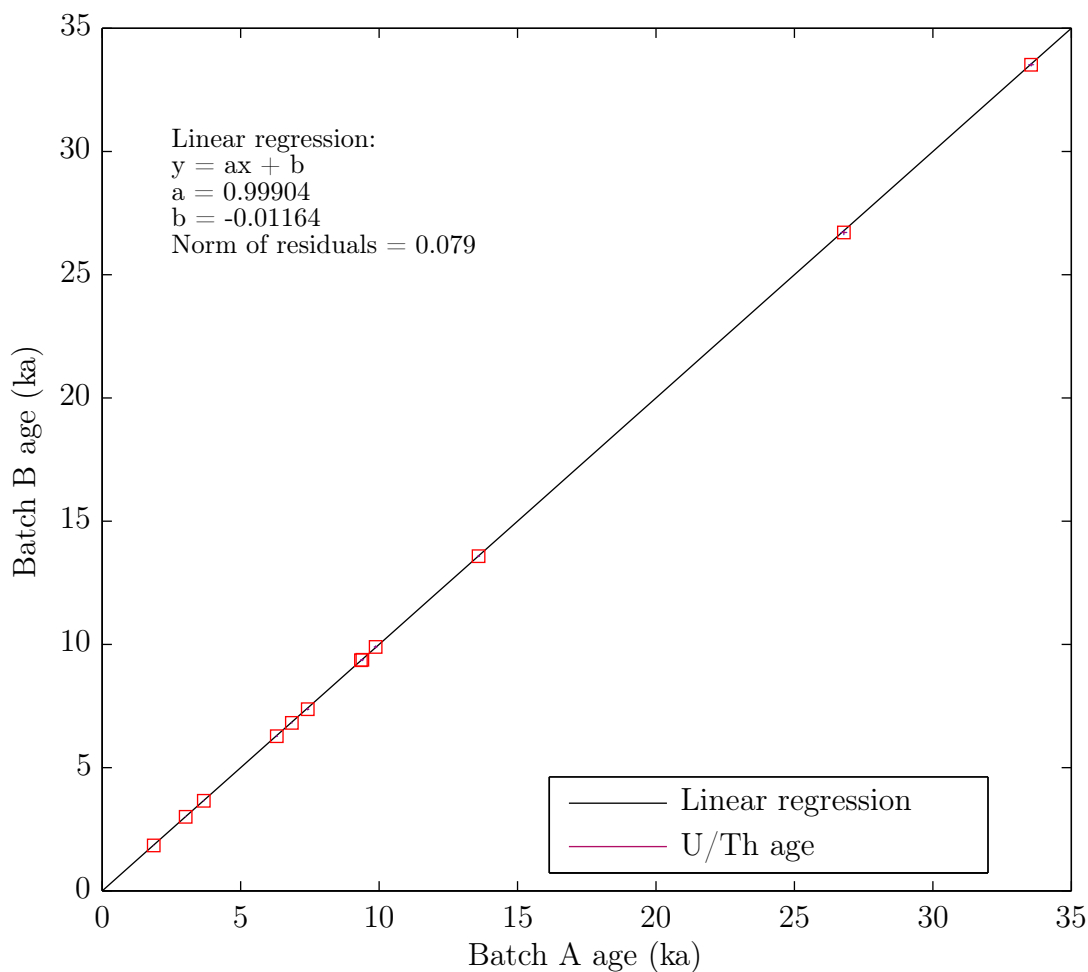
Figure 5.5: Ages of GeoB20933-1 of a batch of samples that were measured with separated U and Th fractions (batch B) versus a batch of samples that were measured via the conventional protocol (batch A). A norm of residuals, which is close to zero indicates a good fit with a slope of $a = 0.99904 \approx 1$.

UHEI Neptune instrument, chemical preparation procedure and dating technique. At this point I would like to mention once again that the separation of the fractions promises an advantage, especially for samples with low [Th], i.e. young ages, which since counting statistic limitations can not be measured with ε-precision. For samples with low [Th], a reduced ^{238}U tailing correction on isotope ^{230}Th and a prolonged measurement time of the Th fraction or a more concentrated Th fraction solution is beneficial.

If the U and Th fractions are measured separately, the improved statistic due to prolonged cycling during measurements increases the instrumental precision. Here, in this case, the errors are 13 % smaller than the errors obtained by the conventional way.

5.4 Discussion of the reproducibility

This chapter examines qualitatively the reproducibility of the UHEI laboratory regarding instrument performances, measurement protocols, data analysis corrections, and chemical preparation. It turns out that the UHEI instrument, when compared to other Neptune instruments (LSCE and UoM), performs similarly (see Tab. 5.2).

In addition, the ages of different samples were reproduced on different mass spectrometers, with different detector setups and in different laboratories (LSCE, UoM and UoB). Also samples, which were prepared chemically differently (batch A and batch B in Sec. 5.3) and which were measured either with separated or combined U and Th fractions, show activity ratios that are reproducible on 1.6 ‰-scale. Measuring the U and Th fraction separately is beneficial for samples with low [Th] as measurement statistics can be improved (here by 13 %), and the ^{238}U tailing correction impact is reduced on isotope ^{230}Th.

A stunning result is that the ages of flowstone SPA-52 were reproduced on 8.4-11.5 ε-scale with different cup configurations on two different measurement days that are twelve months apart, highlighting the stability of the UHEI Neptune performances. These results show that high precision U-series dating with $10^{13}\,\Omega$ amplifiers is feasible, reproducible and that less intense signals are sufficient. This result underlines the credibility of our corrections and the reproducibility of our chemistry, the instruments, and the measurement protocols. It also shows that maximum daily tailing variations of 30 % that affects SPA-52 ages by 14 ε-precision $> 8.4\,\varepsilon$ (Chap. 4) is most likely overestimated.

With these newly determined ages (Sec. 5.1.2) a better estimate of the beginning of the warming in the Northern Alps in Austria (at Spannagel Cave) can be obtained. The newly dated begin of warming for TII is now 133.187 ± 0.833 ka BP. This date matches with the start of deposition of stalagmites in close proximity and with the midpoint to the shift to interglacial values at 132.2 ± 1.4 ka of the famous sub-aqueous calcite record DH$_2$-D from Devils Hole, Nevada, USA. It shows, that the growth of the flowstone and hence initial warming at that region started at the turning point of the rise in boreal summer insolation which seems more consistent with the Milankovitoch hypothesis than formerly published results.

6 Application study: The centennial growth rate variability of two alpine Holocene speleothems

The possible influence of climate on speleothem growth phases and rates has frequently been emphasized (also see Sec. 5.1.2). Yet, the processes leading to speleothem growth rate variations are complex and are not necessarily influenced by climate only. Hence, in this study growth rates (GR) with a centennial-scale resolution of two stalagmites from adjacent caves in the northwestern Alps, Betten and Schratten Cave, were determined using high-precision U-series dating. Both stalagmites were dated witch a temporal resolution of $\sim 220\,a$ between 6,550 and 200 a BP. This study is unique as two sets of ages for the same time interval and catchment area were compared with such a high resolution.

6.1 Motivation of the application study

Speleothems' important feature is their capturing of the cave's response to its external environment, e.g. the cave temperature – apart from a few exceptions – reflects the mean annual surface air temperature and the drip water discharge often responds strongly to the degree of infiltration. Various models and empirical works have shown that speleothem growth is dependent on soil activity, temperature, precipitation, and cave air CO_2 concentration (Baker et al. [1993], Baker et al. [1998], Baker et al. [2016]; Dreybrodt [1999]; Kaufmann and Dreybrodt [2004]; Mühlinghaus et al. [2007]; Romanov et al. [2008]; Fairchild et al. [2012]). A stalagmite stratigraphy can reflect fluctuation of paleoclimate on various time scales, from annual (Mattey et al. [2008]; Baker et al. [2014]) and millennial (Hoffmann et al. [2016]), to ice age cycles (Richards et al. [1994]; Spötl et al. [2002]; Boch et al. [2011]). Speleothems' function as a paleoclimate archive has been exploited in numerous studies with regard to aspects including glacial terminations, Dansgaard-Oeschger events, monsoon patterns, and solar activity (e.g. Frisia et al. [2003]; Cheng et al. [2006]; Moseley et al. [2016]; Wassenburg et al. [2016]).

However, the suitability of speleothem growth rates (GR) as climate proxies is controversial because calcite precipitation is complex; the GR can be further influenced by chaotic processes for example by changing flow paths in the karst system or a change of ventilation in the cave. Considering the fact that speleothem growth is itself most likely dependent on climate (Baker et al. [1993]; Burns et al. [1998], Burns et al. [2001]; Spötl et al. [2004]; Spötl and Mangini [2006]; Jo et al.

[2014]), one may obtain evidence of the paleoclimate in the catchment of the cave when considering average GR variations or growth phases of either an individual stalagmite or a set of stalagmites (Stoll et al. [2013]; Wong and Breecker [2015]; Hoffmann et al. [2016]). This would imply that growth records could have regional climate significance beyond their apparent chaotic nature. There are few high resolution growth records to test whether such influences – either climatic or chaotic – may appear on time scales of centuries. Hence, it is explored whether centennial-scale GR patterns could be a robust and reproducible climate proxy.

This test is conducted on two stalagmites collected in adjacent caves. These caves are 950 m apart and therefore share the same catchment area. Both stalagmites grew over 6,550 a throughout the mid-Holocene climate transition and thus likely share some common (but unknown) climate variability. The Holocene is of particular interest as it is a period of noticeable changes in solar insolation, global ice volume, and regional temperature (Davis et al. [2003]). The difference in altitude in alpine regions implies possible changes of water availability, mean temperature, and soil activity (vegetation) even on small distances (Nussbaumer et al. [2011]). The large temporal variations of the GR turn out to be individual for both speleothems as expected given the complex nature of carbonate deposition; hence, these two stalagmites do not measure coherent growth rate pattern on centennial time scales.

In the following, it is demonstrated that the two stalagmites, while not giving a coherent regional growth pattern, do still expose a weak link between climate and GR on millennial-scale. It is suggested to infer a link to local soil activity and vegetation intervened with fluctuations of the glacier extend in the particular studied alpine region that exerts an influence on the stalagmite deposition.

6.2 Study site

The two examined stalagmites originate from adjacent caves in the central Alps of Switzerland, Betten Cave and Schratten Cave. These caves were discovered by the Höhlenforscher-Gemeinschaft Unterwalden (HGU) and are both part of the alpine karst in the Melchtal valley south of Melchsee-Frutt, located in the canton Obwalden (Fig. 6.1). Among the 58 km of surveyed cave passages in this karst province, which drains into the Melchtal valley, Betten Cave (29 km) and Schratten Cave (20 km) are the longest caves.

The European Alps receive the majority of their annual moisture from the North Atlantic Ocean, the Mediterranean Sea and from land evaporation (Sodemann and Zubler [2010]). With a mean annual temperature of $6.4 \pm 0.7\,°C$ and a precipitation of $1,550 \pm 170$ mm, the study site can be characterized as temperate and humid (1980-2016; station Engelberg at 1,036 m a.s.l., ~ 10 km away). Both caves are located on the same hillside but the stalagmite's drip water samples from different local karst levels due to the 418 m altitude difference between both sites.
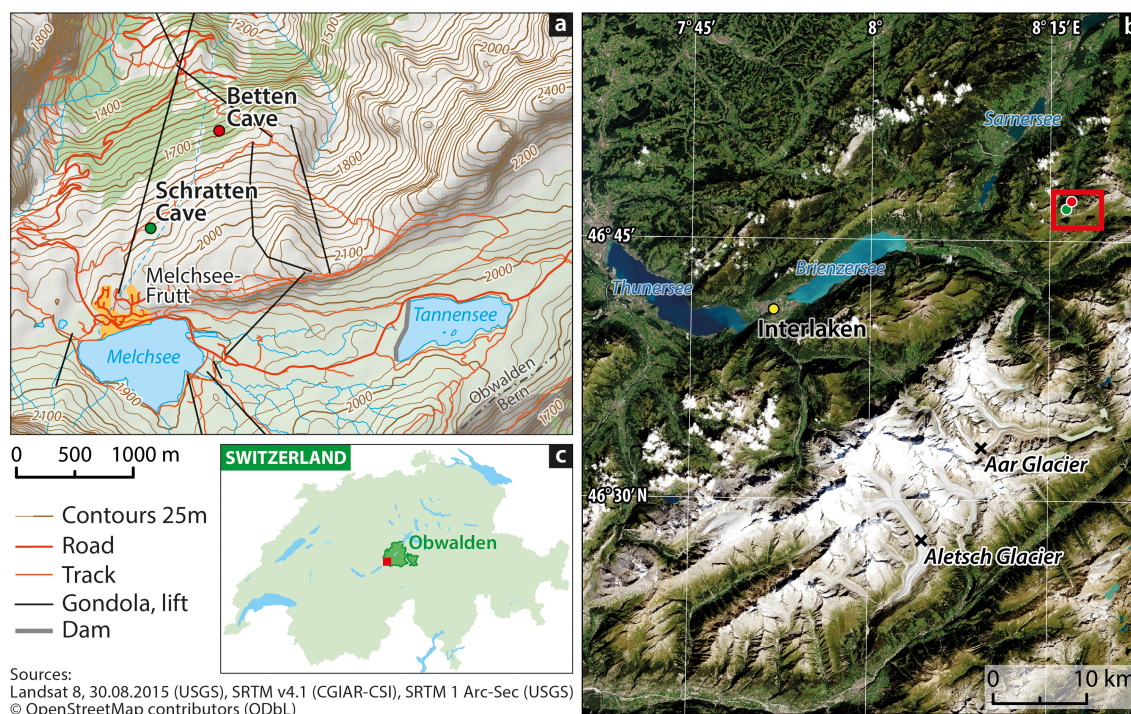
Figure 6.1: Contour map showing the location of the sampled speleothems in central Switzerland. M39_764/1 (Betten Cave) was located clearly below the present day tree-line in contrast to the M6_1/20 (Schratten Cave). Two residual glacier lakes (Tannensee and Melchsee) are south of the karst catchment of Melchsee-Frutt. b) Location of Betten (red) and Schratten Caves (green). The linear distance between the sites is about 1 km. The caves are located in the northern part of the Alps in vicinity of the Aar Glacier. c) Location of the study site in Switzerland (maps designed by V. Schniepp and U. Selgert, s. References for map data details).

6.3 Stalagmites

A 57 cm-long stalagmite, M39_764/1 (M39 for short, Fig. 6.2), was collected 5 m above the permanently flowing cave's creek in the passage Schöllenen-Biwakaufstieg (Biwak VII), has a diameter of 10 cm and consists of white aragonite alternating with dark (translucent) calcite. While M39 formed at a lower karst level in Betten Cave (N 46° 47.309 E 8° 16.819, 1,364 m a.s.l.) (NeKO and Trüssel [2014]).

Stalagmite M6_1/20 (M6 for short, Fig. 6.2) grew at a 418 m higher elevation in Schratten Cave (N 46° 46.856 E 8° 16.363, 1,782 m a.s.l.) with a horizontal distance of 950 m. The M6 completely consists of calcite and formed directly on host rock, is 19 cm in length, and 6 to 10 cm wide (NeKO and Trüssel [2014]). The location of M6 in the Schratten Cave is overlain by an 85 m of Upper Jurassic Quinten limestone. In contrast, M39 in Betten Cave formed in a passage with 295 m of rock

overburden (Middle and Upper Jurassic formations, including Quinten limestone, Schilt formation and a layer which is in varying degrees impermeable to water (Erzegg formation, maybe also Hochstollen formation). Both stalagmites grew simultaneously and continuously during the mid to late Holocene (6,550 to at least 200 a BP, compare Sec. 6.5). Both sites are actively dripping, hence, the tops of the stalagmites are presumed to be modern.

X-ray diffraction images were taken of two supposed to be calcite (brown layers at 7.5 and 21 cm) and two aragonite samples (white layers at 17.5 and 37.2 cm) of stalagmite M39. The brown samples' spectra match with a typical calcite spectrum, while the white samples show the typical aragonite spectrum, but seem to have an additional calcite fraction.
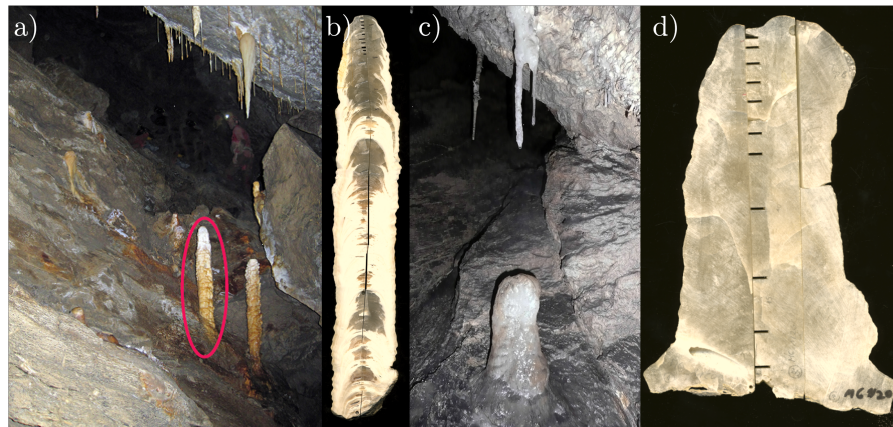
Figure 6.2: Images a) and b): Stalagmite M39_764/1. The stalagmite is c. 57 cm in length, showing alternating layers of calcite and aragonite (proven with x-ray diffraction) and started to grow at $\sim 11,300$ a BP. Images c) and d): Stalagmite M6_1/20. The stalagmite is c. 20 cm in length, showing a homogeneous compact fabric and started to form $\sim 6,550$ a BP (image a) and c): NeKO and Trüssel [2014]).

6.4 Analytical methods

M39 and M6 were analyzed in detail for their [U] and [Th] and respective isotopic composition. Sub-samples of 0.2 - 0.3 g were hand-drilled or cut along growth layers for U/Th analysis (M39, n = 57; M6, n= 34). Isotopic measurements were conducted using MC-ICP-MS (Thermo Fisher Neptune/Finnigan Neptune, n = 91) and an ICP-QMS (Thermo Fisher iCapQ, n= 24) at UHEI, LSCE and UoM according to the analytical protocols of Chap. 3 (UHEI/LSCE), and Cheng et al. [2013], Shen et al. [2012] (UoM).

Chemical preparation followed sample dissolution, spiking with ^{229}Th, ^{233}U, and ^{236}U and subsequent purification of U and Th using wet-column chemistry with Eichrom UTEVA (UHEI/LSCE) or Dowex 1x8 (UoM) resin. The chemical separation

protocol for UHEI and the LSCE followed the procedure of Chap. 3, while the chemical separation protocol for Minnesota followed the procedure of Cheng et al. [2013], and Shen et al. [2012]. Age-depth models are developed with StalAge (Scholz and Hoffmann [2011]).

6.5 Results

Stalagmite M39 consists of calcite and aragonite layers. The former appear brown while the aragonite sections are white on the cut slab. M6 is composed of calcite only. The calcite of M6 and M39 yielded ^{238}U concentrations of 340 - 580 ppb and 200 - 550 ppb, respectively, while the aragonite of M39 yielded ^{238}U concentrations of 1,700 - 2,600 ppb (Tab. 6.1 and 6.2). The measured $(^{230}\text{Th}/^{232}\text{Th})_{\text{atomic}}$ for M6 and M39 ranges from 450 - 48,800 $\cdot$ 10^{-6}, and from 106 - 160,100 $\cdot$ 10^{-6}, respectively, while the lowest values are for ages younger than 500 a BP (Tab. 6.1 and 6.2). These values reflect a minor presence of detrital Th in both speleothems and consequently corrections due to detrital Th are negligible. Nevertheless, ages were corrected by using an initial $^{230}\text{Th}/^{232}\text{Th}$ based on the bulk earth $(^{230}\text{Th}/^{232}\text{Th})_{\text{atomic}}$ of $4.4 \pm 2.2 \cdot 10^{-6}$ (Wedepohl [1995]).

U-series ages yield a precision of 2.6 - 5.1 ‰ (53 % of all measured ages), and 6.2 - 91.9 ‰ (45 %). Two percent of the most recent ages (< 100 a) have higher uncertainties ranging between 126 - 238 ‰. All ages are in stratigraphic order within 3σ uncertainty and are consistent between different methods and chemical preparation protocols, as the measurements were performed in three different laboratories (Tab. 6.1 and 6.2). M6 grew continuously over the period $6{,}531 \pm 88$ to 226 ± 3 a BP, whilst the carbonate of M39 precipitated between $11{,}317 \pm 178$ to 83 ± 20 a BP (Tab. 6.1 and 6.2, Fig. 6.3).

The GR of both stalagmites were determined via StalAge interpolating between ages (Scholz and Hoffmann [2011]) (StalAge age-depth model in Fig. 2). The two stalagmites were sampled at an average distance of $\Delta x_{\text{growthaxis}} = 7$ mm (M6) and $\Delta x_{\text{growthaxis}} = 13$ mm (M39), which corresponds to a ~ 220 a temporal resolution for the GR tie points. Hence, the GR in Fig. 6.8 was determined by an average $\Delta t \sim 220$ a, which corresponds to the same mean distances along the growth axes of $\Delta x = 7$ mm (M6) and $\Delta x = 13$ mm (M39). M6 exhibits a deposition rate between 19 ± 5 and 67 ± 23 µm a^{-1}, while M39 has a higher GR, which varies between 37 ± 1 and 110 ± 14 µm a-1 (Fig. 6.8). The GR of both stalagmites are highly variable and do not correlate significantly ($r = 0.37$, $p = 0.25$).

In the M39 record, the aragonite layers coincide mostly with intervals of lower average GR by up to 50 %, which is further discussed in Sec. 6.5.1 and Fig. 6.4. A discussion of the appropriateness of the StalAge age-depth model is provided in Sec. 6.5.2 and with Fig. 6.5, presenting a comparison with a GR pattern provided via discrete U-series ages.

In Sec. 6.5.3 and Fig. 6.6 and Fig. 6.7 it is argued that the correlation between the two GR patterns does not significantly increase when adjusting the offset of one GR
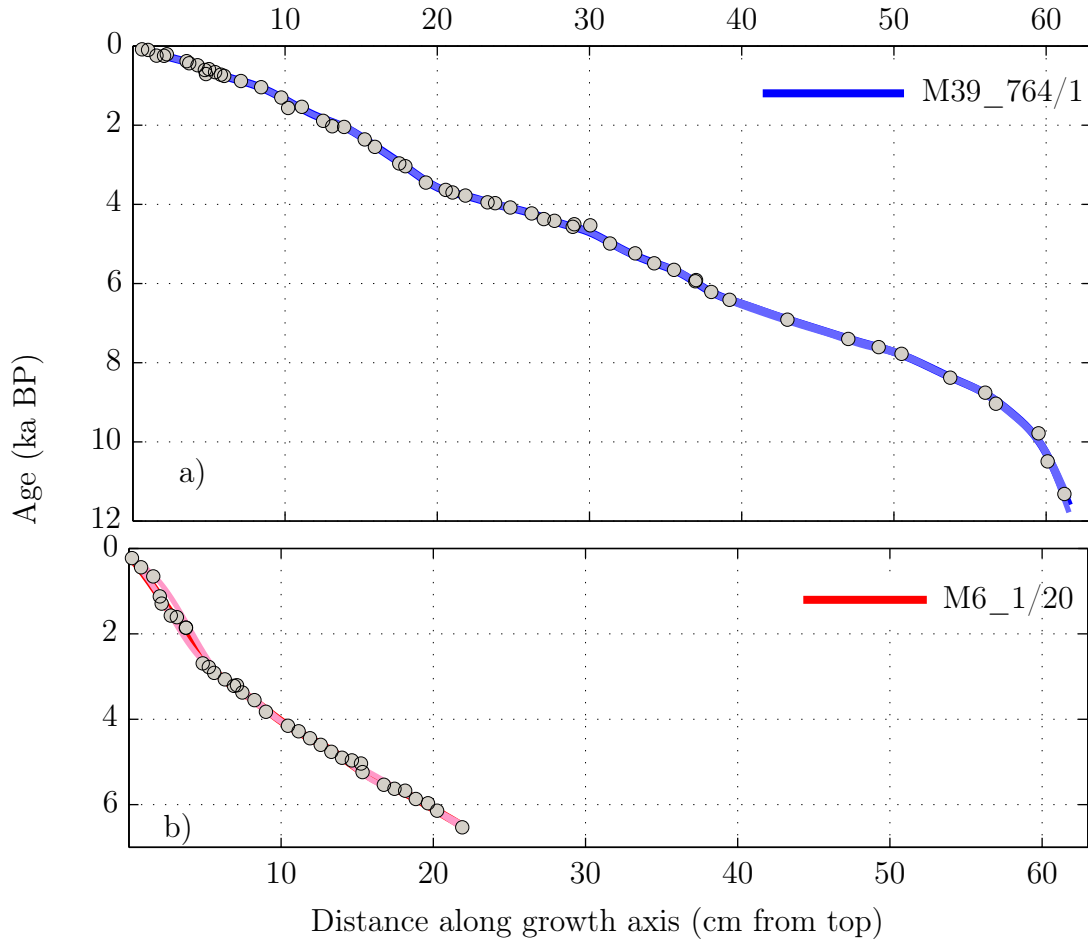
Figure 6.3: StalAge Scholz and Hoffmann [2011] based age-depths models including $2\,\sigma$ error envelopes for the two speleothems presented in this study. (a) M39_764/1; (b) M6_1/20. Error bars are mostly overlapped by the symbols of the U-series data points.

pattern, smoothing the two GR pattern, or using a time frame of 6,550 to 2,400 a BP only. The $\delta^{234}U_{initial}$ is a measure of the fractional deviation of the $(^{234}U/^{238}U)$ atom ratio from the value at secular equilibrium during calcite formation. The absolute values and the amplitude of change of the respective $\delta^{234}U_{initial}$ values differ strongly for the two stalagmites (Fig. 6.8). M6 reveals a range of $\delta^{234}U_{initial}$ of 107 ‰ from $2{,}011 \pm 3$ to $2{,}118 \pm 3$ ‰ independent on age. In contrast, M39 reveals twice as high $\delta^{234}U_{initial}$ values spanning 516 ‰ from $4{,}199 \pm 11$ to $4{,}715 \pm 4$ ‰, which moreover show a clear trend across the past $\sim 11{,}300$ a (Tab. 6.1 and 6.2, Fig. 6.8).

Table 6.1: U-series dating results of M6_1/20.

Sample ID	Depth (mm dft)	$[^{238}U]$ (ppb)	$[^{232}Th]$ (ppt)	$^{230}Th/^{232}Th$ (atomic $\cdot 10^{-6}$)	$(^{230}Th/^{238}U)^a$ (activity)	^{230}Th Age^b (a) (uncorrected)	$\delta^{234}U_{initial}^c$ (corrected)	^{230}Th Age^{d,e} (a BP) (corrected)
M6_1/20								
UHEI-7137	2.0	383 ± 1	33 ± 1	1540 ± 16	0.0081 ± 0.0001	291 ± 2	2052 ± 3	226 ± 3
UHEI-6336*	8.0	375 ± 1	201 ± 1	448 ± 32	0.0142 ± 0.0010	510 ± 35	2078 ± 6	441 ± 35
UHEI-7136	16.0	342 ± 1	79 ± 1	1448 ± 11	0.0202 ± 0.0001	722 ± 5	2065 ± 2	655 ± 5
UoM-7264	20.3	386 ± 1	177 ± 4	2355 ± 49	0.0330 ± 0.0001	1190 ± 5	2047 ± 4	1122 ± 5
UoM-7265	21.5	371 ± 1	69 ± 1	3330 ± 68	0.0377 ± 0.0001	1359 ± 4	2047 ± 3	1292 ± 4
UoM-7266	27.5	391 ± 1	49 ± 1	6042 ± 124	0.0455 ± 0.0001	1639 ± 5	2056 ± 3	1573 ± 5
LSCE-6891	31.5	390 ± 1	50 ± 1	3380 ± 44	0.0472 ± 0.0005	1673 ± 19	2107 ± 3	1609 ± 19
UoM-7267a	37.5	454 ± 1	83 ± 2	4910 ± 101	0.0539 ± 0.0003	1921 ± 8	2086 ± 3	1857 ± 8
UoM-7267b	37.5	454 ± 1	81 ± 2	4977 ± 103	0.0537 ± 0.0003	1918 ± 9	2085 ± 4	1855 ± 9
UoM-7269	48.5	578 ± 1	75 ± 2	9750 ± 198	0.0769 ± 0.0002	2757 ± 9	2088 ± 3	2691 ± 9
LSCE-6892	52.5	410 ± 1	46 ± 1	1215 ± 14	0.0798 ± 0.0008	2841 ± 28	2118 ± 3	2777 ± 28
UoM-7270	56.0	396 ± 1	43 ± 1	12548 ± 256	0.0832 ± 0.0002	2980 ± 9	2094 ± 3	2914 ± 9
UoM-7271	63.0	404 ± 1	48 ± 1	11954 ± 243	0.0869 ± 0.0003	3225 ± 10	2077 ± 3	3066 ± 10
UoM-7272	69.0	432 ± 1	46 ± 1	13853 ± 272	0.0901 ± 0.0003	3347 ± 10	2055 ± 3	3217 ± 10
LSCE-6893	71.0	422 ± 1	40 ± 1	1626 ± 18	0.0908 ± 0.0007	3268 ± 26	2089 ± 3	3204 ± 27
UoM-7273	74.5	420 ± 1	37 ± 1	17531 ± 363	0.0942 ± 0.0003	3440 ± 10	2043 ± 3	3374 ± 10
UoM-7274	82.5	417 ± 1	32 ± 1	21731 ± 451	0.0997 ± 0.0003	3617 ± 11	2067 ± 3	3552 ± 11
UoM-7275	90.0	441 ± 1	31 ± 1	24883 ± 519	0.1057 ± 0.0003	3891 ± 13	2026 ± 4	3825 ± 13
UoM-7277	104.5	410 ± 1	45 ± 1	17486 ± 361	0.1157 ± 0.0004	4218 ± 14	2061 ± 3	4152 ± 14
UoM-7278	111.5	416 ± 1	34 ± 1	23941 ± 497	0.1193 ± 0.0003	4346 ± 13	2066 ± 3	4281 ± 13
UoM-7279	119.0	399 ± 1	18 ± 1	45568 ± 989	0.1238 ± 0.0004	4511 ± 16	2068 ± 3	4445 ± 16
UoM-7280	126.0	405 ± 1	18 ± 1	48384 ± 1061	0.1279 ± 0.0004	4666 ± 17	2067 ± 3	4600 ± 17
UoM-7281	133.0	418 ± 1	36 ± 1	25323 ± 734	0.1324 ± 0.0003	4827 ± 12	2071 ± 3	4762 ± 12
UoM-7282	140.0	397 ± 1	43 ± 1	20399 ± 548	0.1354 ± 0.0005	4967 ± 18	2055 ± 3	4901 ± 18
UoM-7283	146.5	394 ± 1	54 ± 1	16433 ± 338	0.1371 ± 0.0004	5031 ± 15	2054 ± 3	4964 ± 15
LSCE-6896	152.5	412 ± 1	35 ± 1	2850 ± 17	0.1401 ± 0.0006	5101 ± 22	2085 ± 3	5037 ± 22
UoM-7284	153.5	392 ± 1	29 ± 1	32020 ± 664	0.1431 ± 0.0004	5303 ± 15	2030 ± 3	5237 ± 15
UoM-7286	167.5	397 ± 1	20 ± 1	48815 ± 1050	0.1499 ± 0.0007	5600 ± 27	2011 ± 3	5535 ± 27
UoM-7287	174.5	380 ± 1	23 ± 1	41931 ± 879	0.1526 ± 0.0004	5694 ± 17	2016 ± 3	5629 ± 17
UoM-7288	181.5	403 ± 1	34 ± 1	30673 ± 637	0.1565 ± 0.0004	5804 ± 18	2036 ± 3	5738 ± 18
UoM-7290	188.5	403 ± 1	30 ± 1	35448 ± 736	0.1604 ± 0.0004	5932 ± 17	2047 ± 3	5867 ± 17
UoM-7291	196.5	377 ± 1	38 ± 1	26581 ± 548	0.1645 ± 0.0005	6099 ± 20	2041 ± 3	6033 ± 20
LSCE-6898	202.5	376 ± 1	57 ± 1	1901 ± 10	0.1682 ± 0.0008	6207 ± 30	2063 ± 2	6142 ± 30
UHEI-6312*	219.0	404 ± 1	20 ± 1	11061 ± 376	0.1784 ± 0.0023	6595 ± 88	2063 ± 5	6531 ± 88

dft: distance from top. All uncertainties are $2\,\sigma$. *Measurement performed on an ICP-quadrupole MS (Thermo Fisher iCapQ). $^a(^{230}Th/^{238}U) = 1 - e^{-\lambda_{230}T} + (\delta^{234}U_{meas}/1000)[\lambda_{230}/(\lambda_{230}-\lambda_{234})][1 - e^{-(\lambda_{230}-\lambda_{234})T}]$, where T is age in years. $\lambda_{238} = 1.551 \cdot 10^{-10}\,a^{-1}$ (Jaffey et al. [1971]), UHEI and LSCE: $\lambda_{230} = 9.1577 \cdot 10^{-6}\,a^{-1}$, $\lambda_{234} = 2.8263 \cdot 10^{-6}\,a^{-1}$ (Cheng et al. [2000b]) UoM: $\lambda_{230} = 9.1705 \cdot 10^{-6}\,a^{-1}$, $\lambda_{234} = 2.8221 \cdot 10^{-6}\,a^{-1}$ (Cheng et al. [2013]).^{b}Years before measurement and without detrital Th correction. $^c\delta^{234}U = [(^{234}U/^{238}U) - 1] \cdot 1000$. $\delta^{234}U_{initial}$ was calculated based on ^{230}Th age (T), i.e., $\delta^{234}U_{initial} = \delta^{234}U_{initial}e^{\lambda_{234}T}$. ^{d}Corrected ^{230}Th ages assume the initial $^{230}Th/^{232}Th$ atomic ratio of $4.4 \pm 2.2 \cdot 10^{-6}$. Those are the values for a material at secular equilibrium, with the bulk earth $^{232}Th/^{238}U$ value of 3.8. The errors are arbitrarily assumed to be 50 %. ^{e}BP stands for "Before Present" where "Present" is defined as 1950 A.D.

6.5.1 Influence of aragonite on the growth rate

Riechelmann et al. [2014] state that the precipitation of aragonite is bound to very specific conditions. These are high fluid Mg/Ca ratios (≥ 0.5), high fluid pH (> 8.2) and low saturation indices for calcite (< 0.8), which are often associated with slow drip rates and hence, drier conditions. When comparing the GR of M39_764/1 with its aragonite/calcite layer positions (Fig. 6.4, red box: aragonite, blue box: mixed signals of aragonite/calcite, white: calcite), it seems the lowest GR corresponds to the aragonite layers, which could indicate a reduction of soil CO_2, which would be in accordance with the above mentioned specific conditions.

Table 6.2: U-series dating results of M39_764/1.

Sample ID	Depth (mm dft)	$[^{238}U]$ (ppb)	$[^{232}Th]$ (ppt)	$^{230}Th/^{232}Th$ (atomic $\cdot 10^{-6}$)	$(^{230}Th/^{238}U)^a$ (activity)	^{230}Th Age^b (a) (uncorrected)	$\delta^{234}U^c_{initial}$ (corrected)	^{230}Th Age^{d,e} (a BP) (corrected)
M39_764/1								
UHEI-6337*	6.0	243 ± 1	204 ± 1	156 ± 20	0.0076 ± 0.0010	152 ± 20	4622 ± 13	83 ± 20
LSCE-6880	10.0	305 ± 1	74 ± 1	608 ± 46	0.0085 ± 0.0007	164 ± 12	4715 ± 4	98 ± 12
LSCE-6881	15.5	306 ± 1	36 ± 1	2349 ± 172	0.0159 ± 0.0011	307 ± 22	4688 ± 5	242 ± 22
LSCE-6882	20.5	237 ± 1	57 ± 1	1156 ± 23	0.0162 ± 0.0003	312 ± 6	4683 ± 3	247 ± 6
UoM-7325	22.3	248 ± 1	28 ± 1	2006 ± 43	0.0154 ± 0.0001	273 ± 1	4620 ± 5	207 ± 2
UoM-7326	35.3	241 ± 1	155 ± 3	593 ± 12	0.0231 ± 0.0001	450 ± 2	4620 ± 5	382 ± 3
LSCE-6884	37.0	253 ± 1	200 ± 1	568 ± 12	0.0260 ± 0.0006	503 ± 10	4705 ± 4	435 ± 11
LSCE-6885	42.5	343 ± 1	43 ± 1	3926 ± 72	0.0285 ± 0.0005	549 ± 9	4699 ± 4	484 ± 9
UoM-7327	47.3	211 ± 1	21 ± 1	5768 ± 125	0.0344 ± 0.0001	669 ± 3	4627 ± 6	604 ± 3
UHEI-6476*	48.0	227 ± 2	72 ± 1	2051 ± 93	0.0394 ± 0.0018	775 ± 35	4588 ± 55	708 ± 35
LSCE-6886	50.0	251 ± 1	19 ± 1	1439 ± 16	0.0338 ± 0.0003	648 ± 6	4713 ± 3	583 ± 6
LSCE-6887	54.0	249 ± 1	40 ± 1	4028 ± 66	0.0375 ± 0.0006	724 ± 11	4682 ± 4	659 ± 11
UoM-7328	57.8	223 ± 1	36 ± 1	4069 ± 85	0.0403 ± 0.0001	788 ± 2	4610 ± 5	722 ± 2
LSCE-6888	60.0	248 ± 1	58 ± 1	3135 ± 46	0.0425 ± 0.0005	821 ± 10	4681 ± 4	755 ± 11
UoM-7329	71.0	210 ± 1	47 ± 1	3580 ± 74	0.0486 ± 0.0002	950 ± 3	4615 ± 4	884 ± 3
UoM-7330	84.3	369 ± 1	52 ± 1	6617 ± 137	0.0563 ± 0.0002	1102 ± 4	4606 ± 5	1039 ± 4
UoM-7331	97.5	405 ± 1	67 ± 1	6923 ± 142	0.0697 ± 0.0002	1366 ± 4	4605 ± 5	1300 ± 4
UHEI-6477*	102.0	233 ± 1	75 ± 1	4266 ± 114	0.0825 ± 0.0022	1631 ± 45	4578 ± 37	1565 ± 47
UoM-7332	111.0	210 ± 1	61 ± 1	4651 ± 95	0.0812 ± 0.0002	1602 ± 5	4574 ± 5	1536 ± 5
UoM-7333	125.0	197 ± 1	59 ± 1	6486 ± 138	0.1016 ± 0.0004	1956 ± 8	4601 ± 5	1889 ± 8
UHEI-6478*	131.0	221 ± 2	98 ± 1	3933 ± 210	0.1048 ± 0.0055	2094 ± 111	4536 ± 36	2027 ± 110
UoM-7334	138.8	311 ± 1	58 ± 1	9418 ± 193	0.1070 ± 0.0003	2110 ± 7	4595 ± 6	2044 ± 7
UoM-7335	152.3	194 ± 1	33 ± 1	11935 ± 355	0.1228 ± 0.0003	2425 ± 6	4600 ± 4	2359 ± 6
UHEI-6338*	159.0	1722 ± 2	163 ± 1	4325 ± 34	0.1328 ± 0.0009	2613 ± 18	4634 ± 7	2547 ± 18
UHEI-6408*	175.0	1867 ± 5	917 ± 5	5201 ± 80	0.1527 ± 0.0022	3034 ± 46	4599 ± 13	2966 ± 46
UoM-7337	179.0	1682 ± 7	27 ± 1	160141 ± 3394	0.1559 ± 0.0008	3100 ± 17	4582 ± 9	3035 ± 17
UoM-7338	192.5	376 ± 1	35 ± 1	37256 ± 801	0.1758 ± 0.0005	3516 ± 10	4563 ± 5	3450 ± 10
UoM-7339	205.5	212 ± 1	76 ± 2	8552 ± 174	0.1849 ± 0.0005	3701 ± 10	4565 ± 5	3634 ± 10
UHEI-6415*	210.0	239 ± 1	191 ± 1	28101 ± 431	0.1877 ± 0.0023	3768 ± 46	4564 ± 11	3699 ± 46
UoM-7340	218.5	219 ± 1	50 ± 1	13847 ± 284	0.1915 ± 0.0005	3843 ± 10	4554 ± 5	3777 ± 10
UoM-7341	233.0	196 ± 1	118 ± 2	5476 ± 111	0.2005 ± 0.0005	4016 ± 10	4570 ± 5	3948 ± 11
UHEI-6479*	238.0	219 ± 2	51 ± 1	14220 ± 523	0.1999 ± 0.0070	4036 ± 147	4536 ± 35	3970 ± 147
UoM-7342	248.0	207 ± 1	161 ± 3	4380 ± 89	0.2066 ± 0.0005	4148 ± 11	4563 ± 5	4079 ± 11
UoM-7343	262.0	287 ± 1	210 ± 4	4825 ± 98	0.2144 ± 0.0006	4296 ± 13	4577 ± 5	4228 ± 13
UHEI-6416*	270.0	230 ± 1	185 ± 1	4587 ± 61	0.2216 ± 0.0026	4441 ± 55	4596 ± 17	4372 ± 55
UoM-7344	277.0	546 ± 1	81 ± 2	24702 ± 507	0.2228 ± 0.0006	4481 ± 13	4562 ± 5	4415 ± 13
UoM-7345	289.0	278 ± 1	83 ± 2	12606 ± 257	0.2293 ± 0.0006	4633 ± 13	4541 ± 5	4567 ± 13
UHEI-6409*	290.0	2143 ± 4	609 ± 4	13403 ± 153	0.2267 ± 0.0022	4568 ± 47	4566 ± 15	4501 ± 47
UoM-7346	300.5	1297 ± 3	1539 ± 31	3150 ± 78	0.2266 ± 0.0033	4600 ± 69	4514 ± 6	4529 ± 69
UoM-7347	313.5	1847 ± 4	705 ± 14	10820 ± 221	0.2504 ± 0.0008	5055 ± 17	4560 ± 6	4988 ± 17
UHEI-6410*	330.0	2142 ± 5	155 ± 1	61134 ± 582	0.2635 ± 0.0022	5302 ± 48	4595 ± 15	5237 ± 49
UoM-7349	342.5	401 ± 1	57 ± 1	31910 ± 734	0.2745 ± 0.0007	5555 ± 15	4562 ± 5	5490 ± 15
UoM-7350	355.5	1710 ± 4	137 ± 3	58056 ± 1235	0.2813 ± 0.0008	5720 ± 18	4542 ± 6	5655 ± 18
UoM-7351	369.5	2075 ± 4	314 ± 2	54862 ± 1203	0.2934 ± 0.0017	6008 ± 37	4516 ± 10	5942 ± 37
UoM-7352	370.0	2083 ± 4	533 ± 3	19159 ± 192	0.2921 ± 0.0025	5978 ± 55	4523 ± 15	5911 ± 55
UHEI-6411*	380.0	840 ± 2	61 ± 1	69987 ± 1546	0.3064 ± 0.0010	6278 ± 21	4517 ± 6	6212 ± 21
UHEI-6480*	392.0	2382 ± 16	30 ± 1	75814 ± 1100	0.3153 ± 0.0048	6476 ± 105	4518 ± 28	6410 ± 107
UHEI-6339*	430.0	220 ± 1	105 ± 1	11857 ± 135	0.3393 ± 0.0034	6981 ± 72	4526 ± 8	6913 ± 72
UHEI-6417*	470.0	230 ± 1	98 ± 1	14064 ± 146	0.3606 ± 0.0034	7466 ± 77	4506 ± 18	7399 ± 77
UHEI-6412*	490.0	2360 ± 7	505 ± 2	28950 ± 233	0.3695 ± 0.0026	7672 ± 58	4496 ± 14	7606 ± 59
UHEI-6418*	505.0	221 ± 1	122 ± 1	11395 ± 108	0.3764 ± 0.0034	7844 ± 75	4482 ± 13	7776 ± 75
UHEI-6413*	537.0	2160 ± 4	236 ± 1	61642 ± 475	0.4023 ± 0.0024	8444 ± 56	4460 ± 13	8379 ± 57
UHEI-6419*	560.0	225 ± 1	161 ± 1	9813 ± 113	0.4192 ± 0.0045	8825 ± 100	4459 ± 12	8756 ± 100
UHEI-6481*	567.0	2423 ± 13	320 ± 2	53448 ± 758	0.4263 ± 0.0058	9102 ± 133	4388 ± 27	9037 ± 133
UHEI-6482*	595.0	2604 ± 16	277 ± 3	71498 ± 1265	0.4562 ± 0.0068	9849 ± 162	4351 ± 26	9784 ± 162
UHEI-6483*	601.0	2191 ± 19	148 ± 1	119244 ± 1168	0.4879 ± 0.0058	10559 ± 139	4359 ± 25	10494 ± 139
UHEI-6241*	612.0	1977 ± 4	581 ± 7	28635 ± 548	0.5079 ± 0.0075	11384 ± 177	4199 ± 11	11317 ± 178

For Explanations of dft, *, ^{a}, ^{b}, ^{c}, ^{d}, ^{e} see Tab. 6.1.

6.5.2 Legitimacy of the StalAge depth-models for growth rate determinations

Two independent calculation techniques were compared to test whether the GR pattern generated via the StalAge age-depth model is reliable. In Fig. 6.5a, GR were calculated using a StalAge age-depth model, while the step diagram in Fig. 6.5b shows the corresponding GR calculated by the difference of time Δt and space Δx given by discrete U-series ages. As the errors of the U-series ages are the dominating factor for the resolution of an appropriate GR pattern-to-noise ratio (U-series age errors are chosen to be $< 10\%$), an average temporal resolution of GR of $\Delta t \sim 220$ a was chosen for Fig. 6.5a and 6.5b. This corresponds to $\Delta x_{growthaxis} = 7$ mm (M6) and $\Delta x_{growthaxis} = 13$ mm (M39). A simple estimation yields that for GR errors $< 10\%$ with that given temporal and local resolution, the U-series age errors need to be
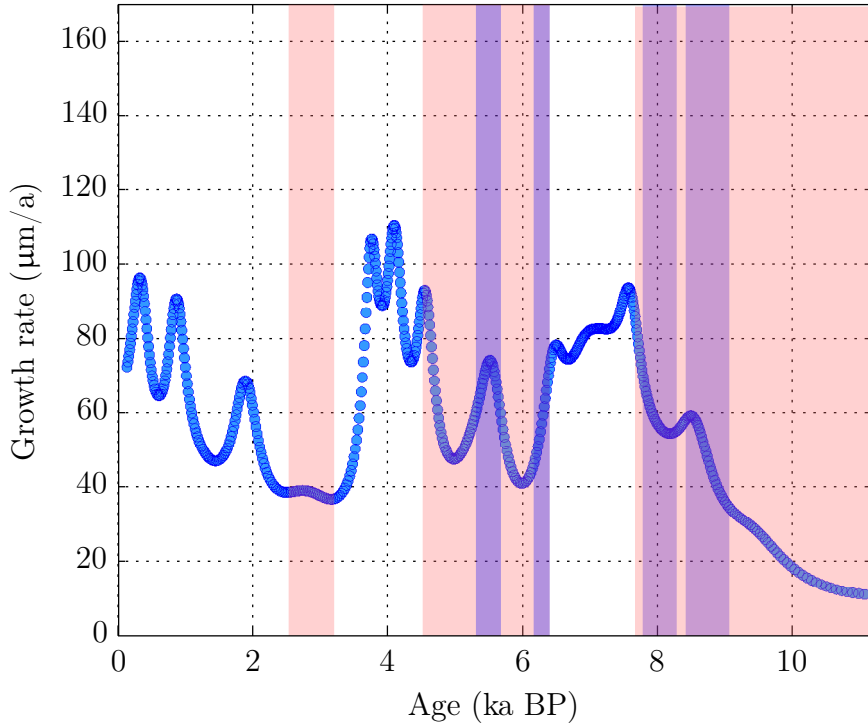
Figure 6.4: GR versus age of stalagmite M39_764/1. The GR of the aragonite layers is indicated by the red boxes, mixed signals of aragonite/calcite by blue ones, and calcite by white boxes. In general, low GR correspond to aragonite layers.

$< 15\,\mathrm{a}$ for the M6 and $< 19\,\mathrm{a}$ for the M39, respectively.

The U-series ages at UoM were generated with that constant $\Delta\mathrm{x}_{\mathrm{growthaxis}} = 7\,\mathrm{mm}$ and $13\,\mathrm{mm}$ and GR errors $< 10\,\%$ and hence, for reasons of simplicity, only the U-series ages determined at UoM were chosen for Fig. 6.5b. In Fig. 6.5a a sliding-window approach provides a big data set. Here, the GR yield an average error of $9\,\%$ (range: $0.04\,\%$ - $38\,\%$) for the M6 and of $6\,\%$ (range: $0.08\,\%$ - $27\,\%$) for the M39. Fig. 6.5 shows that GR pattern of both stalagmites can be by reproduced by both approaches, hence, the StalAge age-depth model seems appropriate.

6.5.3 Influence of offsets, spacing and time frames on the growth rate correlation coefficient r

In this section, it is examined whether a different spacing, i.e., a different Δt and Δx, an offset, or a specific time frame, changes the correlation coefficient r of the two GR patterns. It is assumed that a higher spacing of Δt and Δx (i.e. a lower resolution) could smooth dating, chemical fractionation, and sampling errors, as these errors could be mixed up with a real climate signal.
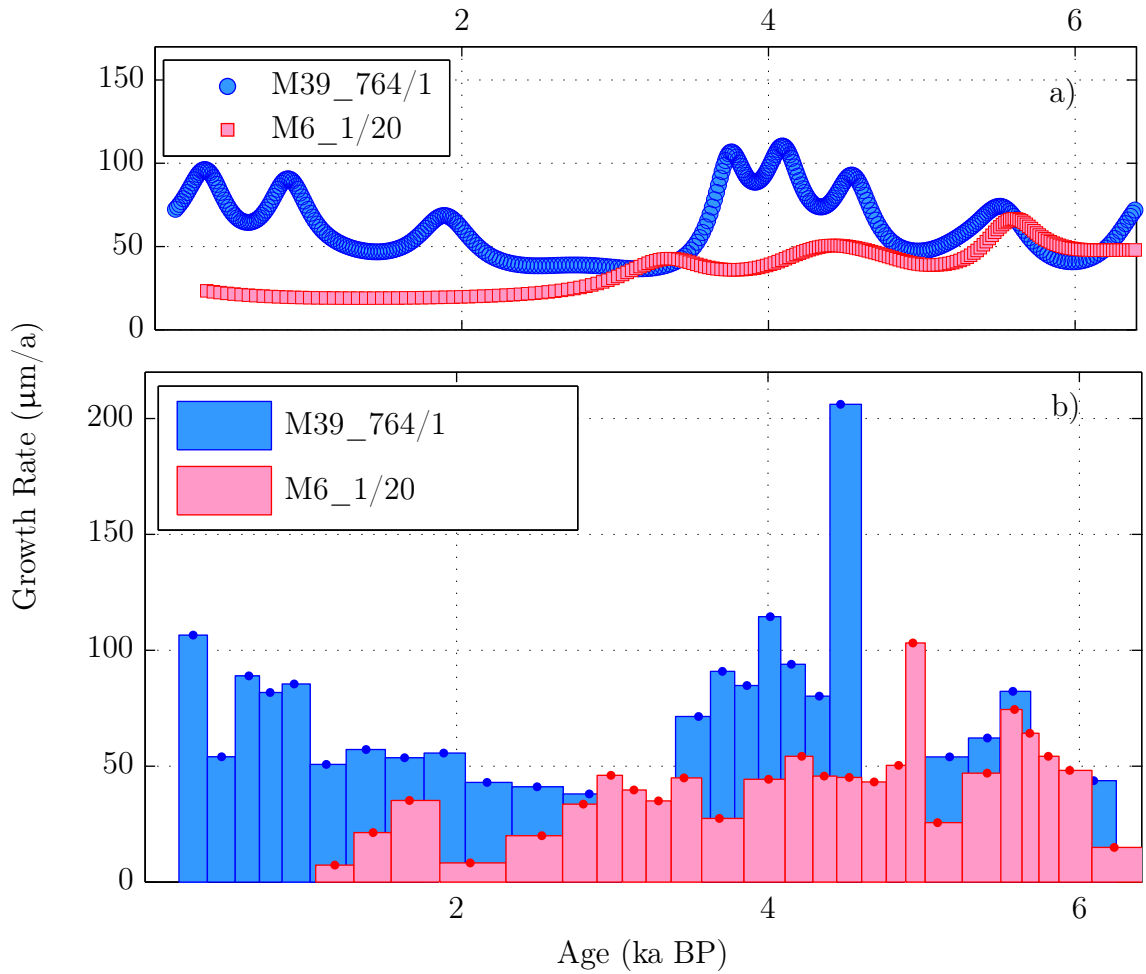
Figure 6.5: GR versus age in M6_1/20 (red) and M39_764/1 (blue). a) GR determined via the age-depth model, i.e. averaged over $\Delta t = 220\,a$, which corresponds to mean distances along the growth axes of $\Delta x = 7\,mm$ (M6_1/20) and $\Delta x = 13\,mm$ (M39_764/1). GR of both stalagmites are highly variable and do not correlate significantly ($r = 0.37$, $p = 0.25$). b) Step diagram of GR determined via the discrete U-series ages that have a constant $\Delta x = 7$ and $13\,mm$, respectively. The oscillation pattern agrees with the GR pattern obtained by StalAge. The difference in the amplitude of the GR to a) is explained by the lack of smoothing which is in contrast to age models. Nevertheless, the pattern of both GR shown in a) can be reproduced. Here as well, the GR of both stalagmites are highly variable and do not correlate significantly ($r = 0.44$, $p = 0.27$).
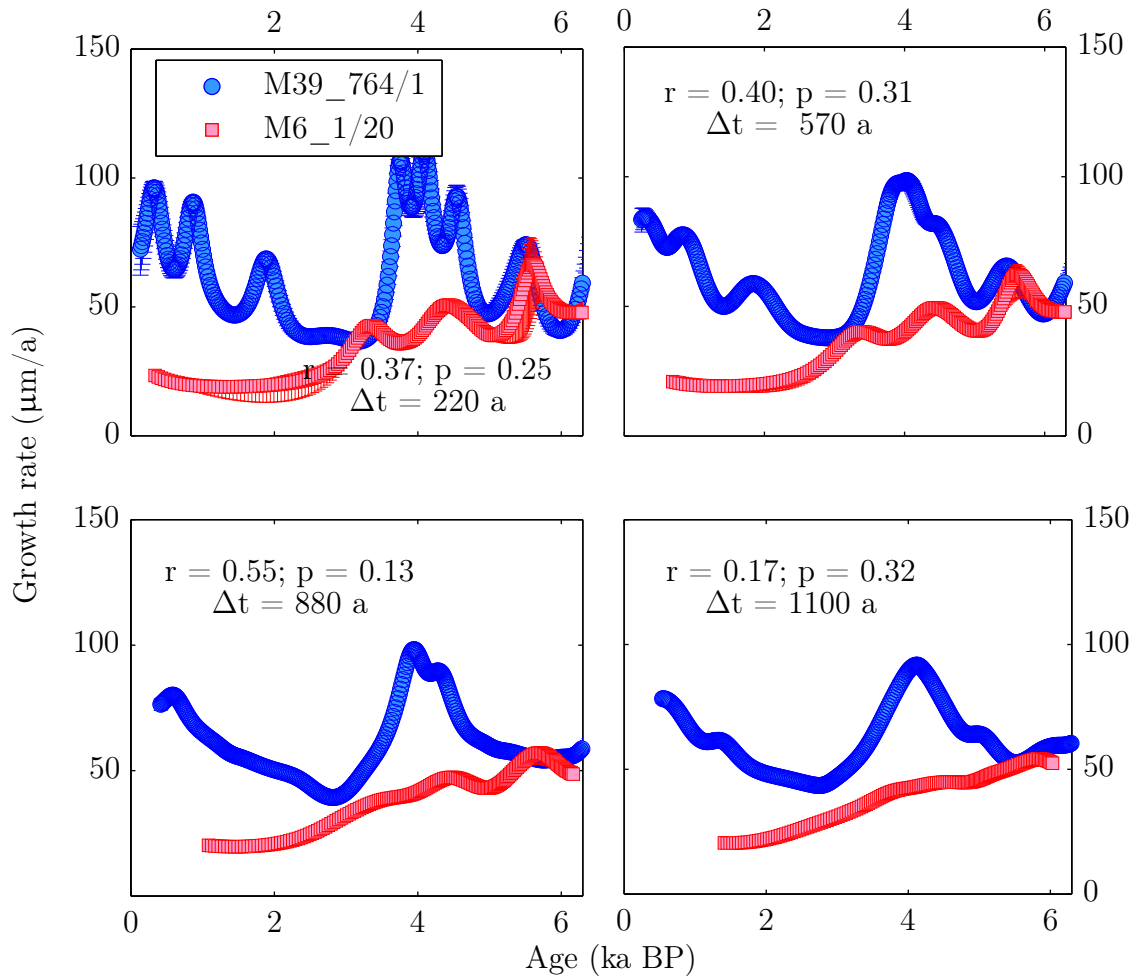
Figure 6.6: The change of the GR pattern of the two stalagmites as a function of temporal and local resolution. The coefficient r and the corresponding p values of the two GR pattern do not show an increase in correlation when varying the temporal resolution Δt.

Applying an offset of ± 100 a on one of the stalagmites' GR leads to a GR peak-matching at 5,600 a BP, if assuming a delay in GR-climate coherence in one of the two stalagmites. Also looking at certain time frames (between 6,400 to 2,300 a BP), when both GR patterns show oscillations could enhance coherence.

In Fig. 6.6 the change of the GR pattern of Fig. 6.5a of both stalagmites is shown as a function of temporal Δt and local resolution Δx. Nevertheless, the correlation coefficients r and their corresponding p values of the two GR pattern are always less than $r = 0.55$, when varying the temporal resolution Δt from 220 a up to 1,100 a. Fig. 6.7 shows that the specific time frame and an offset correction of 100 a also do not increase coherence ($r = 0.13$, $p = 0.25$). Consequently, for the purpose of this study, it is assumed that the two stalagmites' GR patterns are not significantly correlated.
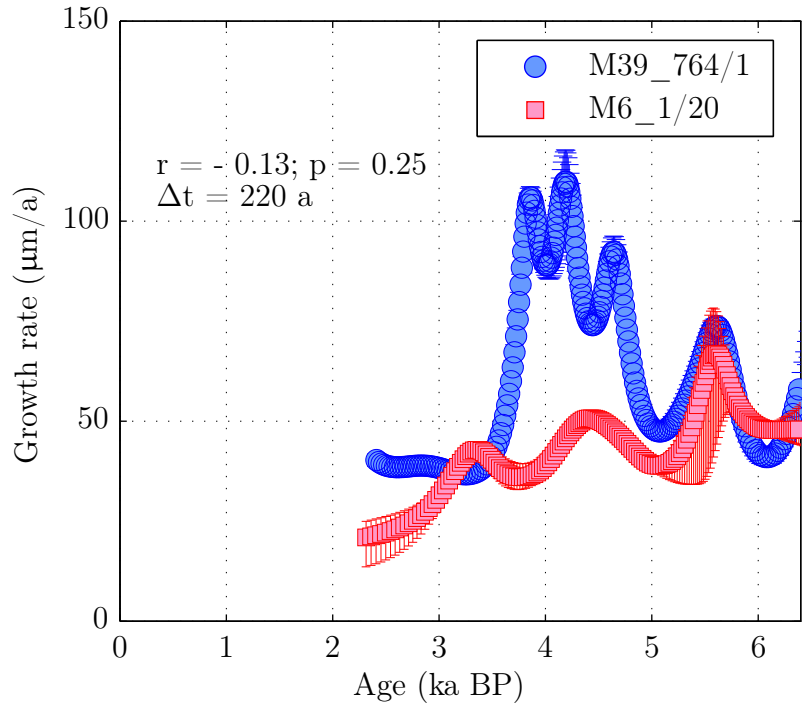
Figure 6.7: The change of the GR pattern of both stalagmites with an offset of 100 a, for the time interval of 6,400 to 2,300 a BP. The coefficient r and the corresponding p values of the two GR pattern do not show an increase in correlation ($r = -0.13$, $p = 0.25$).

6.5.4 Half-lives values for ^{234}U and ^{230}Th

The laboratories of LSCE and UHEI use the half-life values of ^{234}U and ^{230}Th published by Cheng et al. [2000b], as the values in Cheng et al. [2013] have not yet been generally accepted. An adoption of the new values would require the recalibration of all U and Th spikes and standards and reviewing of all available literature data.

However, in this study the U-series ages determined by UoM laboratory were calculated using the new 2013 values. The 2013 values deviate by about 1.5 ‰ from the old ones, which would result in approximately 1.5 ‰ younger ages for the determined UoM U-series ages. For the time span of interest to us ($\sim 6,550$ to 200 a BP), this difference is within dating precision, and hence, in this study the U-series ages are not normalized to the same half-life values.

6.6 Discussion

The speleothem GR is a function of the degree of supersaturation of the drip water with respect to calcite, drip rate, cave air [CO_2], and cave air temperature (e.g. Baker et al. [1998], Baker et al. [2016]; Kaufmann [2003]). It is controversial if speleothem growth itself is sensitive to temperature change, since a recent study of Baker et al. [2016] claim a lack of correlation between calcium concentration in drip water and temperature. The extent of calcite supersaturation of drip water is related to soil CO_2 supply to the groundwater, the subsequent host rock dissolution and the gradient between cave air and drip water [CO_2] (Baker et al. [2016]). These parameters are linked to the outside climate and thus, the precipitation of cave carbonate minerals can reflect climate variations to some extent. Hence, the replicability of speleothem proxy records could be a fundamental test for climate to GR correlations (e.g. Dorale and Liu [2009]). With that the GR pattern of one stalagmite could be inferred from an adjacent stalagmite's pattern, considering that the temporal and local resolution is high enough to detect minor fluctuations in climate conditions. Figure 6.8 shows, however, that secular speleothem GR variations in the two coeval stalagmites from Betten and Schratten Cave do not correlate through time tracing climate variance. Thus, the variations in GR cannot unequivocally be attributed to certain regional climate variables.

At the same time, in Fig. 6.8, consistent features in the GR pattern were found that must be related to changes of the above mentioned processes. Both stalagmites' GR variations are on a centennial scale and their GR range between less than $20\,\mu\mathrm{m\,a^{-1}}$ to more than $100\,\mu\mathrm{m\,a^{-1}}$. Hence, GR clearly depends on cave-specific characteristics, which are indicated, e.g. by marked differences in the U-isotopic composition (Tab. 6.1 and 6.2, Fig. 6.8) and the fact that M39 formed in a cave passage well below the present tree-line in contrast to M6 (Fig. 6.1).

Considering Fig. 6.8, M6 and M39 do expose a link between GR and climate on a local level as the GR evolution can be well explained when the data are compared to the tree-line reconstruction from the Central Alps of Austria (Nicolussi et al. [2005]), to the Alpine Holocene glacier evolution of Holzhauser [2007] and Holzhauser [2009], and with Solomina et al. [2015]. Therefore it is assumed that the CO_2 excess in the drip water may be the key to the lack of coherence in the secular GR changes. I will elaborate on this assumption by taking a closer look at Fig. 6.8.

The high-altitude site M6 shows a significant long-term change of the growth pattern, with no growth documented during the early Holocene, followed by a GR similar to the average high rates observed in stalagmite M39 between 6,550 and 3,000 a BP, and finally a period of slow growth until the present time. Due to its high altitude, stalagmite M6 started forming with a delay of $\sim 5,000\,\mathrm{a}$ (in comparison to M39) and with a delay of several hundred years compared to the known maximum tree-line altitude during the Holocene thermal maximum (Fig. 6.8). Hence, the GR of M6 might reflect the time needed to build up sufficient soil CO_2 supply to the infiltrating water, which can only happen upon significant glacier retreat, followed by enhanced vegetation cover.
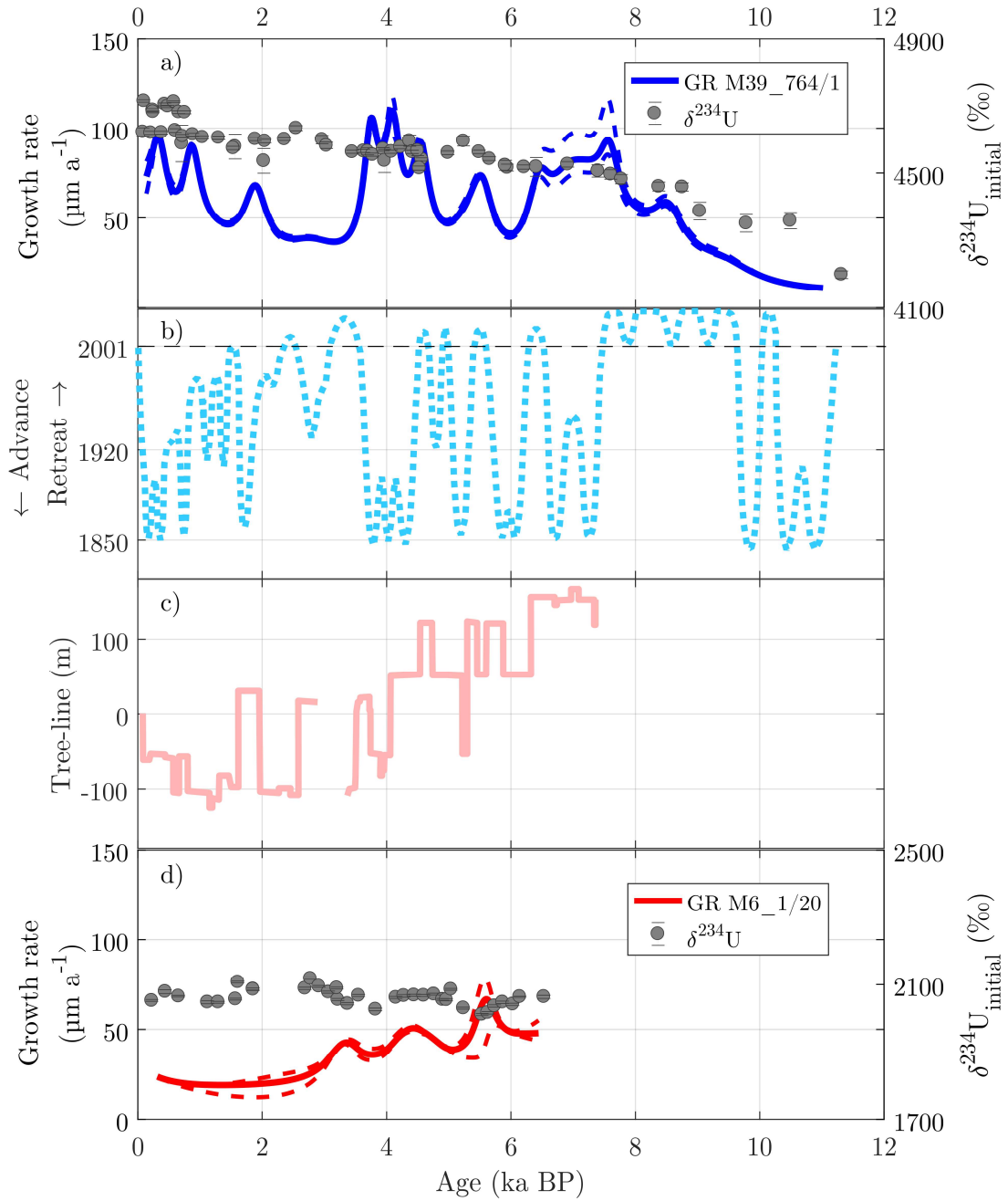
Figure 6.8: Comparison of different Holocene climate indicators in the Alps. a) Growth rate and $\delta^{234}U_{initial}$ of stalagmite M39_764/1. b) Glacier fluctuations (Holzhauser [2007], Holzhauser [2009]). Comparison of the glacier length with those in the years 1850 to 2007. c) Tree-line in the central Eastern Alps compared to today (Nicolussi et al. [2005]). Zero indicates the today's tree line at 2,245 m a.s.l. d) Growth rate and $\delta^{234}U_{initial}$ of stalagmite M6/1_20.

Until ∼3,500 a BP, the GR of M6 decreased parallel with the elevation of the tree-line and remained at a low level, as there was presumably not much vegetation in the catchment above the M6's site. Interestingly, stalagmite M6 did not stop growing until today, which is not only a likely explanation for a sparse vegetation cover above the M6's site, but also the result of the drip water's composition. Today's drip water has high sulfate values of about 240 mg/l (NeKO and Trüssel [2014]). Sulfide oxidation releases protons and enhances the dissolution capacity of the infiltrating water, hence growth could continue even during times of little vegetation (the M6 site lies below present-day tree line). At lower altitude in the nearby Betten Cave, M39 grew throughout the entire Holocene. After a twofold increase in GR between 11,000 and 9,000 a BP, a maximum GR was finally reached between 7,500 and 6,500 a BP, showing an oscillating pattern which changed on a centennial scale later on. The catchment above the M39 site was presumably always vegetated after 11,000 a BP, coincident with the end of the Younger Dryas cold reversal. Since 9,000 a BP the GR remained above 37 μm a^{-1} with subsequent centennial variability. This implies a fully developed vegetation cover in the catchment area above site M39 early within the Holocene, which is in contrast to Schratten Cave located at higher elevation.

It is assumed that the alternating growth pattern of M39 reflects changes in the degree of vegetation cover in the cave catchment area, which shows the same centennial variation as the oscillations of the alpine glaciers. Both, GR changes and glacier extension show a similarity with increasing carbonate deposition beginning after maximal glacier retreat, supporting the hypothesis of increased carbonate deposition induced by a well-established vegetation cover. Also, the highest eastern alpine tree-line values (Nicolussi et al. [2005]) coincide with the highest GR values of M39 starting at ∼7,800 a BP, underscoring the role of vegetation in controlling GR changes of M39. A descent of the tree-line around 4,000 a BP conforms to a lower vegetation density at given high-alpine altitude, subsequently limiting the supply of soil CO_2 to the infiltrating water one to two centuries later. The U-isotopic composition (Fig. 6.8) yields further evidence of the hydrogeochemical evolution, as values increased much more pronounced until 6,550 a BP, after which the increase slowed down and gave way to secular variations, possibly indicative of changes in extent of water-rock interaction linked to the soil water CO_2 content. Those observed secular variations in $\delta^{234}U_{initial}$ are in accordance with the observed ones for the M6 in the same time frame starting at 6,550 a BP.

6.6.1 $\delta^{234}U_{initial}$ variation

On geological time scales, the radioactive equilibrium between ^{238}U and ^{234}U is established and the activity ratio ($^{234}U/^{238}U$) should be unity in a closed system. However, in meteoric aquatic systems this is rarely observed. In most cases an excess of ^{234}U is observed in aquatic systems apart from rare cases of depletion of ^{234}U over equilibrium ^{238}U in solution (Bourdon et al. [2003]; Ivanovich and Harmon [1992]). Here, a deviation from radioactive equilibrium between ^{234}U and ^{238}U has been found in the case for M39 and M6 (Fig. 6.9).
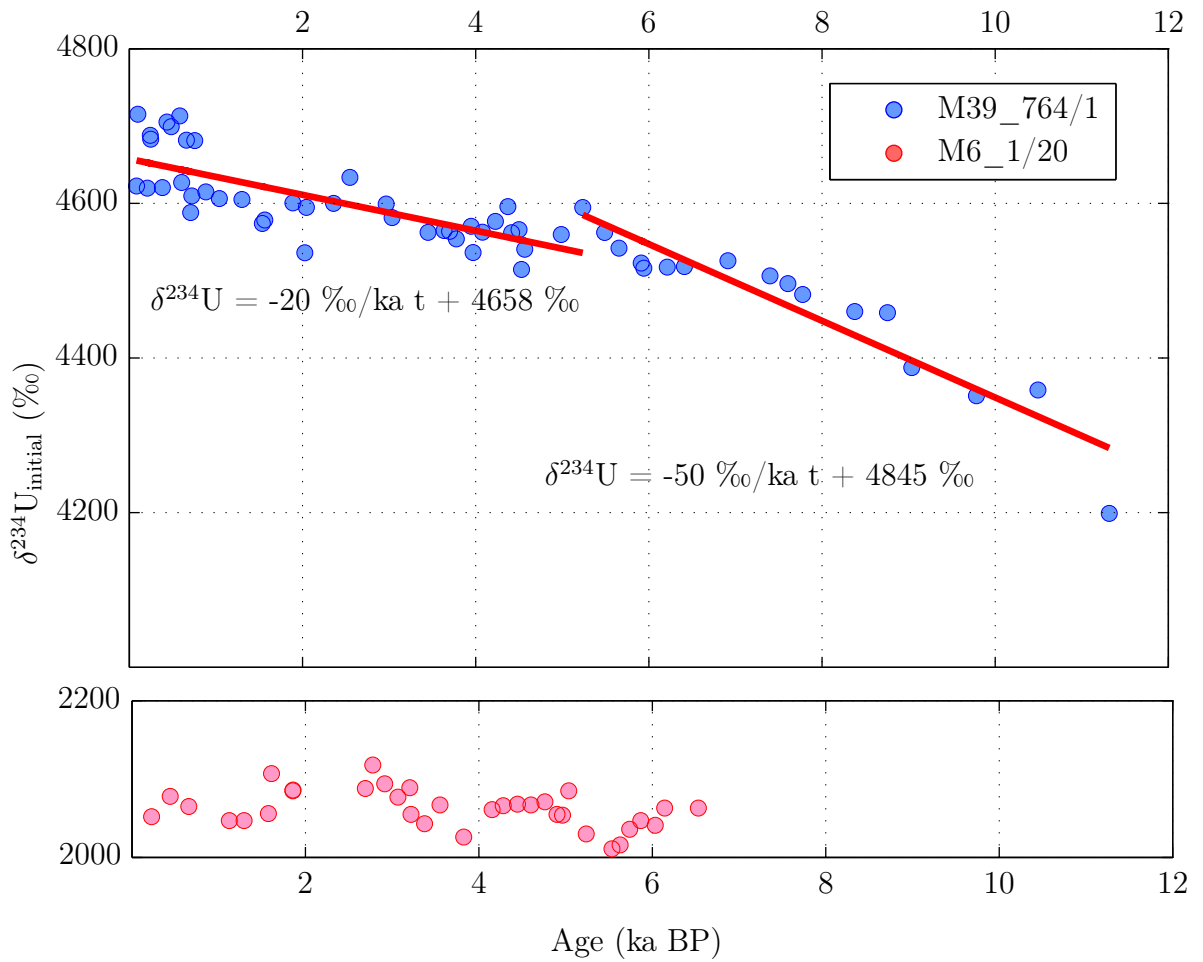
Figure 6.9: $\delta^{234}U_{\text{initial}}$ distribution of M39_764/1 and M6_1/20 versus age. The $\delta^{234}U_{\text{initial}}$ is a measure of the fractional deviation from the $(^{234}U/^{238}U)$ atom ratio from the value at secular equilibrium during calcite formation. The $\delta^{234}U_{\text{initial}}$ of M39_764/1 is approximately twice as high as the one of M6_1/20. Furthermore, M39 shows the trend of an average $35\,\%_0/\text{ka}$ increase of $\delta^{234}U_{\text{initial}}$ in the last $\sim 11,400\,\text{a}$.

The used $\delta^{234}U_{initial}$ is a measure of the $(^{234}U/^{238}U)$'s fractional deviation from secular equilibrium (Cheng et al. [2000b]). The observed disequilibrium is high with 2,000 to 4,200 ‰ indicative of an important contribution of recoil ^{234}U to the groundwater system. The $\delta^{234}U_{initial}$ is approximately twice as high for the M39 as it is for the M6 and increased gradually over the last 11,600 a for the M39. The slope of the $\delta^{234}U_{initial}$ of the M39 decreased abruptly from 50 ‰/ka to 20 ‰/ka at $\sim$5,200 a BP. For the past 5,200 a BP, the slope of 20 ‰/ka is overprinted with a secular variability of ±50 ‰, which, however, is small compared to the long term trend of $\delta^{234}U_{initial}$. In contrast, the M6 does not show a significant trend and scatters about 2,600 ± 30 ‰ during the last 6,600 a.

Several explanatory models for the disequilibrium have been proposed and some have been supported by laboratory experiments. The discussed causes for the disequilibrium range from leaching from radiation-damaged sites (also known as "hot atom" or "Szilard-Chalmers" effect) (Cherdyntsev and Kazachevskii [1965]), over α recoil into solution, up to oxidation of U(IV) to a more soluble uranyl ion $U(VI)O_2^{2+}$ (dependent on a reducing or oxidizing environment) (Suksi et al. [2006]). Furthermore, Osmond and Cowart [1976] found a general inverse correlation such that, for a given area, higher $\delta^{234}U_{initial}$ were often associated with lower [U]. It is assumed that, as natural water gets depleted from the recharge zone, conditions become more reducing and loss of U from solution to the aquifer walls occurs. Also, the residence time of natural waters and the porosity of the bedrock influence $\delta^{234}U_{initial}$ (Banner et al. [1990]; Petersen et al. [2013]).

It is not known exactly, which of the reasons, (i.e. high residence time, high porosity of the bedrock, high distance to recharge zone and a reducing environment), cause the relatively high $\delta^{234}U_{initial}$, but it is evident that the two investigated stalagmites originate from a differing hydrological path and geochemistry.

At the high altitude soil CO_2 might not have a major influence on the $\delta^{234}U_{initial}$ of the M6, but high sulfate values could provide a reducing environment (Suksi et al. [2006])site. In addition, the transport pathways of water at the high alpine Schratten Cave sample an upper level of the karst compared to the water dripping at M39 in the Betten Cave. Hence, supposing high soil CO_2 fluxes to the infiltrating water at the Betten Cave and slightly more acidity to dissolve the host rocks, one would expect a significant difference in the leaching behavior of excess ^{234}U matching with the observations. Orogenesis, e.g., could have an impact on the path and the environment of the dripping water and might be another explanation for the $\delta^{234}U_{initial}$ drift over time as observed for M39. Hence, it may be simply concluded that the two growth pattern expresses local differences of the infiltration and transport pathway of water, and possibly its chemical state, and the amount. Nevertheless, a proper explanation of the observed difference between the stalagmites and the long term trend requires further analysis of the dripping waters, host rock weathering patterns and the water residence time.

6.7 Conclusion

Precisely dated Holocene speleothem records from central Switzerland were investigated with regard to their GR and possible correlations between those deposition rates and their $\delta^{234}U_{initial}$ values. It is shown that the $\delta^{234}U_{initial}$ distributions of both stalagmites are very different between the two stalagmites (an obvious increasing trend over time versus an unbiased scatter), caused most likely by different drip water paths and hydrogeochemistry. It is further demonstrated that with a high resolution of $\Delta t \sim 220\,a$, climate signals cannot unequivocally be responsible for the GR pattern of two adjacent stalagmites on sub-millennial time scales.

GR and hydrogeochemistry should be treated with great care when deriving and comparing climate proxy information from stalagmites solely based on the magnitude of carbonate precipitation. At the same time, the combination of the two stalagmites' GR does provide useful insights into the local paleoclimate and demonstrate that an individual growth record does by far not capture major climate change. The two stalagmites, while not giving regional climate insights, expose a climate-GR link regarding the alpine vegetation. The presumption is, that the GR and the stalagmites' hydrogeochemistry, as evidenced by the U-isotopic composition, evolved individually and independently. Both appear to be influenced by changing vegetation cover in the catchment.

Summing up, it was shown that each stalagmite is influenced by the geochemical controls exerted through climate change, here variable glacier extend and predominantly vegetation and soil CO_2. However, persistent and reproducible GR patterns indicative of such regional climate controls cannot be derived on time scales of centuries.

7 Conclusion and outlook

In this thesis it was shown that routinely, measurements on low per mil to up to ε-scale precision of U-series dating is feasible. Here, ε-precision is meant regarding to the errors on the activity ratios which mainly results in age errors on per mil-scale. In the context of this work, a MATLAB standalone program *UThAnalysis* for fast data analysis was developed. By means of that, two application studies for paleoclimatic research were presented which highlight the advantages and the newly obtained possibilities of high-precision U-series dating. The first study is a reevaluation of already published data. The reevaluated data seem to be more consistent with the Milancovic hypothesis than the formerly published data by shifting the initial warming by $\sim 2\,\mathrm{ka}$ in that Alpine region. In the second application study a unique dating record set was generated resolving the GR pattern of two adjacent Alpine stalagmites with a high temporal resolution of $\Delta t = 220\,\mathrm{a}$ over the last $6{,}500\,\mathrm{a}$.

Chap. 4 and 5 discussed the reproducibility of our data approach regarding applied data corrections, measurement protocols and chemical procedures compared to protocols used by other institutes or for different mass spectrometer types. The results presented in the two chapters show that the UHEI Neptune instrument performs similarly compared to other Neptune instruments (LSCE and UoM) (see Tab. 5.2). Furthermore, for signals higher than $11\,\mathrm{mV}$ a standard reproducibility on ε-precision is achieved (Fig 4.16). The applied data correction scale on the order of ε-units for regular samples (Emmertal3 and GeoB) support the feasibility of ε-dating. In this study we even succeeded in reproducibly measuring the age of the SPA-52 sample on ε-scale. Especially, the error of SPA-52 was controversially discussed, as maximum daily tailing corrections of $30\,\%$ affects the age of SPA-52 by $\sim 14\,\varepsilon$-units. This uncertainty was cleared by measuring this sample using different detector setups and chemical preparations all agreeing with $2\,\sigma$ errors. Hence, it is most likely that $30\,\%$ daily tailing variations were overestimated and variations $< 20\,\%$ might be more realistic.

Furthermore, another dating technique beneficial for samples with low [U] and [Th] was introduced; the separated measurement of the U and Th fractions. With this measurement, statistics can be improved and the impact of the ^{238}U tailing correction on isotope ^{230}Th is reduced. Measurements with either separated or combined U and Th fractions show activity ratios reproducible on $1.6\,\permil$-scale.

Our instrumental setup is limited to the concentrations of our sample solutions in the fg/ml-regime. C09-2 contained unusually low [U] and [Th] leading to corrections on the scale of $8\,\%$ of its age. Hence, the obtained resolution for samples at the detection limit younger than $390\,\mathrm{a}$ is $31\,\mathrm{a}$ larger than the instrumental error of $25\,\mathrm{a}$.

To further support ε-precision dating, future studies should recalibrate the spikes for ε-precision. Furthermore, similar to SPA-52, most samples naturally contain relatively low [U] and, in particular, [Th], an alternative procedure to achieve ε-precision could be developed. (1) Technical improvements that increase the transmission efficiency by an order of magnitude (currently 1 - 2 %) and (2) the decrease of the baseline noise by cooling the electronics ($U_R \sim \sqrt{T}$) could help to gain ε-precision. Furthermore, an altered measurement setup with two $10^{13}\,\Omega$ amplifiers (see Tab. 4.5) would establish simultaneous measurements for all isotopes and allow for the decay time to be set to $0\,\text{s}$ as each cup's signal remains from the same isotope. Additionally, a dilution of the sample to only $0.5\,\text{ml}$ rather than $2\,\text{ml}$ would decrease the measurement time to $5\,\text{min}$, $300\,\text{runs}$ of $1\,\text{s}$, and increase the concentration by a factor of 4.

At this point I would like to stress the importance to fully automate the data analysis. Currently, the final age determinations and data result presentations are done via a Microsoft *Excel* sheet with the main focus on the tabular and user-friendly representation. U-series ages are also determined at the iCapQ, TIMS and via laser ablation coupled to the iCapQ or the Neptune generating different data files. Including these data files in one global data analysis standalone program is beneficial. Since the foundation and the idea were already developed in the course of this work, this task would be relatively quick to realize.

High-precision dating helps to reevaluate the timing of events in Earth's history. In Chap. 5 and 6 highly precisely dated speleothem records from the Northern Alps in Austria and from central Switzerland were investigated. Our precise dating technique reevaluated the beginning of the warming of termination II in the northern Austrian Alps at Spannagel Cave. The newly obtained date for the start of the deposition of flowstone SPA-52 is $133.187 \pm 0.833\,\text{ka BP}$ and $2,000\,\text{a}$ later than $135 \pm 1.2\,\text{ka BP}$ as published in Spötl et al. [2002]. With that date a better estimate of the beginning of the warming in that region is given which further matches with stalagmite data from the close proximity. These data show that the growth of the flowstone took place at the turning point of the boreal summer insolation curve (Fig. 5.3) and are more consistent with the Milankovitch hypothesis than the formerly published results.

In Chap. 6 two stalagmites from Betten and Schratten Cave in central Switzerland were investigated with regard to their growth rates and possible correlations between these deposition rates and their $\delta^{234}U_{\text{initial}}$ values. The $\delta^{234}U_{\text{initial}}$ patterns are very different between the two stalagmites (an obvious increasing trend over time versus an unbiased scatter). This is caused most likely by different drip water paths and hydrogeochemistry. It is shown that with a high resolution of $\Delta t \sim 220\,\text{a}$, climate signals cannot unequivocally be responsible for the GR pattern of two adjacent stalagmites on sub-millennial time scales. However, the combination of the two stalagmite's GR does provide useful insights into the local paleoclimate on millenial time scales.

While the observations are focused on the missing fundamental knowledge on groundwater flow path, hydrogeochemistry, and vegetation, a further validation of those results by comparing the data to other paleoclimatic archives from that

Alpine region would be recommended. Additionally, monitoring drip water samples throughout the whole cave system and over time could help to evaluate and to understand these different $\delta U_{initial}$ trends of both stalagmites. To measure additional stalagmites from the same cave (either Betten or Schratten) that overlap the same growth interval would also help understand growth rate patterns.

Summing up, routinely high-precise U-series measurements for continental and marine carbonates were established in our laboratory at the Institute of Environmental Physics at Heidelberg University. The initial goal to demonstrate the feasibility of ε-precision U-series dating was reached and the technological limitations of present day mass spectrometry were demonstrated. The developed measurement protocols, instrument performances, dating corrections, and chemical protocols are exceedingly reproducible with respect to long term measurments, using various mass spectrometers and chemical protocols, and in comparsison with other well-established U-series dating laboratories. So far, the extent of instrumental corrections on the activity ratios have never been shown in such detail. Our precise U-series measurement technique helped to reevaluate data and to assess speleothem GR as a climate proxy.

Appendices

A Lists

A.1 List of Figures

A.2 List of Tables

B Data

Table B.1: U-series dating results of the SPA-52 flowstone from Spannagel Cave, Austria.

Sample ID	Instrument	Detectors	Depth (cm dft)	[238U] (ppb)	[232Th] (ppt)	(230Th/232Th)^a (activity)	(230Th/238U)^a (activity)	230Th Age^b (a) (uncorrected)	δ234U_initial^c (corrected)	230Th Age^{d,e} (a BP) (corrected)
SPA-52										
LSCE-6573	Neptune	FC+SEM	2.1	2851.3 ± 1.2	1818.1 ± 6.3	3275 ± 18	0.6830 ± 0.0029	121322 ± 1065	22.3 ± 3.0	121240 ± 1069
UHEI-2429	TIMS*	FC+SEM	2.1	3096.0 ± 4.0	1628.8 ± 6.4			122501 ± 1786	16.5 ± 2.5	122432 ± 1786
UHEI-6573	iCap	SEM	2.1	2879.0 ± 14.7	1765.9 ± 12.5	3397 ± 28	0.6838 ± 0.0045	121732 ± 2301	21.7 ± 10.3	121650 ± 2302
LSCE-6572	Neptune	FC+SEM	2.5	3110.0 ± 0.8	3736.7 ± 11.4	1718 ± 8	0.6740 ± 0.0024	118313 ± 820	22.7 ± 1.7	118216 ± 826
UHEI-2414	TIMS*	FC+SEM	2.5	3125.6 ± 4.1	2642.0 ± 7.9			123345 ± 1286	12.1 ± 1.9	123267 ± 1286
UHEI-6572	iCap	SEM	2.5	3145.3 ± 10.6	3714.6 ± 15.8	1759 ± 13	0.6817 ± 0.0047	120207 ± 2267	26.7 ± 9.8	120109 ± 2293
LSCE-6571	Neptune	FC+SEM	3.3	3391.4 ± 0.8	9749.0 ± 35.8	711 ± 4	0.6665 ± 0.0028	117055 ± 939	16.3 ± 2.0	116910 ± 942
UHEI-2314	TIMS*	FC+SEM	3.3	3675.6 ± 3.7	9385.7 ± 18.8			122102 ± 793	14.7 ± 1.4	121976 ± 792
UHEI-6571	iCap	SEM	3.3	3424.6 ± 9.1	9579.1 ± 35.9	729 ± 4	0.6689 ± 0.0035	119256 ± 1688	9.4 ± 7.4	119111 ± 1765
LSCE-6569	Neptune	FC+SEM	4.8	107068.1 ± 18.3	118387.6 ± 393.6	1991 ± 10	0.7200 ± 0.0025	134245 ± 941	22.0 ± 1.6	134214 ± 941
UHEI-2317	TIMS*	FC+SEM	4.8	105072.8 ± 178.6	126510.8 ± 607.3			133495 ± 1842	16.7 ± 2.7	133408 ± 1842
UHEI-6569	iCap	SEM	4.8	107867.6 ± 463.0	109272.2 ± 689.1	2167 ± 19	0.7231 ± 0.0055	135431 ± 2351	22.4 ± 6.0	135337 ± 2381
UHEI-7128	Neptune	FC	4.8	82705.8 ± 13.8	225.2 ± 0.3	815 ± 1	0.7207 ± 0.0009	133819 ± 359	25.3 ± 0.5	133677 ± 358
UHEI-7964	Neptune	FC+10^{13}Ω	4.8	124932.2 ± 18.6	79.0 ± 0.2	3477 ± 1	0.7195 ± 0.0002	133718 ± 127	23.6 ± 0.5	133635 ± 127
LSCE-6568	Neptune	FC+SEM	5.2	102975.3 ± 53.7	232.1 ± 0.7	985 ± 4	0.7259 ± 0.0022	133441 ± 908	36.4 ± 2.4	133314 ± 909
UHEI-2318	TIMS*	FC+SEM	5.2	103589.0 ± 31.1	76196.8 ± 411.5			136117 ± 1603	19.2 ± 1.4	136042 ± 1602
UHEI-6568	iCap	SEM	5.2	104266.8 ± 329.7	227844.4 ± 1173.8	1010 ± 7	0.7270 ± 0.0038	133950 ± 1702	36.8 ± 4.9	133825 ± 1696
UHEI-7129	Neptune	FC	5.2	117792.5 ± 29.6	163 ± 0.6	1614 ± 8	0.7261 ± 0.0026	134240 ± 940	32.8 ± 0.6	134136 ± 940
UHEI-7965	Neptune	FC+10^{13}Ω	5.2	127855.6 ± 23.9	37047 ± 11.5	7644 ± 4	0.7244 ± 0.0003	133782 ± 139	32.1 ± 0.4	133708 ± 139
LSCE-6567	Neptune	FC+SEM	5.6	93891.9 ± 13.7	99449 ± 663.7	2090 ± 21	0.7238 ± 0.0052	134027 ± 1875	29.7 ± 1.6	133933 ± 1875
UHEI-2319	TIMS*	FC+SEM	5.6	100619.6 ± 171.1	85715 ± 360.0			135219 ± 1333	24.3 ± 2.8	135189 ± 1333
UHEI-6567	iCap	SEM	5.6	94410.1 ± 288.2	92221 ± 0.4	2266 ± 15	0.7326 ± 0.0042	137378 ± 1965	29.9 ± 5.7	137285 ± 2002
UHEI-7183	Neptune	FC	5.6	94434.4 ± 13.6	103 ± 0.1	2035 ± 1	0.7210 ± 0.0002	132607 ± 111	30.3 ± 0.4	132512 ± 112
UHEI-7966	Neptune	FC+10^{13}Ω	5.6	85353.7 ± 11.8	113 ± 0.1	1657 ± 1	0.7182 ± 0.0002	132571 ± 113	28.4 ± 0.5	132368 ± 114
LSCE-6566	Neptune	FC+SEM	6.0	76146.7 ± 12.3	137276 ± 404.4	1225 ± 5	0.7221 ± 0.0024	132668 ± 917	33.3 ± 1.5	132554 ± 917
UHEI-2320	TIMS*	FC+SEM	6.0	64518.2 ± 167.7	136859 ± 2052.9			133509 ± 1548	27.3 ± 2.3	133419 ± 1547
UHEI-6566	iCap	SEM	6.0	76590.5 ± 237.2	128113 ± 622.2	1322 ± 8	0.7319 ± 0.0036	135900 ± 1808	35.9 ± 5.9	135788 ± 1807
UHEI-7184	Neptune	FC	6.0	83802.2 ± 14.5	131735 ± 71.8	1411 ± 1	0.7202 ± 0.0002	132581 ± 123	30.4 ± 0.4	132472 ± 123
UHEI-7967	Neptune	FC+10^{13}Ω	6.0	80078.6 ± 9.4	119892 ± 17.5	1464 ± 1	0.7169 ± 0.0003	132312 ± 150	26.3 ± 0.5	132204 ± 152
LSCE-6565	Neptune	FC+SEM	6.4	88539.0 ± 16.3	77079 ± 336.0	2574 ± 15	0.7340 ± 0.0028	134855 ± 1043	43.7 ± 1.4	134767 ± 1037
UHEI-2321	TIMS*	FC+SEM	6.4	87516.5 ± 131.3	42381 ± 178.0			134214 ± 1276	27.3 ± 2.3	134147 ± 1276
UHEI-6565	iCap	SEM	6.4	89077.8 ± 314.3	67044 ± 327.5	2967 ± 21	0.7328 ± 0.0045	135147 ± 2152	40.7 ± 6.6	135061 ± 2150
UHEI-7185	Neptune	FC	6.4	79918.7 ± 15.1	70003 ± 41.8	2567 ± 2	0.7301 ± 0.0002	134259 ± 121	39.7 ± 0.4	134170 ± 122
UHEI-7968	Neptune	FC+10^{13}Ω	6.4	52885.0 ± 5.5	219653 ± 31.1	540 ± 1	0.7341 ± 0.0002	134197 ± 129	47.2 ± 0.6	134017 ± 140
LSCE-6570	Neptune	FC+SEM	6.8	80678.4 ± 84.4	9412 ± 421.2	1826 ± 11	0.7265 ± 0.0032	132460 ± 1266	42.1 ± 3.0	132363 ± 1272
UHEI-2391	TIMS*	FC+SEM	6.8	41353.6 ± 53.8	71684 ± 229.4			138284 ± 1258	28.5 ± 2.0	138182 ± 1258
UHEI-6570	iCap	SEM	6.8	80734.3 ± 215.1	80869 ± 457.6	2249 ± 17	0.7422 ± 0.0044	135205 ± 1799	56.9 ± 4.5	135113 ± 1799
UHEI-7969	Neptune	FC+10^{13}Ω	6.8	88558.1 ± 15.3	46398 ± 12.2	4217 ± 2	0.7227 ± 0.0002	132237 ± 121	36.6 ± 0.5	132156 ± 122

dft: distance from top. All uncertainties are 2σ. *(230Th/238U) and (230Th/232Th) missing data from 2004. $^{a}(^{234}U/^{238}U) = 1 − e^{−λ_{230}T} + (δ^{234}U_{meas}/1000)[λ_{230}/(λ_{230}−λ_{234})][1−e^{−(λ_{230}−λ_{234})T}]$, where T is age in years. $λ_{238} = 1.551·10^{-10}$ a^{-1} (Jaffey et al. [1971]), $λ_{230} = 9.1577·10^{-6}$ a^{-1}, $λ_{234} = 2.8263·10^{-6}$ a^{-1} (Cheng et al. [2000b]). ^{b}Years before measurement and without detrital Th correction. $^{c}δ^{234}U_{initial}$ was calculated based on 230Th age (T), i.e., $δ^{234}U_{initial} = δ^{234}U_{meas}e^{λ_{234}T}$. ^{d}Corrected 230Th ages assume the initial 230Th/232Th atomic ratio of $4.4 ± 2.2·10^{-6}$. Those are the values for a material at secular equilibrium, with the bulk earth 232Th/238U value of 3.8. The errors are arbitrarily assumed to be 50%. ^{e}BP stands for "Before Present" where "Present" is defined as 1950 A.D.

Table B.2: U-series dating results of MI5 from Socotra Island, Yemen.

Sample ID	Depth (cm dft)	[^{238}U] (ppb)	[^{232}Th] (ppt)	(^{230}Th/^{232}Th) (activity)	(^{230}Th/^{238}U)[a] (activity)	^{230}Th Age[b] (a) (uncorrected)	δ^{234}U[c] initial (corrected)	^{230}Th Age[d,e] (a BP) (corrected)
MI5								
UoM								
7242a	13.7	1107.1 ± 6.6	456.13 ± 9.62	3939 ± 87	0.0984 ± 0.0009	11921 ± 118	-50.4 ± 2.7	11843 ± 118
7242b	13.7	1112.5 ± 3.1	455.97 ± 9.27	3939 ± 81	0.0979 ± 0.0004	11836 ± 58	-48.7 ± 1.2	11758 ± 58
7243a	17.2	1685.9 ± 7.4	1749.09 ± 35.92	1583 ± 33	0.0996 ± 0.0006	11980 ± 87	-43.6 ± 2.2	11883 ± 90
7243b	17.2	1691.4 ± 4.3	1758.09 ± 35.51	1577 ± 32	0.0994 ± 0.0004	11982 ± 53	-45.3 ± 1.2	11885 ± 57
7244	20.4	1243.2 ± 4.3	134.54 ± 2.78	5156 ± 106	0.0992 ± 0.0005	12018 ± 70	-50.2 ± 1.6	11949 ± 70
7245	23.3	1515.0 ± 4.4	487.97 ± 9.92	15115 ± 318	0.1007 ± 0.0005	12118 ± 60	-43.1 ± 1.3	12043 ± 60
7246a	25.6	2813.8 ± 9.3	153.45 ± 3.17	30514 ± 640	0.1009 ± 0.0005	12241 ± 67	-50.4 ± 1.4	12175 ± 67
7246b	25.6	2805.8 ± 14.2	154.04 ± 3.21	30435 ± 649	0.1013 ± 0.0007	12329 ± 94	-53.0 ± 2.2	12262 ± 94
7247	28.6	1485.5 ± 3.8	1843.94 ± 37.07	1355 ± 27	0.1020 ± 0.0004	12366 ± 52	-49.3 ± 1.7	12263 ± 58
7248	31.8	1452.6 ± 3.1	84.30 ± 2.13	7464 ± 153	0.1033 ± 0.0004	12486 ± 45	-46.1 ± 1.2	12419 ± 45
7249	35.1	1491.8 ± 3.1	343.53 ± 6.98		0.1042 ± 0.0003	12570 ± 45	-43.3 ± 1.1	12498 ± 46
7250	38.4	1707.5 ± 3.3	246.23 ± 5.09	12045 ± 251	0.1053 ± 0.0003	12674 ± 44	-45.7 ± 1.2	12674 ± 45
7251	41.3	1577.9 ± 3.5	242.38 ± 5.00	11309 ± 235	0.1054 ± 0.0004	12874 ± 51	-54.8 ± 1.3	12804 ± 51
7252	44.8	1323.3 ± 2.8	355.62 ± 7.22	6725 ± 138	0.1117 ± 0.0004	13119 ± 54	-33.5 ± 1.2	13046 ± 54
7254a	50.8	1708.4 ± 3.3	974.93 ± 19.61	3228 ± 65	0.1117 ± 0.0003	13221 ± 46	-21.8 ± 1.3	13139 ± 47
7254b	50.8	1701.9 ± 4.3	966.11 ± 19.40	3249 ± 66	0.1118 ± 0.0004	13230 ± 55	-21.4 ± 1.9	13148 ± 56
7255	54.4	1378.2 ± 2.0	933.63 ± 18.90	2731 ± 55	0.1122 ± 0.0004	13348 ± 36	-26.7 ± 1.1	13263 ± 38
7256	58.0	1590.3 ± 3.1	3613.65 ± 72.72	818 ± 17	0.1127 ± 0.0004	13498 ± 49	-32.3 ± 1.3	13365 ± 69
7257a	59.0	1637.6 ± 4.3	119.92 ± 2.43	25425 ± 522	0.1125 ± 0.0005	13482 ± 65	-29.7 ± 1.9	13405 ± 65
7257b	59.0	1644.6 ± 4.4	117.99 ± 2.38	25855 ± 526	0.1125 ± 0.0004	13445 ± 60	-30.8 ± 1.9	13378 ± 60
7258	61.4	1414.1 ± 2.7	85.28 ± 1.72	31154 ± 633	0.1125 ± 0.0003	13455 ± 46	-25.7 ± 1.4	13488 ± 46
7259	64.3	1487.8 ± 3.0	396.75 ± 7.97	7075 ± 143	0.1144 ± 0.0004	13649 ± 50	-28.0 ± 1.4	13576 ± 51
7263	71.1	1578.4 ± 3.8	707.91 ± 14.22	4270 ± 86	0.1161 ± 0.0004	13963 ± 56	-34.3 ± 1.7	13884 ± 56
U, Th. combined								
UHEI								
7811	120.6	2001.1 ± 0.1	15.04 ± 0.09	54596 ± 363	0.1333 ± 0.0004	16058 ± 55	-25.9 ± 0.7	15992 ± 57
7812	129.0	1993.0 ± 0.1	668.86 ± 1.28	1251 ± 4	0.1365 ± 0.0003	16643 ± 41	-35.2 ± 0.4	16567 ± 43
7813	136.8	1929.2 ± 0.1	124.71 ± 0.28	6538 ± 21	0.1375 ± 0.0003	17205 ± 46	-58.1 ± 0.3	17137 ± 45
7815	153.2	1883.0 ± 0.1	3731.58 ± 7.99	224 ± 1	0.1445 ± 0.0004	18902 ± 48	-93.4 ± 0.4	18772.8 ± 59
7816	162.0	2182.4 ± 0.1	393.08 ± 1.00	2619 ± 9	0.1537 ± 0.0004	19847 ± 51	-77.4 ± 0.3	19775 ± 51
7818	178.7	1732.0 ± 0.1	1892.76 ± 3.46	452 ± 1	0.1610 ± 0.0004	21724 ± 56	-111.3 ± 0.4	21623 ± 58
7819	186.3	2377.4 ± 0.1	658.89 ± 1.66	1803 ± 7	0.1631 ± 0.0004	22133 ± 66	-114.7 ± 0.3	22058 ± 65
7820	193.0	2308.2 ± 0.1	864.86 ± 1.57	1483 ± 4	0.1814 ± 0.0004	23836 ± 55	-77.4 ± 0.3	23758 ± 55
7821	199.4	1517.3 ± 0.1	1124.13 ± 2.27	770 ± 2	0.1863 ± 0.0004	24620 ± 53	-80.0 ± 0.5	24530 ± 54
7822	207.4	2019.8 ± 0.1	1322.06 ± 2.32	897 ± 2	0.1915 ± 0.0004	25482 ± 60	-83.0 ± 0.3	25396 ± 59
7823	215.0	1871.4 ± 0.1	4551.26 ± 7.09	247 ± 1	0.1957 ± 0.0005	26280 ± 61	-88.6 ± 0.3	26137 ± 73
7824	222.4	1856.2 ± 0.1	2104.25 ± 35.73	56 ± 0	0.2051 ± 0.0013	27531 ± 59	-82.9 ± 0.4	27019 ± 196
7825	44.7	1331.6 ± 0.0	502.70 ± 0.88	884 ± 3	0.1088 ± 0.0003	12982 ± 32	-30.0 ± 0.4	12905 ± 34
U, Th. separated								
7801	11.8	922.6 ± 0.1	0.69 ± 0.01	393 ± 4	0.0963 ± 0.0007	11755 ± 94	-57.4 ± 0.4	11666 ± 97
7802	12.8	1442.9 ± 0.1	0.25 ± 0.01	1721 ± 10	0.0982 ± 0.0004	11889 ± 51	-49.3 ± 0.9	11817 ± 50
7803	43.0	1488.3 ± 0.1	0.68 ± 0.01	722 ± 3	0.1084 ± 0.0004	12930 ± 53	-29.8 ± 0.6	12851 ± 54
7804	47.1	1727.1 ± 0.1	0.17 ± 0.01	3562 ± 14	0.1115 ± 0.0003	13089 ± 43	-12.8 ± 0.8	13020 ± 44
7805	75.2	1891.6 ± 0.3	0.15 ± 0.01	4530 ± 17	0.1168 ± 0.0003	14069 ± 41	-34.2 ± 0.8	14001 ± 42
7806	82.9	1878.8 ± 0.1	0.35 ± 0.01	1963 ± 6	0.1207 ± 0.0003	14336 ± 36	-19.5 ± 0.6	14264 ± 35
7807	92.5	2203.4 ± 0.1	0.19 ± 0.01	4469 ± 15	0.1228 ± 0.0003	14737 ± 38	-28.0 ± 0.3	14669 ± 37
7808	98.9	2141.3 ± 0.2	0.39 ± 0.01	2115 ± 7	0.1257 ± 0.0003	15090 ± 40	-27.0 ± 0.3	15019 ± 41
7809	105.6	2010.6 ± 0.1	0.59 ± 0.01	1350 ± 5	0.1302 ± 0.0004	15447 ± 46	-13.3 ± 0.3	15372 ± 47
7810	111.3	2304.8 ± 0.3	0.16 ± 0.01	5866 ± 25	0.1313 ± 0.0004	15642 ± 49	-16.3 ± 0.3	15574 ± 49

dft: distance from top. All uncertainties are 2σ. [a](^{230}Th/^{238}U) $= 1 - e^{-\lambda_{230}T} + (\delta^{234}\text{U}_{meas}/1000)[\lambda_{230}/(\lambda_{230} - \lambda_{234})][1 - e^{-(\lambda_{230}-\lambda_{234})T}]$, where T is age in years. $\lambda_{238} = 1.551 \cdot 10^{-10}$ a^{-1} (Jaffey et al. [1971]), UHEI: $\lambda_{230} = 9.1577 \cdot 10^{-6}$ a^{-1}, $\lambda_{234} = 2.8263 \cdot 10^{-6}$ a^{-1} (Cheng et al. [2000b]), UoM: $\lambda_{230} = 9.1705 \cdot 10^{-6}$ a^{-1}, $\lambda_{234} = 2.8221 \cdot 10^{-6}$ a^{-1} (Cheng et al. [2013]). [b]Years before measurement and without detrital Th correction. [c]δ^{234}U $= [(^{234}\text{U}/^{238}\text{U}) - 1] \cdot 1000$, $\delta^{234}\text{U}_{initial} = \delta^{234}\text{U}_{initial} e^{\lambda_{234}T}$. [d]Corrected ^{230}Th ages assume the initial ^{230}Th/^{232}Th atomic ratio of $4.4 \pm 2.2 \cdot 10^{-6}$. Those are the values for a material at secular equilibrium, with the bulk earth ^{232}Th/^{238}U value of 3.8. The errors are arbitrarily assumed to be 50%. [e]BP stands for "Before Present" where "Present" is defined as 1950 A.D.

Table B.3: U-series dating results of corals from core GeoB20933-1.

Sample ID	Depth (cm dft)	[238U] (ppb)	[232Th] (ppt)	(230Th/232Th) (activity)	(230Th/238U)[a] (activity)	230Th Age[b] (a) (uncorrected)	$\delta^{234}U^c_{initial}$ (corrected)	230Th Age[d,e] (a BP) (corrected)
GeoB20933-1								
Batch A								
7919 A	34.0	4142.8 ± 0.1	219.3 ± 0.4	1804 ± 7	0.0313 ± 0.0001	3027 ± 11	146.6 ± 0.3	2948 ± 12
7920 A	79.5	3336.5 ± 0.1	179.8 ± 0.4	2147 ± 8	0.0380 ± 0.0001	3682 ± 13	147.0 ± 0.4	3603 ± 14
7921 A	114.5	3681.8 ± 0.1	751.1 ± 1.4	967 ± 3	0.0648 ± 0.0002	6356 ± 19	148.1 ± 0.5	6239 ± 32
7922 A	151.0	3961.0 ± 0.1	186.4 ± 0.3	4510 ± 13	0.0697 ± 0.0002	6860 ± 16	146.7 ± 0.4	6782 ± 17
7923 A	179.5	2902.0 ± 0.1	947.6 ± 1.7	711 ± 2	0.0761 ± 0.0002	7505 ± 22	148.0 ± 0.5	7358 ± 47
7924 A	204.5	4209.8 ± 1.2	301.4 ± 0.7	4002 ± 13	0.0940 ± 0.0002	9362 ± 23	146.3 ± 1.1	9279 ± 24
7925 A	208.5	4288.9 ± 0.1	1439.7 ± 2.6	864 ± 3	0.0952 ± 0.0002	9480 ± 24	147.2 ± 0.5	9330 ± 49
7926 A	249.0	3830.9 ± 0.1	1624.4 ± 2.9	719 ± 2	0.1000 ± 0.0002	9980 ± 25	147.2 ± 0.5	9808 ± 59
7934 A	522.5	3260.2 ± 0.1	582.5 ± 1.2	2290 ± 8	0.1342 ± 0.0004	13637 ± 39	146.0 ± 0.6	13526 ± 45
7940 A	708.0	3668.5 ± 0.1	2321.3 ± 4.2	1196 ± 3	0.2485 ± 0.0005	26944 ± 64	141.9 ± 0.5	26720 ± 102
7949 A	937.0	3465.0 ± 0.1	857.1 ± 1.5	3679 ± 10	0.2998 ± 0.0006	33610 ± 86	138.2 ± 0.8	33481 ± 92
Batch B								
7919 B	34.0	4143.6 ± 0.1	209.1 ± 0.3	1894 ± 5	0.0313 ± 0.0001	3020 ± 9	147.7 ± 1.7	2941 ± 11
7920 B	79.5	3340.5 ± 0.1	140.7 ± 0.2	2746 ± 8	0.0379 ± 0.0001	3669 ± 11	148.0 ± 1.6	3592 ± 12
7921 B	114.5	3682.8 ± 0.1	633.8 ± 0.6	1147 ± 2	0.0646 ± 0.0001	6325 ± 15	149.1 ± 1.4	6216 ± 26
7922 B	151.0	3960.4 ± 0.1	172.9 ± 0.2	4874 ± 11	0.0696 ± 0.0001	6833 ± 16	148.9 ± 1.5	6757 ± 17
7923 B	179.5	2907.3 ± 0.1	853.6 ± 0.8	789 ± 2	0.0757 ± 0.0001	7451 ± 15	148.7 ± 0.4	7312 ± 40
7924 B	204.5	4205.0 ± 0.1	278.0 ± 0.4	4369 ± 9	0.0943 ± 0.0002	9383 ± 17	147.1 ± 0.7	9300 ± 19
7925 B	208.5	4289.7 ± 0.1	1276.9 ± 1.1	980 ± 2	0.0951 ± 0.0001	9457 ± 19	148.6 ± 1.5	9317 ± 42
7926 B	249.0	3832.8 ± 0.1	1476.4 ± 1.2	795 ± 1	0.1002 ± 0.0002	10001 ± 20	147.4 ± 1.4	9839 ± 51
7934 B	522.5	3266.4 ± 0.1	527.7 ± 0.5	2535 ± 5	0.1342 ± 0.0002	13632 ± 35	148.3 ± 2.2	13525 ± 39
7940 B	708.0	3666.7 ± 0.1	2224.7 ± 1.8	1257 ± 2	0.2486 ± 0.0003	26892 ± 80	144.5 ± 2.8	26675 ± 110
7949 B	937.0	3455.4 ± 0.1	799.8 ± 0.9	3967 ± 7	0.3004 ± 0.0004	33686 ± 50	138.5 ± 0.4	33562 ± 56

dft: distance from top. All uncertainties are 2σ. [a] $(^{230}\text{Th}/^{238}\text{U}) = 1 - e^{-\lambda_{230}T} + (\delta^{234}U_{meas}/1000)[\lambda_{230}/(\lambda_{230} - \lambda_{234})][1 - e^{-(\lambda_{230}-\lambda_{234})T}]$, where T is age in years. $\lambda_{238} = 1.551 \cdot 10^{-10}$ a^{-1} (Jaffey et al. [1971]), $\lambda_{230} = 9.1577 \cdot 10^{-6}$ a^{-1}, $\lambda_{234} = 2.8263 \cdot 10^{-6}$ a^{-1} (Cheng et al. [2000b]). [b] Years before measurement and without correction for the initial ^{230}Th/^{232}Th ratio. [c] $\delta^{234}U_{initial}$ was calculated based on ^{230}Th age (T), i.e., $\delta^{234}U_{initial} = \delta^{234}U_{initial}e^{\lambda_{234}T}$. [d]Corrected ^{230}Th ages according to Cheng et al. [2000a] and with an assumed initial ^{230}Th/^{232}Th ratio of 8 ± 4. The errors are arbitrarily assumed to be 50 %. [e] BP stands for "Before Present" where "Present" is defined as 1950 A.D.

C Matlab source code

C.1 Starting script

```matlab
1  global data_root_folder
2
3  if ¬exist('is_gui') % start of skript
4      clear all
5      close all
6      clc
7      folder = ...
           'C:\Users\bwpc\bwSyncAndShare\Arbeit\matlab\ratios_2.7_gui'; ...
           % directory of matlab routines
8      data_root_folder = folder; % directory of data
9      cd(folder)
10     addpath(genpath(folder))
11 end
12
13 format long
14 warning('off')
15
16
17
18
19 %% initializing constants
20 run params.m
21
22 %% read yhas file: hydride - abundance sensitivity
23 run yhas_uran.m
24 run yhas_thorium.m
25
26 if ¬exist('is_gui')
27     blk      = 1.0; % blk = 0 if already subtracted in measurement ...
           sequence, else blk = 1.0
28     yield_U  = 1.0;
29     yield_Th = 1.0;
30     gain13   = 1.0; % gain13 = 1.0 if measured on 10, 11, and 12 ...
           Ohm cups, else tuning
31 end
32
33 %% tailing
34 if exist('dummyc','var')== 1 && exist('dummy','var')==1
35     tail_mat_cup = [fc(229), fc(230), fc(232), fc(233), fc(234), ...
           fc(235), fc(236), fc(237)]./(yield_U.*cps.*u238tail_c); % ...
           tailing U-238 on cup
```

```matlab
36      tail_mat       = [f(229), f(230), f(232), f(233), f(234), f(235), ...
            f(236), f(237)]./(yield_U.*cps.*u238tail); % tailing U-238 ...
            on SEM/RPQ
37      for j=1:length(tail_mat)
38          if tail_mat(j) < 0
39          tail_mat(j) = 0;
40          end
41      end
42
43      for j=1:length(tail_mat_cup)
44          if tail_mat_cup(j) < 0
45          tail_mat_cup(j) = 0;
46          end
47      end
48      RPQ_Norm_Uran = tail_mat.*cps % tailing normalized to 1 V signal
49      IC5_Norm_Uran = tail_mat_cup.*cps
50
51      if exist('is_gui')
52          factors = get(handles.table_factors,'data');
53          factors{1,3} = f(237)./(yield_U.*cps.*u238tail);
54          factors{1,4} = fc(237)./(yield_U.*cps.*u238tail_c);
55          set(handles.table_factors, 'data', factors);
56          set(handles.table_tail_u, 'data', [tail_mat' tail_mat_cup']');
57      end
58
59
60  elseif exist('dummyc','var')== 1 && exist('dummy','var')==0
61      tail_mat_cup = [fc(229), fc(230), fc(232), fc(233), fc(234), ...
            fc(235), fc(236), fc(237)]./(yield_U.*cps.*u238tail_c); % ...
            tailing U-238 on cup
62
63       for j=1:length(tail_mat_cup)
64          if tail_mat_cup(j) < 0
65          tail_mat_cup(j) = 0
66          end
67       end
68      IC5_Norm_Uran = tail_mat_cup.*cps
69      if exist('is_gui')
70        factors = get(handles.table_factors,'data');
71        factors{1,4} = fc(237)./(yield_U.*cps.*u238tail_c);
72        set(handles.table_factors, 'data', factors);
73        set(handles.table_tail_u, 'data', [tail_mat_cup']');
74      end
75
76  else
77          tail_mat       = [f(229), f(230), f(232), f(233), f(234), ...
                f(235), f(236), f(237)]./(yield_U.*cps.*u238tail); % ...
                tailing U-238 on SEM/RPQ
78
79          for j=1:length(tail_mat)
80              if tail_mat(j) < 0
81              tail_mat(j) = 0
```

```matlab
82              end
83          end
84              RPQ_Norm_Uran = tail_mat.*cps
85
86          if exist('is_gui')
87              factors = get(handles.table_factors,'data');
88              factors{1,3} = f(237)./(yield_U.*cps.*u238tail);
89              set(handles.table_factors, 'data', factors);
90              set(handles.table_tail_u, 'data', [tail_mat']');
91          end
92
93  end
94
95  if exist('dummyct','var') == 1 && exist('dummyt','var') == 1
96      tail_mat_th_cup = [gc(229), ...
            gc(230)]./(yield_Th.*cps.*th232tail_c); % tailing Th-232 on cup
97      tail_mat_th = [g(229), g(230)]./(yield_Th.*cps.*th232tail); % ...
            tailing Th-232 on SEM/RPQ
98      for j=1:length(tail_mat_th)
99          if tail_mat_th(j) < 0
100             tail_mat_th(j) = 0;
101         end
102     end
103
104     for j=1:length(tail_mat_th_cup)
105         if tail_mat_th_cup(j) < 0
106             tail_mat_th_cup(j) = 0;
107         end
108     end
109     RPQ_Norm_Th = tail_mat_th.*cps
110     IC5_Norm_Th = tail_mat_th_cup.*cps
111     if exist('is_gui')
112         set(handles.table_tail_th, 'data', [tail_mat_th' ...
                tail_mat_th_cup']');
113     end
114
115
116 elseif exist('dummyct','var') == 1 && exist('dummyt','var') == 0
117     tail_mat_th_cup = [gc(229), gc(230)]./(yield_Th.*cps.*th232tail_c);
118     for j=1:length(tail_mat_th_cup)
119         if tail_mat_th_cup(j) < 0
120             tail_mat_th_cup(j) = 0;
121         end
122     end
123     IC5_Norm_Th = tail_mat_th_cup.*cps
124     if exist('is_gui')
125         set(handles.table_tail_th, 'data', [tail_mat_th_cup']');
126     end
127 else
128     tail_mat_th = [g(229), g(230)]./(yield_Th.*cps.*th232tail);
129     for j=1:length(tail_mat_th)
130         if tail_mat_th(j) < 0
```

```matlab
                   tail_mat_th(j) = 0;
           end
      end
      RPQ_Norm_Th = tail_mat_th.*cps
      if exist('is_gui')
          set(handles.table_tail_th, 'data', [tail_mat_th']');
      end
 end


%% creating tailing excel file
if exist('dummyc','var')== 1 && exist('dummy','var')==1 && ...
      exist('dummyct','var')== 1 && exist('dummyt','var')==1

    headers_tail = {
        'Th-229'
        'Th-230'
        'Th-232'
        'U-233'
        'U-234'
        'U-235'
        'U-236'
        'U-237'
        'Th-229'
        'Th-230'}';

    tail_names = {
        'Tailing IC + RPQ'
        'Tailing IC'
        'IC/IC+RPQ'};

    a_tail = [tail_mat tail_mat_th];
    b_tail = [tail_mat_cup tail_mat_th_cup];
    c_tail = [tail_mat_cup./tail_mat tail_mat_th_cup./tail_mat_th];
    dummytailm = [
        a_tail
        b_tail
        c_tail];

    dummytail  = num2cell(dummytailm);
    MATRIXtail = [{''} headers_tail; tail_names dummytail];
    xlswrite('Tailing.xlsx', MATRIXtail);
end
%% begin data correction
run cupfast.m

%% corrected data in excel file
headers = { 'Ratio 233/236'
    'Error (%)'
    'Ratio 235/238'
    'Error (%)'
    'Ratio 235/236'
```

```
182    'Error (%)'
183    'Ratio 234/233'
184    'Error (%)'
185    'Ratio 234/235'
186    'Error (%)'
187    'Ratio 234/238'
188    'Error (%)'
189    'Ratio 230/229'
190    'Error (%)'
191    'Ratio 229/232'
192    'Error (%)'
193    'Ratio 230/232'
194    'Error (%)'}';
195
196
197 dummy11 = matrix_ratios;
198 dummy2  = num2cell(dummy11);
199 MATRIX  = [{''} headers; names_data' dummy2];
200 delete('Ratios.xlsx');
201 xlswrite('Ratios.xlsx', MATRIX);
202
203
204 if exist('is_gui')
205 set(handles.table_results, 'data',[names_data' dummy2 num2cell(AU)]);
206 end
```

C.2 Initializing parameters

```
1  %% spike impurities
2  R34_33 = 0.002324; % ratio spike 234/233 0.002324 +- 0.000048
3  R35_33 = 0.005066; % ratio spike 235/233 0.005066 +- 0.000110
4  R30_29 = 4.8e-5;   % ratio spike 230/229 0.000048 +- 0.000007
5
6
7  %% constants
8  mf48 = 1.336402435064349; % mass fractionation 234/238, i.e. ...
       ln(234/238)/ln(235/238) exponential law
9  mf36 = 1.008202776684838; % mass fractionation 233/236
10 mf56 = 0.334493224630051; % mass fractionation 235/236
11 mf68 = 0.665506775369946; % mass fractionation 236/238
12 mf90 = 0.343185870411394; % mass fractionation 229/230
13 mf92 = 1.025840620457897; % mass fractionation 229/232
14
15 mf43 = -0.337307116990441;
16 mf45 = 0.336402435064353;
17 mf09 = -0.343185870411394;
18 mf29 = -1.025840620457897;
19 mf34 = 0.337307116990439;
20 mf58 = 1;
21 mf02 = 0.682654750046506;
```

106

```
22
23
24  NA   = 6.02214129e23; % Avogadro constant in 1/mol
25  NR85 = 137.881;       % natural ratio U238/U235
26  cps  = 62500000;      % 1/(1e11*1.602e-19) counts/1V @ R = 10e11 Ohm
27
28  lambda234 = 2.8263e-06;  % decay constant U234, Cheng et. al. 2000
29  lambda238 = 1.55125e-10; % decay constant U238
30  lambda230 = 9.1577e-06;  % decay constant Th230
31  lambda232 = 4.9475e-11;  % decay constant Th232
```

C.3 Hydride and abundance sensitivity ^{238}U

```
1   folderyu = strcat(data_root_folder, '\yhas_u');
2   listyu  = dir(fullfile(folderyu,'*.exp'));
3   namesyu = {listyu.name};
4   cd(folderyu)
5
6       x_axis_tail_u        = [228.5, 230.5, 231.5, 233.5, 236.5, ...
            236.7, 237.05, 237.5];   % half-masses tailing SEM/RPQ
7       x_axis_tail_u_cup    = [228.5, 230.5, 231.5, 233.5, 236.5, ...
            236.7, 237.05, 237.5]; % half-masses tailing cup
8
9   xxx   = linspace(228.5,237.5,200);
10
11  for i = 1:length(namesyu)
12
13      aa=readtable(namesyu{i},'Delimiter','\t','FileType','text');
14      raw       = table2cell(aa);
15      [d,e]     = size(raw);
16      peakstrc  = 'C(C)';
17      [rc, cc]  = find(strcmp(raw,peakstrc));
18      peakstr   = 'Mean';
19      [row, col] = find(strcmp(raw,peakstr));
20
21      if length(cc) == 0
22      dummyc(i,:)   = str2double(raw(row,col+1:col+8));
23      u238tailc(:,i) = str2double(raw(row,col+10));
24      uhc(:,i)      = ...
            str2double(raw(row,col+9))./(str2double(raw(row,col+10)).*cps);
25
26      UH_plus_c  = mean(uhc(uhc≠0));
27      u238tail_c = mean(u238tailc(u238tailc≠0));
28      dummyc(¬any(dummyc,2),:) = [];
29
30      aac = mean(dummyc(:,1:length(dummyc)),1);
31
32      else
33
34      dummy(i,:)    = str2double(raw(row,col+1:col+8));
```

```matlab
35         u238tail(:,i) =str2double(raw(row,col+10));
36         uh(:,i)        = ...
               str2double(raw(row,col+9))./(str2double(raw(row,col+10)).*cps);
37
38         UH_plus        = mean(uh(uh≠0));
39         u238tail       = mean(u238tail(u238tail≠0));
40         dummy(¬any(dummy,2),:) = [];
41
42         aas = mean(dummy(:,1:length(dummy)),1);
43
44     end
45 end
46
47 if exist('is_gui')
48     cla(handles.axes_uran)
49     axes(handles.axes_uran)
50 else
51     figure
52 end
53
54 set(gca,'FontSize',12)
55
56 if exist('dummyc','var') == 1 && exist('dummy','var') == 1
57
58     f  = fit(x_axis_tail_u(1:(length(x_axis_tail_u)))',...
59         aas(1:(length(aas)))','pchipinterp'); % pchipinterp on full ...
               masses on SEM/RPQ
60     fc = fit(x_axis_tail_u_cup(1:(length(x_axis_tail_u_cup)))',...
61         aac(1:(length(aac)))','pchipinterp'); % pchipinterp on full ...
               masses on cup
62     plot(xxx,f(xxx),'LineWidth',3)
63     hold on
64     plot(x_axis_tail_u,aas,'og')
65     hold on
66     plot(xxx,fc(xxx),'LineWidth',3,'Color','r')
67     hold on
68     plot(x_axis_tail_u_cup,aac,'ok')
69     legend('Tailing IC + RPQ','measured','Tailing IC','measured')
70     ylim([0,400])
71     xlim([228,237.5])
72     title('Tailing U-238')
73     grid on
74     UH_plus = (UH_plus_c+UH_plus)./2;
75
76 elseif exist('dummyc','var') == 1 && exist('dummy','var') == 0
77     fc = fit(x_axis_tail_u_cup(1:(length(x_axis_tail_u_cup)))',...
78         aac(1:(length(aac)))','pchipinterp'); % pchipinterp on full ...
               masses on cup
79     plot(xxx,fc(xxx),'LineWidth',3,'Color','r')
80     hold on
81     plot(x_axis_tail_u_cup,aac,'ok')
82     legend('Tailing IC','measured')
```

```matlab
83      ylim([0,400])
84      xlim([228,237.5])
85      title('Tailing U-238')
86      grid on
87      UH_plus = UH_plus_c;
88
89  else
90
91      f = fit(x_axis_tail_u(1:(length(x_axis_tail_u)))',...
92          aas(1:(length(aas)))','pchipinterp'); % pchipinterp on full ...
                masses on SEM/RPQ
93      plot(xxx,f(xxx),'LineWidth',3)
94      hold on
95      plot(x_axis_tail_u,aas,'og')
96      hold on
97      ylim([0,400])
98      xlim([228,237.5])
99      title('Tailing U-238')
100     grid on
101     legend('Tailing IC + RPQ','measured')
102     UH_plus = UH_plus;
103 end
104
105 if exist('is_gui')
106     factors = get(handles.table_factors,'data');
107     factors{1,1} = UH_plus;
108     set(handles.table_factors, 'data', factors);
109 end
110
111 cd ..
```

C.4 Hydride and abundance sensitivity ^{232}Th

```matlab
1  format long
2  folderyth = strcat(data_root_folder, '\yhas_th');
3  listyth  = dir(fullfile(folderyth,'*.exp')); % alle yhas in einen ...
       Ordner als exp Datei
4  namesyth  = {listyth.name};
5
6      x_axis_tail_th        = [227.5 228.5 229.5 230.5 231.5]; % ...
           half-masses tailing SEM/RPQ
7      x_axis_tail_th_cup    = [227.5 228.5 229.5 230.5 231.5]; % ...
           half-masses tailing cup
8  cd(folderyth)
9
10 for i = 1:length(namesyth) % read yhas data
11
12     aa=readtable(namesyth{i},'Delimiter','\t','FileType','text');
13     raw          = table2cell(aa);
14     [d,e]        = size(raw);
```

```matlab
    peakstct      = 'IC2';
    [rct, cct]    = find(strcmp(raw,peakstct));
    peakstrt      = 'Mean';
    [rowt, colt] = find(strcmp(raw,peakstrt));

    if length(cct) == 0

    dummyt(i,:)     = str2double(raw(rowt,colt+1:colt+5));
    th232tail(:,i) = str2double(raw(rowt,colt+6));
    thh(:,i)        = ...
        str2double(raw(rowt,colt+7))./(str2double(raw(rowt,colt+6)).*cps);

    ThH_plus        = mean(thh(thh≠0));
    th232tail        = mean(th232tail(th232tail≠0));
    dummyt(¬any(dummyt,2),:) = [];

    aats = mean(dummyt(:,1:length(dummyt)),1);

    else

    dummyct(i,:)     = str2double(raw(rowt,colt+1:colt+5));
    th232tailc(:,i) =str2double(raw(rowt,colt+6));
    thhc(:,i)        = ...
        str2double(raw(rowt,colt+7))./(str2double(raw(rowt,colt+6)).*cps);

    ThH_plus_c  = mean(thhc(thhc≠0));
    th232tail_c = mean(th232tailc(th232tailc≠0));
    dummyct(¬any(dummyct,2),:) = [];

    aac = mean(dummyct(:,1:length(dummyct)),1);
    end
end


if exist('is_gui')
    cla(handles.axes_thorium)
    axes(handles.axes_thorium)
else
    figure
end

set(gca,'FontSize',12)

if exist('dummyct','var') == 1 && exist('dummyt','var') == 1

    g = fit(x_axis_tail_th(1:(length(x_axis_tail_th)))',...
        aats(1:(length(aats)))','pchipinterp'); % pchipinterp on ...
            full masses on SEM/RPQ
    gc = fit(x_axis_tail_th_cup(1:(length(x_axis_tail_th_cup)))',...
        aac(1:(length(aac)))','pchipinterp'); % pchipinterp on full ...
            masses on cup
    plot(xxx,g(xxx),'LineWidth',3)
```

110

```matlab
63        hold on
64        plot(x_axis_tail_th,aats,'og');
65        hold on
66        plot(xxx,gc(xxx),'LineWidth',3,'Color','r');
67        hold on
68        plot(x_axis_tail_th_cup,aac,'ok')
69        legend('Tailing IC + RPQ','measured','Tailing IC','measured')
70        xlim([228, 231.8])
71        title('Tailing Th-232')
72        ylim([0, 400]);
73        grid on
74        ThH_plus = (ThH_plus_c+ThH_plus)./2;
75
76  elseif exist('dummyct','var') == 1 && exist('dummyt','var') == 0
77
78        gc = fit(x_axis_tail_th_cup(1:(length(x_axis_tail_th_cup)))',...
79            aac(1:(length(aac)))','pchipinterp'); % pchipinterp on full ...
                 masses on cup
80        plot(xxx,gc(xxx),'LineWidth',3,'Color','r');
81        hold on
82        plot(x_axis_tail_th_cup,aac,'ok');
83        legend('Tailing IC','measured')
84        xlim([228, 231.8])
85        title('Tailing Th-232')
86        ylim([0, 400]);
87        grid on
88
89        ThH_plus = ThH_plus_c;
90
91  else
92
93        g = fit(x_axis_tail_th(1:(length(x_axis_tail_th)))',...
94            aats(1:(length(aats)))','pchipinterp'); % pchipinterp on ...
                 full masses on SEM/RPQ
95        plot(xxx,g(xxx),'LineWidth',3);
96        hold on
97        plot(x_axis_tail_th,aats,'og');
98        xlim([228, 231.8])
99        title('Tailing Th-232')
100       ylim([0, 400]);
101       grid on
102       legend('Tailing IC + RPQ','measured')
103       ThH_plus = ThH_plus;
104
105 end
106
107 if exist('is_gui')
108     factors = get(handles.table_factors,'data');
109     factors{1,2} = ThH_plus;
110     set(handles.table_factors, 'data', factors);
111 end
112
```

```
113
114 cd ..
```

C.5 Blank correction and calculation of ratios

```
1  %% blank correction
2  folder_blank  = strcat(data_root_folder, '\blank');
3  list_blank    = dir(fullfile(folder_blank,'*.exp'));
4  names_blank   = {list_blank.name};
5
6  folder_data   = strcat(data_root_folder, '\data');
7  list_data     = dir(fullfile(folder_data,'*.exp'));
8  names_data    = {list_data.name};
9
10 headers = {
11         'U-233'
12         'U-234'
13         'U-235'
14         'U-236'
15         'U-238'
16         'Th-230'
17         'Th-232'
18         'Th-229'}';
19
20 %% process blank correction, read blank file
21 if blk == 1.0
22     for k = 1:length(names_blank)
23         cd(folder_blank)
24         bb ...
               =readtable(names_blank{k},'Delimiter','\t','FileType','text');
25         raw = table2cell(bb);
26
27         peakstra = '1:233U';
28         peakstrb = 'Cup';
29         peakstrc = '2:230Th';
30         [rowa, cola] = find(strcmp(raw,peakstra));
31         [rowpb, colpb] = find(strcmp(raw,peakstrb));
32         [rowpc, colpc] = find(strcmp(raw,peakstrc));
33
34         cd ..
35
36         datablk = str2double(raw(rowa+1:rowpb-1,colpb+1:colpb+5));
37         datablk = [datablk,  ...
               str2double(raw(rowpc+1:rowpb-1,colpc:colpc+2))];
38         Z = bsxfun(@lt, mean(datablk) + 0.5*std(datablk), datablk) ...
               | bsxfun(@gt, mean(datablk) - 2*std(datablk), datablk);
39         datablk(Z) = nan;
40
41         [nn,mm] = size(datablk);
42         for n=1:nn
```

112

```matlab
43              for m = 1:mm
44                  if datablk(n,m) < 0
45                      datablk(n,m) = 0;
46                  end
47              end
48          end
49
50          datablkm(:,k) = nanmean(datablk);
51      end
52
53      dummymm     = datablkm';
54      dummy2mm    = num2cell(dummymm);
55      MATRIXblank = [{''} headers; names_blank' dummy2mm];
56      delete('PrBlank.xlsx');
57      xlswrite('PrBlank.xlsx', MATRIXblank);
58
59  else
60
61      datablkm    = zeros(8,length(names_data));
62      dummymm     = datablkm';
63      dummy2mm    = num2cell(dummymm);
64      MATRIXblank = [{''} headers; names_data' dummy2mm];
65      delete('PrBlank.xlsx');
66      xlswrite('PrBlank.xlsx', MATRIXblank);   %% MATRIX in Excel
67  end
68
69  %% data division into different measurement methods and data correction
70  for i = 1:length(names_data)
71
72      cd(folder_data)
73      aa=readtable(names_data{i},'Delimiter','\t','FileType','text');
74      raw = table2cell(aa);
75
76      [d,e]           = size(raw);
77      peakst3         = 'C(C)';
78      peakst4         = 'C';
79      [r3, c3]        = find(strcmp(raw,peakst3));
80      [r4, c4]        = find(strcmp(raw,peakst4));
81      peakstr         = '1:233U';
82      peakstr2        = 'Cup';
83      [rowp, colp]    = find(strcmp(raw,peakstr));
84      [rowp2, colp2]  = find(strcmp(raw,peakstr2));
85      cd ..
86      data = str2double(raw(rowp+1:rowp2-1,colp:colp+8));
87
88      switch length(c3)
89          case 3
90              run post_904IC.m       % measurement method: 234, 230, ...
91                  and 229 on SEM/RPQ
92          case 2
93              run post_90IC.m        % measurement method: 230 and ...
94                  229 on SEM/RPQ
```

```
93          case 1
94              run post_0IC.m          % measurement method: 230 on SEM/RPQ
95          otherwise
96              run post_allcup.m       % measurement method: all ...
                    isotopes on cup
97      end
98
99      matrix_ratios(i,:) = [R36_
100     errRel36*100
101     R58u_
102     errRel58u*100
103     R56_
104     errRel56*100
105     R43_
106     errRel43*100
107     R45_
108     errRel45*100
109     R48_
110     errRel48*100
111     R09_
112     errRel09*100
113     R92_
114     errRel92*100
115     R02_
116     errRel02*100];
117
118 AU(i,:) = [R48_.*lambda234./lambda238
119          errRel48.*100];
120
121 end
```

C.5.1 Measurement method: ^{234}U, ^{230}Th, ^{229}Th on SEM with RPQ

```
1  % tail_mat(_th)/_cup): tailing correction U/Th, SEM+RPQ/cup, ...
       UH_plus/ThH_plus: Hydride correction,
2  % blk: process blank correction, yield_U(_Th)/gain13: yield/gain13 ...
       correction
3
4  data33    = data(:,1)-data(:,5).*tail_mat_cup(4) - ...
       data(:,8).*ThH_plus - blk .*datablkm(1,i); % U233
5  err_data33 = 2*std(data33)./sqrt(length(data33));
6  abs_data33 = mean(data33);
7
8  data34    = data(:,2)-UH_plus.*data33.*cps*yield_U - ...
       data33*R34_33.*cps*yield_U-data(:,5).*tail_mat(5).*cps*yield_U ...
       - blk .*datablkm(2,i); % U234
9  err_data34 = 2*std(data34)./sqrt(length(data34));
10 abs_data34 = mean(data34);
11
12 data35    = (data(:,3)-(data(:,2).*UH_plus)./(cps*yield_U)) - ...
```

```matlab
           data33*R35_33-data(:,5).*tail_mat_cup(6) - blk .*datablkm(3,i); ...
           % U235
13 err_data35 = 2*std(data35)./sqrt(length(data35));
14 abs_data35 = mean(data35);
15
16 data36     = ...
           data(:,4)-UH_plus.*data(:,3)-data(:,5).*tail_mat_cup(7) - blk ...
           .*datablkm(4,i);  % U236
17 err_data36 = 2*std(data36)./sqrt(length(data36));
18 abs_data36 = mean(data36);
19
20 data38     = data(:,5)- blk.*datablkm(5,i);  % U238
21 err_data38 = 2*std(data38)./sqrt(length(data38));
22 abs_data38 = mean(data38);
23
24 data29     = data(:,9)-data(:,5).*tail_mat(1).*cps*yield_U - ...
           tail_mat_th(1).*cps.*yield_Th.*data(:,8)- blk .*datablkm(8,i);  ...
           % Th229
25 err_data29 = 2*std(data29)./sqrt(length(data29));
26 abs_data29 = mean(data29);
27
28 data30     = data(:,7)-ThH_plus.*data29 - ...
           data29*R30_29-data(:,5).*tail_mat(2).*cps.*yield_U- ...
           tail_mat_th(2).*cps.*yield_Th.*data(:,8) - blk .*datablkm(6,i); ...
            % Th230 U
29 err_data30 = 2*std(data30)./sqrt(length(data30));
30 abs_data30 = mean(data30);
31
32 data32     = data(:,8)-data(:,5).*tail_mat_cup(3) - blk ...
           .*datablkm(7,i);  % Th232
33 err_data32 = 2*std(data32)./sqrt(length(data32));
34 abs_data32 = mean(data32);
35
36 %% calculating atomic ratios, mass fractionation correction, 2 ...
           sigma outlier test
37 R58d = data35./data38;  % U235/U238 for mass fractionation correction
38
39 R58u = data35./data38;  % U235/U238 for monitoring machine drift
40 [R58u, errR58u, R58u_, errRel58u] = outliertest(R58u); % output: ...
           outlier corrected R58, 2sigma SE, mean, 2sigma relative SE
41
42 R58  = data35./data38.*(1./137.881./R58d).^mf58;  % U235/U238
43 [R58, errR58, R58_, errRel58]     = outliertest(R58);
44
45 R34  = data33./(data34./(cps*yield_U)).*(1./137.881./R58d).^mf34; ...
            % U233/U234
46 [R34, errR34, R34_, errRel34]     = outliertest(R34);
47
48 R56  = data35./data36.*(1./137.881./R58d).^mf56; % U235/U236
49 [R56, errR56, R56_, errRel56]     = outliertest(R56);
50
51 R48  = (data34./(cps*yield_U))./data38.*(1./137.881./R58d).^mf48; ...
```

```
                % U234/U238
52  [R48, errR48, R48_, errRel48]     = outliertest(R48);

53
54  R09  = data30./data29.*(1./137.881./R58d).^mf09; % Th230/Th229
55  [R09, errR09, R09_, errRel09]     = outliertest(R09);

56
57  R29  = data32./(data29./(cps*yield_Th)).*(1./137.881./R58d).^mf29; ...
                % Th232/Th229
58  [R29, errR29, R29_, errRel29]     = outliertest(R29);

59
60  R43  = (data34./(cps*yield_U))./data33.*(1./137.881./R58d).^mf43; ...
                % U233/U234
61  [R43, errR43, R43_, errRel43]     = outliertest(R43);

62
63  R92  = (data29./(cps.*yield_Th))./data32.*(1./137.881./R58d).^mf92; ...
                % Th232/Th229
64  [R92, errR92, R92_, errRel92]     = outliertest(R92);

65
66  R36  = data33./data36.*(1./137.881./R58d).^mf36; % U233/U234
67  [R36, errR36, R36_, errRel36]     = outliertest(R36);

68
69  R45  = (data34./(cps.*yield_U))./data35.*(1./137.881./R58d).^mf45; ...
                % U233/U234
70  [R45, errR45, R45_, errRel45]     = outliertest(R45);

71
72  R02  = (data30./(cps*yield_Th))./data32.*(1./137.881./R58d).^mf02; ...
                % Th230/Th229
73  [R02, errR02, R02_, errRel02]     = outliertest(R02);
```

C.5.2 Measurement method: ^{230}Th, ^{229}Th on SEM with RPQ

```
1  % tail_mat(_th)/_cup): tailing correction U/Th, SEM+RPQ/cup, ...
       UH_plus/ThH_plus: Hydride correction,
2  % blk: process blank correction, yield_U(_Th)/gain13: yield/gain13 ...
       correction

3
4  data33    = data(:,1)-data(:,5).*tail_mat_cup(4)- ...
       data(:,8).*ThH_plus -  blk .*datablkm(1,i); % U233
5  err_data33 = 2*std(data33)./sqrt(length(data33));
6  abs_data33 = mean(data33);

7
8  data34    = gain13.*data(:,2)-UH_plus.*data33 - ...
       data33*R34_33-data(:,5).*tail_mat_cup(5) -  blk ...
       .*datablkm(2,i)./(cps*yield_U); % U234
9  err_data34 = 2*std(data34)./sqrt(length(data34));
10 abs_data34 = mean(data34);

11
12 data35    = (data(:,3)-data(:,2).*UH_plus.*gain13) - ...
       data33*R35_33-data(:,5).*tail_mat_cup(6) -  blk ...
       .*datablkm(3,i); % U235
13 err_data35 = 2*std(data35)./sqrt(length(data35));
```

116

```matlab
14  abs_data35 = mean(data35);

16  data36      = ...
        data(:,4)-UH_plus.*data(:,3)-data(:,5).*tail_mat_cup(7) - blk ...
        .*datablkm(4,i);  % U236
17  err_data36 = 2*std(data36)./sqrt(length(data36));
18  abs_data36 = mean(data36);

20  data38      = data(:,5) - blk .*datablkm(5,i);  % U238
21  err_data38 = 2*std(data38)./sqrt(length(data38));
22  abs_data38 = mean(data38);

24  data29      = data(:,9)-data(:,5).*tail_mat(1).*cps*yield_U - ...
        tail_mat_th(1).*cps.*yield_Th.*data(:,8) -  blk ...
        .*datablkm(8,i);  % Th229
25  err_data29 = 2*std(data29)./sqrt(length(data29));
26  abs_data29 = mean(data29);

28  data30      = data(:,7)-ThH_plus.*data29 - ...
        data29*R30_29-data(:,5).*tail_mat(2).*cps.*yield_U - ...
        tail_mat_th(2).*cps.*yield_Th.*data(:,8)-  blk .*datablkm(6,i); ...
         % Th230
29  err_data30 = 2*std(data30)./sqrt(length(data30));
30  abs_data30 = mean(data30);

32  data32      = data(:,8)-data(:,5).*tail_mat_cup(3)-  blk ...
        .*datablkm(7,i);  % Th232
33  err_data32 = 2*std(data32)./sqrt(length(data32));
34  abs_data32 = mean(data32);

36  %% calculating atomic ratios, mass fractionation correction, 2 ...
        sigma outlier test
37  R58d = data35./data38;  % U235/U238 for mass fractionation correction

39  R58u = data35./data38;  % U235/U238 for monitoring machine drift
40  [R58u, errR58u, R58u_, errRel58u] = outliertest(R58u); % output: ...
        outlier corrected R58, 2sigma SE, mean, 2sigma relative SE

42  R58  = data35./data38.*(1./137.881./R58d).^mf58;  % U235/U238
43  [R58, errR58, R58_, errRel58]      = outliertest(R58);

45  R34  = data33./data34.*(1./137.881./R58d).^mf34;  % U233/U234
46  [R34, errR34, R34_, errRel34]      = outliertest(R34);

48  R56  = data35./data36.*(1./137.881./R58d).^mf56;  % U235/U236 and ...
        mass fractionation
49  [R56, errR56, R56_, errRel56]      = outliertest(R56);

51  R48  = data34./data38.*(1./137.881./R58d).^mf48;  % U234/U238
52  [R48, errR48, R48_, errRel48]      = outliertest(R48);

54  R09  = data30./data29.*(1./137.881./R58d).^mf09;  % Th230/Th229
```

117

```
55  [R09, errR09, R09_, errRel09]    = outliertest(R09);

56

57  R29  = data32./(data29./(cps*yield_Th)).*(1./137.881./R58d).^mf29; ...
         % Th232/Th229
58  [R29, errR29, R29_, errRel29]    = outliertest(R29);

59

60  R43  = data34./data33.*(1./137.881./R58d).^mf43;  % U233/U234
61  [R43, errR43, R43_, errRel43]    = outliertest(R43);

62

63  R92  = (data29./(cps.*yield_Th))./data32.*(1./137.881./R58d).^mf92; ...
         % Th232/Th229
64  [R92, errR92, R92_, errRel92]    = outliertest(R92);

65

66  R36  = data33./data36.*(1./137.881./R58d).^mf36;  % U233/U234
67  [R36, errR36, R36_, errRel36]    = outliertest(R36);

68

69  R45  = data34./data35.*(1./137.881./R58d).^mf45;  % U233/U234
70  [R45, errR45, R45_, errRel45]    = outliertest(R45);

71

72  R02  = (data30./(cps*yield_Th))./data32.*(1./137.881./R58d).^mf02; ...
         % Th230/Th229
73  [R02, errR02, R02_, errRel02]    = outliertest(R02);
```

C.5.3 Measurement method: ^{230}Th on SEM with RPQ

```
1   % tail_mat(_th)/_cup): tailing correction U/Th, SEM+RPQ/cup, ...
      UH_plus/ThH_plus: Hydride correction,
2   % blk: process blank correction, yield_U(_Th)/gain13: yield/gain13 ...
      correction
3
4   data33    = data(:,1)-data(:,5).*tail_mat_cup(4) - ...
      data(:,8).*ThH_plus - blk .*datablkm(1,i); % U233
5   err_data33 = 2*std(data33)./sqrt(length(data33));
6   abs_data33 = mean(data33);
7
8   data34    = gain13.*data(:,2)-UH_plus.*data33 - ...
      data33*R34_33-data(:,5).*tail_mat_cup(5)- blk .*datablkm(2,i); ...
      % U234
9   err_data34 = 2*std(data34)./sqrt(length(data34));
10  abs_data34 = mean(data34);
11
12  data35    = (data(:,3)-data(:,2).*UH_plus.*gain13) - ...
      data33*R35_33-data(:,5).*tail_mat_cup(6) - blk .*datablkm(3,i); ...
      % U235
13  err_data35 = 2*std(data35)./sqrt(length(data35));
14  abs_data35 = mean(data35);
15
16  data36    = ...
      data(:,4)-UH_plus.*data(:,3)-data(:,5).*tail_mat_cup(7)- blk ...
      .*datablkm(4,i);  % U236
17  err_data36 = 2*std(data36)./sqrt(length(data36));
```

```matlab
18  abs_data36 = mean(data36);
19
20  data38     = data(:,5)- blk .*datablkm(5,i);  % U238
21  err_data38 = 2*std(data38)./sqrt(length(data38));
22  abs_data38 = mean(data38);
23
24  data29     = data(:,6)-data(:,5).*tail_mat_cup(1) - ...
        tail_mat_th_cup(1).*data(:,8)- blk .*datablkm(8,i);  % Th229
25  err_data29 = 2*std(data29)./sqrt(length(data29));
26  abs_data29 = mean(data29);
27
28  data30     = data(:,7)-ThH_plus.*data29.*cps*yield_Th - ...
29  data29*R30_29.*cps*yield_Th-data(:,5).*tail_mat(2).*cps*yield_U - ...
30  tail_mat_th(2).*cps.*yield_Th.*data(:,8)- blk .*datablkm(6,i);  % Th230
31  err_data30 = 2*std(data30)./sqrt(length(data30));
32  abs_data30 = mean(data30);
33
34  data32     = data(:,8)-data(:,5).*tail_mat_cup(3)- blk ...
        .*datablkm(7,i);  % Th232
35  err_data32 = 2*std(data32)./sqrt(length(data32));
36  abs_data32 = mean(data32);
37
38
39  %% calculating atomic ratios, mass fractionation correction, 2 ...
        sigma outlier test
40  R58d = data35./data38;  % U235/U238 for mass fractionation correction
41
42  R58u = data35./data38;  % U235/U238 for monitoring machine drift
43  [R58u, errR58u, R58u_, errRel58u] = outliertest(R58u); % output: ...
        outlier corrected R58, 2sigma SE, mean, 2sigma relative SE
44
45  R58  = data35./data38.*(1./137.881./R58d).^mf58;  % U235/U238
46  [R58, errR58, R58_, errRel58]     = outliertest(R58);
47
48  R34  = data33./data34.*(1./137.881./R58d).^mf34;  % U233/U234
49  [R34, errR34, R34_, errRel34]     = outliertest(R34);
50
51  R56  = data35./data36.*(1./137.881./R58d).^mf56;  % U235/U236 and ...
        mass fractionation
52  [R56, errR56, R56_, errRel56]     = outliertest(R56);
53
54  R48  = data34./data38.*(1./137.881./R58d).^mf48;  % U234/U238
55  [R48, errR48, R48_, errRel48]     = outliertest(R58u);
56
57  R09  = (data30./(cps.*yield_Th))./data29.*(1./137.881./R58d).^mf09; ...
        % Th230/Th229
58  [R09, errR09, R09_, errRel09]     = outliertest(R09);
59
60  R29  = data32./data29.*(1./137.881./R58d).^mf29;  % Th232/Th229
61  [R29, errR29, R29_, errRel29]     = outliertest(R29);
62
63  R43  = data34./data33.*(1./137.881./R58d).^mf43;  % U233/U234
```

```
64  [R43, errR43, R43_, errRel43]      = outliertest(R43);

65

66  R92  = data29./data32.*(1./137.881./R58d).^mf92;  % Th232/Th229
67  [R92, errR92, R92_, errRel92]      = voutliertest(R92);

68

69  R36  = data33./data36.*(1./137.881./R58d).^mf36;  % U233/U234
70  [R36, errR36, R36_, errRel36]      = outliertest(R36);

71

72  R45  = data34./data35.*(1./137.881./R58d).^mf45;  % U233/U234
73  [R45, errR45, R45_, errRel45]      = outliertest(R45);

74

75  R02  = (data30./(cps*yield_Th))./data32.*(1./137.881./R58d).^mf02;  ...
         % Th230/Th229
76  [R02, errR02, R02_, errRel02]      = outliertest(R02);
```

C.5.4 Measurement method: all isotopes on Faraday cups

```
1  % tail_mat(_th)/_cup): tailing correction U/Th, SEM+RPQ/cup, ...
      UH_plus/ThH_plus: Hydride correction,
2  % blk: process blank correction, yield_U(_Th)/gain13: yield/gain13 ...
      correction
3
4  data33     = data(:,1)-data(:,5).*tail_mat_cup(4) - ...
      data(:,8).*ThH_plus - blk .*datablkm(1,i); % U233
5  err_data33 = 2*std(data33)./sqrt(length(data33));
6  abs_data33 = mean(data33);

7

8  data34     = gain13.*data(:,2)-UH_plus.*data33 - ...
      data33*R34_33-data(:,5).*tail_mat_cup(5)- blk ...
      .*datablkm(2,i)./cps; % U234
9  err_data34 = 2*std(data34)./sqrt(length(data34));
10 abs_data34 = mean(data34);

11

12 data35     = (data(:,3)-data(:,2).*UH_plus.*gain13) - ...
      data33*R35_33-data(:,5).*tail_mat_cup(6)- blk .*datablkm(3,i); ...
      % U235
13 err_data35 = 2*std(data35)./sqrt(length(data35));
14 abs_data35 = mean(data35);

15

16 data36     = ...
      data(:,4)-UH_plus.*data(:,3)-data(:,5).*tail_mat_cup(7)- blk ...
      .*datablkm(4,i);  % U236
17 err_data36 = 2*std(data36)./sqrt(length(data36));
18 abs_data36 = mean(data36);

19

20 data38     = data(:,5)- blk .*datablkm(5,i);  % U238
21 err_data38 = 2*std(data38)./sqrt(length(data38));
22 abs_data38 = mean(data38);

23

24 data29     = data(:,6)-data(:,5).*tail_mat_cup(1) - ...
      tail_mat_th_cup(1).*data(:,8)- blk .*datablkm(8,i)./cps;  % Th229
```

```matlab
25  err_data29 = 2*std(data29)./sqrt(length(data29));
26  abs_data29 = mean(data29);
27
28  data30      = gain13.*data(:,7)-ThH_plus.*data29 - ...
        data29*R30_29-data(:,5).*tail_mat_cup(2)- ...
        tail_mat_th_cup(2).*data(:,8)- blk .*datablkm(6,i)./cps;  % Th230
29  err_data30 = 2*std(data30)./sqrt(length(data30));
30  abs_data30 = mean(data30);
31
32  data32      = data(:,8)-data(:,5).*tail_mat_cup(3)- blk ...
        .*datablkm(7,i);   % Th232
33  err_data32 = 2*std(data32)./sqrt(length(data32));
34  abs_data32 = mean(data32);
35
36  %% calculating atomic ratios, mass fractionation correction, 2 ...
        sigma outlier test
37  R58d = data35./data38; % U235/U238 for mass fractionation correction
38
39  R58u = data35./data38; % U235/U238 for monitoring machine drift
40  [R58u, errR58u, R58u_, errRel58u] = outliertest(R58u); % output: ...
        outlier corrected R58, 2sigma SE, mean, 2sigma relative SE
41
42  R58  = data35./data38.*(1./137.881./R58d).^mf58;  % U235/U238
43  [R58, errR58, R58_, errRel58]     = outliertest(R58);
44
45  R34  = data33./data34.*(1./137.881./R58d).^mf34;  % U233/U234
46  [R34, errR34, R34_, errRel34]     = outliertest(R34);
47
48  R56  = data35./data36.*(1./137.881./R58d).^mf56;  % U235/U236 and ...
        mass fractionation
49  [R56, errR56, R56_, errRel56]     = outliertest(R56);
50
51  R48  = data34./data38.*(1./137.881./R58d).^mf48;  % U234/U238
52  [R48, errR48, R48_, errRel48]     = outliertest(R48);
53
54  R09  = data30./data29.*(1./137.881./R58d).^mf09;  % Th230/Th229
55  [R09, errR30, R09_, errRel09]     = outliertest(R09);
56
57  R29  = data32./data29.*(1./137.881./R58d).^mf29;  % Th232/Th229
58  [R29, errR32, R29_, errRel29]     = outliertest(R29);
59
60  R43  = data34./data33.*(1./137.881./R58d).^mf43;  % U233/U234
61  [R43, errR43, R43_, errRel43]     = outliertest(R43);
62
63  R92  = data29./data32.*(1./137.881./R58d).^mf92;  % Th232/Th229
64  [R92, errR92, R92_, errRel92]     = outliertest(R92);
65
66  R36  = data33./data36.*(1./137.881./R58d).^mf36;  % U233/U234
67  [R36, errR36, R36_, errRel36]     = outliertest(R36);
68
69  R45  = data34./data35.*(1./137.881./R58d).^mf45;  % U233/U234
70  [R45, errR45, R45_, errRel45]     = outliertest(R45);
```

```
71
72  R02 = data30./data32.*(1./137.881./R58d).^mf02;  % Th230/Th229
73  [R02, errR02, R02_, errRel02]    = outliertest(R02);
```

C.6 Function outliertest

```
1  function [X, errX, meanX, errRelX] = outliertest(x)
2
3  out       = bsxfun(@lt, mean(x) + 2*std(x), x) | bsxfun(@gt, ...
       mean(x) - 2*std(x), x); % outlier determination
4  x(out)    = [];                           % remove outliers
5  X         = x;
6  errX      = 2*std(x)./sqrt(length(x)); % 2 sigma SE
7  meanX     = mean(x);                       % mean
8  errRelX   = errX/meanX;                    % 2 sigma relative error
9
10  end
```

C.7 Graphical user interface

```
1   function varargout = gui(varargin)
2   % GUI MATLAB code for gui.fig
3   %      GUI, by itself, creates a new GUI or raises the existing
4   %      singleton*.
5   %
6   %      H = GUI returns the handle to a new GUI or the handle to
7   %      the existing singleton*.
8   %
9   %      GUI('CALLBACK',hObject,eventData,handles,...) calls the local
10  %      function named CALLBACK in GUI.M with the given input arguments.
11  %
12  %      GUI('Property','Value',...) creates a new GUI or raises the
13  %      existing singleton*.  Starting from the left, property value ...
       pairs are
14  %      applied to the GUI before gui_OpeningFcn gets called.  An
15  %      unrecognized property name or invalid value makes property ...
       application
16  %      stop.  All inputs are passed to gui_OpeningFcn via varargin.
17  %
18  %      *See GUI Options on GUIDE's Tools menu.  Choose "GUI allows ...
       only one
19  %      instance to run (singleton)".
20  %
21  % See also: GUIDE, GUIDATA, GUIHANDLES
22
23  % Edit the above text to modify the response to help gui
24
25  % Last Modified by GUIDE v2.5 20-Mar-2017 22:16:52
26
```

```matlab
27 % Begin initialization code - DO NOT EDIT
28 gui_Singleton = 1;
29 gui_State = struct('gui_Name',        mfilename, ...
30                    'gui_Singleton',  gui_Singleton, ...
31                    'gui_OpeningFcn', @gui_OpeningFcn, ...
32                    'gui_OutputFcn',  @gui_OutputFcn, ...
33                    'gui_LayoutFcn',  [] , ...
34                    'gui_Callback',   []);
35 if nargin && ischar(varargin{1})
36     gui_State.gui_Callback = str2func(varargin{1});
37 end
38
39 if nargout
40     [varargout{1:nargout}] = gui_mainfcn(gui_State, varargin{:});
41 else
42     gui_mainfcn(gui_State, varargin{:});
43 end
44 % End initialization code - DO NOT EDIT
45
46
47 % --- Executes just before gui is made visible.
48 function gui_OpeningFcn(hObject, eventdata, handles, varargin)
49 % This function has no output args, see OutputFcn.
50 % hObject    handle to figure
51 % eventdata  reserved - to be defined in a future version of MATLAB
52 % handles    structure with handles and user data (see GUIDATA)
53 % varargin   command line arguments to gui (see VARARGIN)
54
55 % clear workspace
56 evalin( 'base', 'clearvars *' )
57
58 set(handles.tableStartParams, 'Data', cell(4,1))
59 set(handles.table_factors,    'Data', cell(1,4))
60 set(handles.table_tail_u,     'Data', cell(2,8))
61 set(handles.table_tail_th,    'Data', cell(2,2))
62
63 startParams = set(handles.tableStartParams,'data',{1,1,1,1}')
64
65 % Choose default command line output for gui
66 handles.output = hObject;
67
68 % Update handles structure
69 guidata(hObject, handles);
70
71
72 % --- Outputs from this function are returned to the command line.
73 function varargout = gui_OutputFcn(hObject, eventdata, handles)
74 % varargout  cell array for returning output args (see VARARGOUT);
75 % hObject    handle to figure
76 % eventdata  reserved - to be defined in a future version of MATLAB
77 % handles    structure with handles and user data (see GUIDATA)
78
```

```matlab
79  % Get default command line output from handles structure
80  varargout{1} = handles.output;
81
82
83  % --- Executes during object creation, after setting all properties.
84  function path_CreateFcn(hObject, eventdata, handles)
85  % hObject    handle to path (see GCBO)
86  % eventdata  reserved - to be defined in a future version of MATLAB
87  % handles    empty - handles not created until after all CreateFcns ...
        called
88
89  % Hint: edit controls usually have a white background on Windows.
90  %        See ISPC and COMPUTER.
91  if ispc && isequal(get(hObject,'BackgroundColor'), ...
       get(0,'defaultUicontrolBackgroundColor'))
92      set(hObject,'BackgroundColor','white');
93  end
94
95
96  % --- Executes on button press in path_button.
97  function path_button_Callback(hObject, eventdata, handles)
98  % hObject    handle to path_button (see GCBO)
99  % eventdata  reserved - to be defined in a future version of MATLAB
100 % handles    structure with handles and user data (see GUIDATA)
101 global data_root_folder
102 data_root_folder = uigetdir;
103 set(handles.path, 'string', data_root_folder);
104
105
106 % Resizes Gui to screen size
107 % --- Executes when figure1 is resized.
108 function figure1_ResizeFcn(hObject, eventdata, handles)
109 % hObject    handle to figure1 (see GCBO)
110 % eventdata  reserved - to be defined in a future version of MATLAB
111 % handles    structure with handles and user data (see GUIDATA)
112
113
114 % --- Executes during object creation, after setting all properties.
115 function tableStartParams_CreateFcn(hObject, eventdata, handles)
116 % hObject    handle to tableStartParams (see GCBO)
117 % eventdata  reserved - to be defined in a future version of MATLAB
118 % handles    empty - handles not created until after all CreateFcns ...
        called
119 set(hObject,'ColumnName',{'Values'}, 'RowName', {'Blank (1/0)' ...
       'Yield (U)','Yield (Th)','Gain (13 Ohm)'})
120
121
122 % --- Executes during object creation, after setting all properties.
123 function table_factors_CreateFcn(hObject, eventdata, handles)
124 % hObject    handle to table_factors (see GCBO)
125 % eventdata  reserved - to be defined in a future version of MATLAB
126 % handles    empty - handles not created until after all CreateFcns ...
```

124

```matlab
          called
127 set(hObject,'ColumnName',{'UH+' 'ThH+','AS RPQ','AS Cup'}, ...
          'RowName', {'Factors'})
128
129
130 % --- Executes during object creation, after setting all properties.
131 function table_tail_u_CreateFcn(hObject, eventdata, handles)
132 % hObject    handle to table_tail_u (see GCBO)
133 % eventdata  reserved - to be defined in a future version of MATLAB
134 % handles    empty - handles not created until after all CreateFcns ...
          called
135 set(hObject,'ColumnName',{'229','230','232','233','234','235','236','237'}, ...
          'RowName', {'Tailing SEM','Tailing Cup'})
136
137
138 % --- Executes during object creation, after setting all properties.
139 function table_tail_th_CreateFcn(hObject, eventdata, handles)
140 % hObject    handle to table_tail_th (see GCBO)
141 % eventdata  reserved - to be defined in a future version of MATLAB
142 % handles    empty - handles not created until after all CreateFcns ...
          called
143 set(hObject,'ColumnName',{'229','230'}, 'RowName', {'Tailing Th ...
          SEM','Tailing Th Cup'})
144
145
146 % --- Executes on button press in run_UTh.
147 function run_UTh_Callback(hObject, eventdata, handles)
148 % hObject    handle to run_UTh (see GCBO)
149 % eventdata  reserved - to be defined in a future version of MATLAB
150 % handles    structure with handles and user data (see GUIDATA)
151
152 global data_root_folder;
153 startParams = get(handles.tableStartParams,'data');
154
155
156 if exist(data_root_folder, 'dir') ≠ 7
157     errordlg('Please choose a valid data folder');
158 elseif exist(strcat(data_root_folder, '\yhas_th'), 'dir') ≠ 7
159     errordlg('Data folder must contain a yhas_th subfolder');
160 elseif exist(strcat(data_root_folder, '\yhas_u'), 'dir') ≠ 7
161     errordlg('Data folder must contain a yhas_u subfolder');
162 elseif exist(strcat(data_root_folder, '\data'), 'dir') ≠ 7
163     errordlg('Data folder must contain a data subfolder');
164
165 else
166
167     blk = startParams{1, 1};
168     yield_U = startParams{2, 1};
169     yield_Th = startParams{3, 1};
170     gain13 = startParams{4, 1};
171
172     is_gui = 1
```

```matlab
173
174     folder = ...
            'C:\Users\bwpc\bwSyncAndShare\Arbeit\matlab\ratios_2.7_gui'; ...
            % path of all matlab scripts
175     cd(folder)
176     addpath(genpath(folder))
177
178     run run_intro.m
179 end
180
181
182 % --- Executes on button press in run_U.
183 function run_U_Callback(hObject, eventdata, handles)
184 % hObject    handle to run_U (see GCBO)
185 % eventdata  reserved - to be defined in a future version of MATLAB
186 % handles    structure with handles and user data (see GUIDATA)
187
188
189 % --- Executes on button press in run_Th.
190 function run_Th_Callback(hObject, eventdata, handles)
191 % hObject    handle to run_Th (see GCBO)
192 % eventdata  reserved - to be defined in a future version of MATLAB
193 % handles    structure with handles and user data (see GUIDATA)
194
195
196 % --- Executes on slider movement.
197 function slider_axes_uran_Callback(hObject, eventdata, handles)
198 % hObject    handle to slider_axes_uran (see GCBO)
199 % eventdata  reserved - to be defined in a future version of MATLAB
200 % handles    structure with handles and user data (see GUIDATA)
201
202 % Hints: get(hObject,'Value') returns position of slider
203 %        get(hObject,'Min') and get(hObject,'Max') to determine ...
         range of slider
204
205 ylim(handles.axes_uran, [0, get(hObject,'Value')])
206
207
208 % --- Executes during object creation, after setting all properties.
209 function slider_axes_uran_CreateFcn(hObject, eventdata, handles)
210 % hObject    handle to slider_axes_uran (see GCBO)
211 % eventdata  reserved - to be defined in a future version of MATLAB
212 % handles    empty - handles not created until after all CreateFcns ...
         called
213
214 % Hint: slider controls usually have a light gray background.
215 if isequal(get(hObject,'BackgroundColor'), ...
         get(0,'defaultUicontrolBackgroundColor'))
216     set(hObject,'BackgroundColor',[.9 .9 .9]);
217 end
218
219
```

```matlab
220  % --- Executes on slider movement.
221  function slider_axes_thorium_Callback(hObject, eventdata, handles)
222  % hObject    handle to slider_axes_thorium (see GCBO)
223  % eventdata  reserved - to be defined in a future version of MATLAB
224  % handles    structure with handles and user data (see GUIDATA)
225
226  % Hints: get(hObject,'Value') returns position of slider
227  %        get(hObject,'Min') and get(hObject,'Max') to determine ...
         range of slider
228  ylim(handles.axes_thorium, [0, get(hObject,'Value')])
229
230
231  % --- Executes during object creation, after setting all properties.
232  function slider_axes_thorium_CreateFcn(hObject, eventdata, handles)
233  % hObject    handle to slider_axes_thorium (see GCBO)
234  % eventdata  reserved - to be defined in a future version of MATLAB
235  % handles    empty - handles not created until after all CreateFcns ...
         called
236
237  % Hint: slider controls usually have a light gray background.
238  if isequal(get(hObject,'BackgroundColor'), ...
         get(0,'defaultUicontrolBackgroundColor'))
239      set(hObject,'BackgroundColor',[.9 .9 .9]);
240  end
```

D Submitted manuscripts of the author

The following manuscripts are under submission in peer-reviewed journals and are co-authored by Jennifer Arps as of 15th of May, 2017. None of the manuscripts' contents were used in this work.

Wefing, A.-M. **J. Arps**, P. Blaser, C. Wienberg, D. Hebbeln, N. Frank
2017. Sub-permil precision U-series dating of scleractinian cold-water corals using an automated chromatographic U and Th extraction. *Journal of Analytical Atomic Spectrometry.*

Warken, S. F., J. Fohlmeister, A. Schröder-Ritzrau, **J. Arps**, S. Constantin, M. Terente, C. Spötl, A. Gerdes, J. Esper, N. Frank, A. Mangini, D. Scholz
2017. Reconstruction of late Holocene winter precipitation variability in southwestern Romania from a high-resolution speleothem trace element record. *Earth and Planetary Science Letters.*

Stinnesbeck, W., E. Frey, F. Hering, P. Zell, J. Avilés, M. Deininger, N. Frank, **J. Arps**, A. Geenen, J. Gescher, M. Isenbeck-Schröter, S. Ritter, S. Stinnesbeck, E. A. Núñez, A. G. González
2017. Hells Bells – speleothems from the Yucatán Peninsula, Mexico, generated underwater and by microbial calcite precipitation. *Palaeogeography, Palaeoclimatology, Palaeoecology.*

E Bibliography

Adkins, R., C. Cheng, H. Boyle, Druffel, and Edwards
  1998. Deep-Sea coral evidence for rapid change in ventilation of the deep north atlantic 15,400 years Ago. *Science (New York, N.Y.)*, 280(5364):725–8.

Andersen, M. B., C. H. Stirling, E. K. Potter, and A. N. Halliday
  2004. Toward epsilon levels of measurement precision on 234U/ 238U by using MC-ICPMS. *International Journal of Mass Spectrometry*, 237(2-3):107–118.

Andersen, M. B., C. H. Stirling, E. K. Potter, A. N. Halliday, S. G. Blake, M. T. McCulloch, B. F. Ayling, and M. O'Leary
  2008. High-precision U-series measurements of more than 500,000 year old fossil corals. *Earth and Planetary Science Letters*, 265(1-2):229–245.

Baker, A., I. Flemons, M. S. Andersen, K. Coleborn, and P. C. Treble
  2016. What determines the calcium concentration of speleothem-forming drip waters? *Global and Planetary Change*, 143:152–161.

Baker, A., D. Genty, W. Dreybrodt, W. L. Barnes, N. J. Mockler, and J. Grapes
  1998. Testing Theoretically Predicted Stalagmite Growth Rate with Recent Annually Laminated Samples: Implications for Past Stalagmite Deposition. *Geochimica et Cosmochimica Acta*, 62(3):393–404.

Baker, A., P. L. Smart, and D. C. Ford
  1993. Northwest European palaeoclimate as indicated by growth frequency variations of secondary calcite deposits. *Palaeogeography, Palaeoclimatology, Palaeoecology*, 100(3):291–301.

Baker, A. J., D. P. Mattey, and J. U. L. Baldini
  2014. Reconstructing modern stalagmite growth from cave monitoring, local meteorology, and experimental measurements of dripwater films. *Earth and Planetary Science Letters*, 392:239–249.

Banner, J. L., G. J. Wasserburg, J. H. Chen, and C. H. Moore
  1990. 234U238U230Th232Th systematics in saline groundwaters from central Missouri. *Earth and Planetary Science Letters*, 101(2-4):296–312.

Bard, E., M. Arnold, R. G. Fairbanks, and B. Hamelin
  1993. 230Th-234U and 14C ages obtained by mass spectrometry on corals. *Radiocarbon*, 35(1):191–199.

Bard, E., B. Hamelin, and R. G. Fairbanks
1990a. U/Th ages obtained by mass spectrometry in corals from Barbados. *Chemical Geology*, 84(1-4):157–158.

Bard, E., B. Hamelin, R. G. Fairbanks, and A. Zindler
1990b. Calibration of the C-14 timescale over the past 30,000 years using mass spectrometric U-Th ages from Barbados corals.

Baumann, J., D. Buhmann, W. Dreybrodt, and H. D. Schulz
1985. Calcite dissolution kinetics in porous media. *Chemical Geology*, 53(3-4):219–228.

Boch, R., H. Cheng, C. Spötl, R. L. Edwards, X. Wang, and P. Häuselmann
2011. NALPS: A precisely dated European climate record 120-60 ka. *Climate of the Past*, 7(4):1247–1259.

Böhm, E., J. Lippold, M. Gutjahr, M. Frank, P. Blaser, B. Antz, J. Fohlmeister, N. Frank, M. B. Andersen, and M. Deininger
2015. Strong and deep Atlantic meridional overturning circulation during the last glacial cycle. *Nature*, 517(7534):73–76.

Bourdon, B., S. Turner, G. Henderson, and C. Lundstrom
2003. Introduction to U-series Geochemistry. *Reviews in Mineralogy & Geochemistry*, 52(1):1–24.

Burns, S. J., D. Fleitmann, A. Matter, U. Neff, and A. Mangini
2001. Speleothem evidence from Oman for continental pluvial events during interglacial periods. *Geology*, 29(7):623–626.

Burns, S. J., A. Matter, N. Frank, and A. Mangini
1998. Speleothem-based paleoclimate record from northern Oman. *Geology*, 26(6):499–502.

Chen, T.-Y., M. Frank, B. A. Haley, M. Gutjahr, and R. F. Spielhagen
2012. Variations of North Atlantic inflow to the central Arctic Ocean over the last 14 million years inferred from hafnium and neodymium isotopes. *Earth and Planetary Science Letters*, 353–354:82–92.

Cheng, H., J. Adkins, R. L. Edwards, and E. A. Boyle
2000a. U-Th dating of deep-sea corals. *Geochimica et Cosmochimica Acta*, 64(14):2401–2416.

Cheng, H., R. L. Edwards, W. S. Broecker, G. H. Denton, X. Kong, Y. Wang, R. Zhang, and X. Wang
2009. Ice Age Terminations. *Science*, 326(5950):248–252.

Cheng, H., R. L. Edwards, J. Hoff, C. D. Gallup, D. A. Richards, and Y. Asmerom
2000b. The half-lives of uranium-234 and thorium-230. In *Chemical Geology*, volume 169, Pp. 17–33.

Cheng, H., R. L. Edwards, C.-C. Shen, V. J. Polyak, Y. Asmerom, J. Woodhead, J. Hellstrom, Y. Wang, X. Kong, C. Spötl, X. Wang, and E. Calvin Alexander 2013. Improvements in 230Th dating, 230Th and 234U half-life values, and U–Th isotopic measurements by multi-collector inductively coupled plasma mass spectrometry. *Earth and Planetary Science Letters*, 371-372:82–91.

Cheng, H., R. L. Edwards, and Y. Wang
1998. U/th and u/pa dating of nanjing man and peking man. *Chinese Science Bulletin*, 43(1):26–26.

Cheng, H., R. L. Edwards, Y. Wang, X. Kong, Y. Ming, M. J. Kelly, X. Wang, C. D. Gallup, and W. Liu
2006. A penultimate glacial monsoon record from Hulu Cave and two-phase glacial terminations. *Geology*, 34(3):217–220.

Cherdyntsev, V. and I. Kazachevskii
1965. Age of Pleistocene carbonate Formation according to Thorium and Uranium isotopes. *osti.gov*.

Davis, B., S. Brewer, A. Stevenson, and J. Guiot
2003. The temperature of Europe during the Holocene reconstructed from pollen data. *Quaternary Science Reviews*, 22(15-17):1701–1716.

Dorale, J. A. and Z. Liu
2009. Limitations of hendy test criteria in judging the paleoclimatic suitability of speleothems and the need for replication. *Journal of Cave and Karst Studies*, 71(1):73–80.

Dornick, C.
2016. Charakterisierung verschiedener Detektortypen in der Inductively Coupled Plasma Massen Spektrometrie (ICP-MS). Bachelor's thesis, Ruprecht-Karls-Universität Heidelberg.

Douville, E., E. Sallé, N. Frank, M. Eisele, E. Pons-Branchu, and S. Ayrault
2010. Rapid and accurate U–Th dating of ancient carbonates using inductively coupled plasma-quadrupole mass spectrometry. *Chemical Geology*, 272(1-4):1–11.

Dreybrodt, W.
1988. *Processes in Karst Systems*. Springer-Verlag Berlin Heidelberg.

Dreybrodt, W.
1999. Chemical kinetics, speleothem growth and climate. *Boreas*, 28(3):347–356.

Dreybrodt, W. and D. Romanov
    2008. Regular stalagmites: The theory behind their shape. *Acta Carsol.*, 37(2):175–184.

Edwards, R. L., J. H. Chen, and G. J. Wasserburg
    1987. 238U234U230Th232Th systematics and the precise measurement of time over the past 500,000 years. *Earth and Planetary Science Letters*, 81(2-3):175–192.

Emiliani, C.
    1955. Pleistocene temperatures.

Fairchild, I. J., A. Baker, A. Asrat, D. Dominguez-Villar, J. Gunn, A. Hartland, and D. Lowe
    2012. *Speleothem Science: From Process to Past Environments.*

Fietzke, J., V. Liebetrau, A. Eisenhauer, and C. Dullo
    2005. Determination of uranium isotope ratios by multi-static MIC-ICP-MS: method and implementation for precise U- and Th-series isotope measurements. *Journal of Analytical Atomic Spectrometry*, 20(5):395.

Fontugne, M., Q. Shao, N. Frank, F. Thil, N. Guidon, and E. Boeda
    2013. Cross-dating (Th/U-14C) of calcite covering prehistoric paintings at Serra da Capivara National Park, Piaui, Brazil. *Radiocarbon*, 55(2):1191–1198.

Frank, N., M. Braum, U. Hambach, A. Mangini, and G. Wagner
    2000. Warm Period Growth of Travertine during the Last Interglaciation in Southern Germany. *Quaternary Research*, 54(1):38–48.

Frisia, S., A. Borsato, N. Preto, and F. McDermott
    2003. Late Holocene annual growth in three Alpine stalagmites records the influence of solar activity and the North Atlantic Oscillation on winter climate. *Earth and Planetary Science Letters*, 216(3):411–424.

Gallup, C. D., R. L. Edwards, and R. G. Johnson
    1994. The timing of high sea levels over the past 200,000 years. *Science (New York, N.Y.)*, 263(5148):796–800.

Genty, D., A. Baker, and B. Vokal
    2001. Instra- and inter-annual growth rate of modern stalagmites. *Chemical Geology*, 176(1-4):191–212.

Goldstein, S. J.
    2003. Techniques for Measuring Uranium-series Nuclides: 1992-2002. *Reviews in Mineralogy and Geochemistry*, 52(1):23–57.

Grumet, N. S., T. P. Guilderson, and R. B. Dunbar
    2002. Meridional transport in the Indian Ocean traced by coral radiocarbon. *Journal of Marine Research*, 60:725–742.

Hays, J. D., J. Imbrie, and N. J. Shackleton
  1976. Variations in the Earth's Orbit: Pacemaker of the Ice Ages. *Science (New York, N.Y.)*, 194(4270):1121–32.

Hoffmann, D. L., M. Rogerson, C. Spötl, M. Luetscher, D. Vance, A. H. Osborne, N. M. Fello, and G. E. Moseley
  2016. Timing and causes of North African wet phases during the last glacial period and implications for modern human migration. *Scientific Reports*, 6(November):36367.

Holzhauser, H.
  2007. *Holocene glacier fluctuations in the Swiss Alps*, Documents Préhistoriques n° 21. Paris: Editions du CTHS, Paris.

Holzhauser, H.
  2009. Auf dem Holzweg zur Gletschergeschichte. *Hallers Landschaften und Gletscher. Beiträge zu den Veranstaltungen der Akademien der Wissenschaften Schweiz 2008 zum Jubiläumsjahr Haller300. Sonderdruck aus den Mitteilungen der Naturforschenden Gesellschaft in Bern*, 66:173–208.

Imbrie, J.
  1985. A theoretical framework for the Pleistocene ice ages: William Smith Lecture. *Journal of the Geological Society*, 142(3):417–432.

Ivanovich, M.
  1994. Uranium Series Disequilibrium - Concepts and Applications. *Radiochimica Acta*, 64(2):81–94.

Ivanovich, M. and R. S. Harmon
  1992. Uranium-series disequilibrium: applications to earth, marine, and environmental sciences, 2nd edition. *Uranium-series disequilibrium: applications to earth, marine, and environmental sciences, 2nd edition.*

Jaffey, A. H., K. F. Flynn, L. E. Glendenin, W. C. Bentley, and A. M. Essling
  1971. Precision measurement of half-lives and specific activities of U235 and U238. *Physical Review C*, 4(5):1889–1906.

Jo, K.-N., K. S. Woo, S. Yi, D. Y. Yang, H. S. Lim, Y. Wang, H. Cheng, and R. L. Edwards
  2014. Mid-latitude interhemispheric hydrologic seesaw over the past 550,000 years. *Nature*, 508(7496):378–82.

Kaufmann, G.
  2003. Stalagmite growth and palaeo-climate: The numerical perspective. *Earth and Planetary Science Letters*, 214(1-2):251–266.

Kaufmann, G. and W. Dreybrodt
2004. Stalagmite growth and palaeo-climate: An inverse approach. *Earth and Planetary Science Letters*, 224(3-4):529–545.

Kigoshi, K.
1971. Alpha-recoil thorium-234: dissolution into water and the uranium-234/uranium-238 disequilibrium in nature. *Science (New York, N.Y.)*, 173(3991):47–48.

Lea, D. W. and E. A. Boyle
1990. Foraminiferal reconstruction of barium distributions in water masses of the glacial oceans. *Paleoceanography*, 5(5):719–742.

Lisiecki, L. E. and M. E. Raymo
2005. A Pliocene-Pleistocene stack of 57 globally distributed benthic $\delta^{18}O$ records. *Paleoceanography*, 20(1):1–17.

Ludwig, K. R. and D. M. Titterington
1994. Calculation of 230Th/U isochrons, ages, and errors. *Geochimica et Cosmochimica Acta*, 58(22):5031–5042.

Mason, A. J. and G. M. Henderson
2010. Correction of multi-collector-ICP-MS instrumental biases in high-precision uranium-thorium chronology. *International Journal of Mass Spectrometry*, 295(1-2):26–35.

Matos, L., F. Mienis, C. Wienberg, N. Frank, C. Kwiatkowski, J. Groeneveld, F. Thil, F. Abrantes, M. R. Cunha, and D. Hebbeln
2015. Interglacial occurrence of cold-water corals off Cape Lookout (NW Atlantic): First evidence of the Gulf Stream influence. *Deep-Sea Research Part I: Oceanographic Research Papers*, 105:158–170.

Mattey, D., D. Lowry, J. Duffet, R. Fisher, E. Hodge, and S. Frisia
2008. A 53 year seasonally resolved oxygen and carbon isotope record from a modern Gibraltar speleothem: Reconstructed drip water and relationship to local precipitation. *Earth and Planetary Science Letters*, 269(1-2):80–95.

McDermott, F.
2004. Palaeo-climate reconstruction from stable isotope variations in speleothems: A review. In *Quaternary Science Reviews*, volume 23, Pp. 901–918.

Montagna, P., M. McCulloch, E. Douville, M. Lopez Correa, J. Trotter, R. Rodolfo-Metalpa, D. Dissard, C. Ferrier-Pagès, N. Frank, A. Freiwald, S. Goldstein, C. Mazzoli, S. Reynaud, A. Rüggeberg, S. Russo, and M. Taviani
2014. Li/Mg systematics in scleractinian corals: Calibration of the thermometer. *Geochimica et Cosmochimica Acta*, 132:288–310.

Moseley, G. E., R. L. Edwards, K. A. Wendt, H. Cheng, Y. Dublyansky, Y. Lu, R. Boch, and C. Spötl
2016. Reconciliation of the Devils Hole climate record with orbital forcing. *Science*, 351(6269):165–168.

Moseley, G. E., C. Spötl, H. Cheng, R. Boch, A. Min, and R. L. Edwards
2015. Termination-II interstadial/stadial climate change recorded in two stalagmites from the north European Alps. *Quaternary Science Reviews*, 127:229–239.

Mühlinghaus, C., D. Scholz, and A. Mangini
2007. Modelling stalagmite growth and d13C as a function of drip interval and temperature. *Geochimica et Cosmochimica Acta*, 71(11):2780–2790.

Neff, U.
2001. *Massenspektrometrische Th/U-Datierung von Höhlensintern aus dem Oman: Klimaarchive des asiatischen Monsuns.* PhD thesis, Ruprecht-Karls-Universität Heidelberg.

NeKO and M. Trüssel
2014. *Arbeitsbericht NAB 14-73 Nachweis von fünf Karstniveaus in Obwalden und Nidwalden mit ersten radiometrischen U/Th-Datierungen von Stalagmiten in den beiden jüngsten fossilen Karstniveaus.* Wettingen: NeKO.

Nicolussi, K., M. Kaufmann, G. Patzelt, J. Plicht Van Der, and A. Thurner
2005. Holocene tree-line variability in the Kauner Valley, Central Eastern Alps, indicated by dendrochronological analysis of living trees and subfossil logs. *Vegetation History and Archaeobotany*, 14(3):221–234.

Nussbaumer, S. U., F. Steinhilber, M. Trachsel, P. Breitenmoser, J. Beer, A. Blass, M. Grosjean, A. Hafner, H. Holzhauser, H. Wanner, and H. J. Zumbühl
2011. Alpine climate during the Holocene: A comparison between records of glaciers, lake sediments and solar activity. *Journal of Quaternary Science*, 26(7):703–713.

Osmond, J. and J. Cowart
1976. The theory and uses of natural uranium isotopic variations in hydrology. *Atomic Energy Review*, 4(14):621–679.

Petersen, J., P. Deschamps, B. Hamelin, J. Goncalves, J.-L. Michelot, and K. Zouari
2013. Water-Rock Interaction and Residence Time of Groundwater Inferred by 234U/238U Disequilibria in the Tunisian Continental Intercalaire Aquifer System. *Procedia Earth and Planetary Science*, 7:685–688.

Petit, J. R., J. Jouzel, D. Raynaud, N. I. Barkov, J.-M. Barnola, I. Basile, M. Bender, J. Chappellaz, M. Davis, G. Delaygue, M. Delmotte, V. M. Kotlyakov, M. Legrand, V. Y. Lipenkov, C. Lorius, L. PEpin, C. Ritz, E. Saltzman, and M. Stievenard
1999. Climate and atmospheric history of the past 420,000 years from the Vostok ice core, Antarctica. *Nature*, 399(6735):429–436.

Plummer, L., T. Wigley, and D. Parkhurst
1978. The kinetics of calcite dissolution in CO2-water systems at 5C to 60C and 0.0 to 1.0 atm CO2. *American Journal of Science*, 278:179–216.

Potter, E. K., C. H. Stirling, M. B. Andersen, and A. N. Halliday
2005. High precision Faraday collector MC-ICPMS thorium isotope ratio determination. *International Journal of Mass Spectrometry*, 247(1-3):10–17.

Reimer, P. J., E. Bard, A. Bayliss, J. W. Beck, P. G. Blackwell, C. Bronk Ramsey, C. E. Buck, H. Cheng, R. L. Edwards, M. Friedrich, P. M. Grootes, T. P. Guilderson, H. Haflidason, I. Hajdas, C. Hatté, T. J. Heaton, D. L. Hoffmann, A. G. Hogg, K. A. Hughen, K. F. Kaiser, B. Kromer, S. W. Manning, M. Niu, R. W. Reimer, D. A. Richards, E. M. Scott, J. R. Southon, R. A. Staff, C. S. M. Turney, and J. van der Plicht
2013. IntCal13 and Marine13 Radiocarbon Age Calibration Curves 0–50,000 Years cal BP. *Radiocarbon*, 55(4):1869–1887.

Richards, D. A., P. L. Smart, and R. L. Edwards
1994. Maximum sea levels for the last glacial period from U-series ages of submerged speleothems. *Nature*, 367(6461):357–360.

Riechelmann, S., A. Schröder-Ritzrau, J. A. Wassenburg, J. Schreuer, D. K. Richter, D. F. C. Riechelmann, M. Terente, S. Constantin, A. Mangini, and A. Immenhauser
2014. Physicochemical characteristics of drip waters: Influence on mineralogy and crystal morphology of recent cave carbonate precipitates. *Geochimica et Cosmochimica Acta*, 145:13–29.

Robinson, L. F., G. M. Henderson, and N. C. Slowey
2002. U-Th dating of marine isotope stage 7 in Bahamas slope sediments. *Earth and Planetary Science Letters*, 196(3-4):175–187.

Romanov, D., G. Kaufmann, and W. Dreybrodt
2008. Modeling stalagmite growth by first principles of chemistry and physics of calcite precipitation. *Geochimica et Cosmochimica Acta*, 72(2):423–437.

Scholz, D. and D. L. Hoffmann
2011. StalAge - An algorithm designed for construction of speleothem age models. *Quaternary Geochronology*, 6(3-4):369–382.

Shakun, J. D., S. J. Burns, D. Fleitmann, J. Kramers, A. Matter, and A. Al-Subary
2007. A high-resolution, absolute-dated deglacial speleothem record of Indian Ocean climate from Socotra Island, Yemen. *Earth and Planetary Science Letters*, 259(3-4):442–456.

Shen, C. C., C. C. Wu, H. Cheng, R. L. Edwards, Y. T. Hsieh, S. Gallet, C. C. Chang, T. Y. Li, D. D. Lam, A. Kano, M. Hori, and C. Spötl
2012. High-precision and high-resolution carbonate 230Th dating by MC-ICP-MS with SEM protocols. *Geochimica et Cosmochimica Acta*, 99:71–86.

Sodemann, H. and E. Zubler
2010. Seasonal and inter-annual variability of the moisture sources for alpine precipitation during 1995-2002. *International Journal of Climatology*, 30(7):947–961.

Solomina, O. N., R. S. Bradley, D. A. Hodgson, S. Ivy-Ochs, V. Jomelli, A. N. Mackintosh, A. Nesje, L. A. Owen, H. Wanner, G. C. Wiles, and N. E. Young
2015. Holocene glacier fluctuations.

Spötl, C. and A. Mangini
2006. U/Th age constraints on the absence of ice in the central Inn Valley (eastern Alps, Austria) during Marine Isotope Stages 5c to 5a. *Quaternary Research*, 66(1):167–175.

Spötl, C., A. Mangini, S. J. Burns, N. Frank, and R. Pavuza
2004. *Speleothems from the High-Alpine Spannagel Cave, Zillertal Alps (Austria)*. Boston, MA: Springer US.

Spötl, C., A. Mangini, N. Frank, R. Eichstädter, and S. J. Burns
2002. Start of the last interglacial period at 135 ka: Evidence from a high Alpine speleothem. *Geology*, 30(9):815–818.

Stein, M., G. J. Wasserburg, P. Aharon, J. H. Chen, Z. R. Zhu, A. Bloom, and J. Chappell
1993. TIMS U-series dating and stable isotopes of the last interglacial event in Papua New Guinea. *Geochimica et Cosmochimica Acta*, 57(11):2541–2554.

Stirling, C. H. and M. B. Andersen
2009. Uranium-series dating of fossil coral reefs: Extending the sea-level record beyond the last glacial cycle. *Earth and Planetary Science Letters*, 284(3-4):269–283.

Stirling, C. H., T. M. Esat, M. T. McCulloch, and K. Lambeck
1995. High-precision U-series dating of corals from Western Australia and implications for the timing and duration of the Last Interglacial. *Earth and Planetary Science Letters*, 135(1-4):115–130.

Stoll, H. M., A. Moreno, A. Mendez-Vicente, S. Gonzalez-Lemos, M. Jimenez-Sanchez, M. J. Dominguez-Cuesta, R. L. Edwards, H. Cheng, and X. Wang
2013. Paleoclimate and growth rates of speleothems in the northwestern Iberian Peninsula over the last two glacial cycles. *Quaternary Research (United States)*, 80(2):284–290.

Suksi, J., K. Rasilainen, and P. Pitkänen
2006. Variations in 234U/238U activity ratios in groundwater-A key to flow system characterisation? *Physics and Chemistry of the Earth*, 31(10-14):556–571.

Swisher, C. C., W. J. Rink, S. C. Antón, H. P. Schwarcz, G. H. Curtis, a. Suprijo, and Widiasmoro
1996. Latest Homo erectus of Java: potential contemporaneity with Homo sapiens in southeast Asia. *Science (New York, N.Y.)*, 274(5294):1870–1874.

Szabo, B. J., K. R. Ludwig, D. R. Muhs, and K. R. Simmons
1994. Thorium-230 ages of corals and duration of the last interglacial sea-level high stand on oahu, hawaii. *Science (New York, N.Y.)*, 266(5182):93–96.

ThermoFisher
2009. *NEPTUNE Plus Hardware Manual*, volume Revision B. Massachussetts: Thermo Fisher Scientific.

Thomas, R.
2013. *Practical Guide to ICP-MS: A Tutorial for Beginners, Third Edition*.

Thompson, W. G. and S. L. Goldstein
2005. Open-system coral ages reveal persistent suborbital sea-level cycles. *Science (New York, N.Y.)*, 308(5720):401–4.

Thurber, D. L., W. S. Broecker, R. L. Blanchard, and H. A. Potratz
1965. Uranium-Series Ages of Pacific Atoll Coral. *Science*, 149(3679):55–58.

Ulianov, A., O. Müntener, and U. Schaltegger
2014. The ICPMS signal as a Poisson process: a review of basic concepts. *J. Anal. At. Spectrom.*

Wassenburg, J. A., S. Dietrich, J. Fietzke, J. Fohlmeister, K. P. Jochum, D. Scholz, D. K. Richter, A. Sabaoui, C. Spötl, G. Lohmann, M. O. Andreae, and A. Immenhauser
2016. Reorganization of the North Atlantic Oscillation during early Holocene deglaciation. *Nature Geosci*, 9(8):602–605.

Wedepohl, K. H.
1995. INGERSON LECTURE The composition of the continental crust. *Geochimica et Cosmochimica Acta*, 59(7):1217–1232.

Wefing, A.-M.
2016. Fully Automated Chromatographic Extraction of Th and U: Performance of the prepFAST-MC and its Application to Cold-Water Corals from the Angolan Margin. Master's thesis, Ruprecht-Karls-Universität Heidelberg.

Wong, C. I. and D. O. Breecker
2015. Advancements in the use of speleothems as climate archives. *Quaternary Science Reviews*, 127:1–18.

Danksagung

Mein ausdrücklicher Dank gilt Norbert Frank, denn diese Arbeit wäre ohne seine Unterstützung nicht möglich gewesen. Norbert Frank gab mir die Möglichkeit bei ihm fachfremd zu promovieren und somit die Reise in die Paläoklimatologie und Speläotheme zu beginnen. Ich bedanke mich für das Vertrauen, die Freiheit in meiner Arbeit aber auch für jeden Rat, wann immer ich welchen benötigt habe.

Bei Werner Aeschbach und Hai Cheng bedanke ich mich für Ihre Mitbetreuung und bei Rüdiger Klingeler für seine Freundlichkeit das Zweitgutachten zu übernehmen.

Ich bedanke mich bei Norbert Frank, Hai Cheng und Lawrence Edwards für die Möglichkeit, die außerordentliche Erfahrung eines Forschungsaufenthaltes an der University of Minnesota in Minneapolis zu machen.

Mein Dank gilt René Eichstädter, mit ihm habe ich viele zum Teil lustige zum Teil leidvolle Stunden am Massenspektrometer verbracht, Jens Fohlmeister für seine vielseitige wissenschaftliche Unterstützung und seiner Verfügbarkeit am Telefon und bei Andrea Schröder-Ritzrau für ihre großartige Hilfe und wissenschaftliche Unterstützung. Mein Dank gilt auch Christoph Dornick und Henrik Eckhardt, die ich während meiner Arbeit betreuen durfte und mit deren Hilfe ich ich viel Neues gelernt habe und deren Ergebnisse sich auch direkt und indirekt in dieser Arbeit wiederfinden. François Thil und Pu Zhang möchte ich für ihre ausgiebige Hilfe im Labor in Gif- sur-Yvette und Minneapolis danken. Ich bedanke mich bei Volker Schniepp und Ulrich Selgert für Ihre tolle Karte und die netten Emails. Eine große Hilfe waren mir Jens F., Evan B., Martin K., Freya H., Mayte D., Julius F. und Sabrina E. beim Korrekturlesen.

Ich danke dieser einzigartigen Gruppe für ihre Unterstützung und Ihrer sehr schönen Arbeitsatmosphäre. Mein besonderer Dank gilt hierbei René, Patrick, Freya, Andrea, Michi, Benny und Sophie, die mir oft Rat in schwierigen Situationen während meiner Arbeit gegeben haben.

Patrick, danke für den unlimitierten Schokoladensupport vor allem zur Oster- und Weihnachtszeit und die zukünftige daraus resultierende Diabetes, und danke für unser Zusammenstehen in unserer Endphase und unserer Diskussionen am Whiteboard. Freya und Patrick, danke, dass Ihr pflichtbewusst „regelmäßig" zum IUP-Stammtisch gekommen seid. Sabrina und Therese, danke für Eure Zeit für Snack- und Kaffeepausen. Arne und Jan, danke für unsere witzige Zeit als IUP PhD Repräsentanten.

Sabrina, Tessa, Schnix, Oskar, Emil, Mayte, danke für unser inniges und gemütliches WG-Leben auf dem Lande. DeFazanten gebührt Dank für posttraumatische Balkanpolkatangobluesfolkrockfahrstuhlsurf-Abende. Es war schön mit uns, schade, dass es

nun vorbei ist. Japan, Hindustan, Großbritannien, der Pfalz, Äthiopien und dem Commonwealth danke ich für die spaßigen Stunden Mittwoch Abends mit viel viel gar nicht mal so leckerer Pizza.

Ich danke natürlich Melanie und Amelie für ihre „optische" Unterstützung. Und zu aller Letzt danke ich den wichtigsten Menschen, meiner Famile, ohne deren Hilfe ich niemals so weit gekommen wäre und auf deren Unterstützung ich mich immer verlassen kann!

Vielen, vielen lieben Dank!

PS: Mir ist bewusst, dass diese Liste keine Gewähr für Vollständigkeit liefert. Es sollen sich bitte alle bedankt fühlen, denen Dank gebührt.